Analysis of T-stub component under combined shear and axial loads

Auteur : Moreau, Valentin
Promoteur(s) : Duchene, Laurent
Faculté : Faculté des Sciences appliquées
Diplôme : Master en ingénieur civil des constructions, à finalité spécialisée en "civil engineering"
Année académique : 2024-2025
URI/URL : http://hdl.handle.net/2268.2/23228

UNIVERSITE DE LIEGE
FACULTE DES SCIENCES APPLIQUEES

Analysis of T-stub component under combined shear and axial loads

MOREAU Valentin

Thesis presented to obtain the degree of :
Master of Science in Civil Engineering

Thesis supervisor :
Duchêne Laurent

Academic year: **2024 - 2025**

Acknowledgments

I would first like to thank my supervisor, Professor Laurent Duchene, for his ongoing support and mentorship. His availability, expertise and assiduous follow-up played a major role in the completion of this work.

I would also like to thank Arnaud Neutelers for his daily support. His availability, his sharing of expertise and his invaluable advice had a great impact on my work. His thoughtful comments during our discussions continuously encouraged and stimulated me throughout the entire process.

I am grateful to my proofreaders, my dear parents, for the time they took to review this work and for their sound advice on language, presentation and content.

Most of all, I would like to thank my family. Specifically my parents and my brother and sister, for their unwavering support. Their love, care and encouragement have allowed me to be in the best possible condition at every stage of the way.

I'm grateful to all my friends, especially Thibault, Noah and Arthur, without whom these last few years would not have been the same. Thank you for your support, your advice and for always being there when I needed help.

I am deeply grateful to my friends from the *kot Dominican*, François and Damien, for sharing daily life with me during three pivotal years of my studies. Your support, encouragement, and our enriching discussions created an ideal environment for personal and intellectual growth.

Finally, I would like to thank all the people who contributed to this thesis, and all those who encouraged, guided and supported me throughout my five years of study.

Summary

Title: Analysis of T-stub component under combined shear and axial loads

Structural robustness has gained prominence following historical collapses triggered by local damage. Modern design approaches increasingly account for catenary effects, which require significant rotational capacity in structural joints. In this context, the present thesis focuses on the specific behaviour of T-stub components subjected to combined shear and axial loads, due to their critical role in joint performance under extreme conditions.

Experimental reference data from Mancini's tests at the University of Trento, involving inclined loading angles on a T-stub specimen, were analysed to understand boundary conditions and load configurations. Analytical predictions from Eurocode and other standards (AISC, Australian, Song's proposal) were evaluated against these tests. Significant discrepancies highlighted the limitations of current codes in capturing T-stub behaviour under combined actions.

To improve understanding, a finite element model was developed in Abaqus. As material damage was excluded from the constitutive laws, the model was limited to capturing the pre-damage response. Validation showed good qualitative agreement with Mancini's results, though stiffness differences arose due to modelling simplifications and unavailable parameters (e.g. bolt threading and interaction details).

Rotational boundary conditions and a refined model including load-transmitting pins were analysed. The pin model revealed stress concentrations and detachment areas that simplified models could not capture. Stress analyses showed non-uniform distributions along the bolt, varying significantly with load inclination. Intermediate angles did not behave as linear combinations of pure shear and tension but displayed unique interaction effects.

Finally, moment effects in the bolt were investigated. Asymmetric contact stresses at the washer indicated bending moments about both X and Y axes - these effects are ignored in current design standards.

The present thesis demonstrates the sensitivity of T-stub performance to loading configurations and modelling assumptions. It underscores the need for refined numerical models and improved design criteria to account for complex stress states and moment effects in bolted connections under combined loading.

Résumé

Titre: Analyse de profilés en T soumis à des combinaisons de charges de cisaillement et axiales

La robustesse des structures a pris de l'importance à la suite d'effondrements historiques déclenchés par des dommages locaux. Les approches modernes de conception prennent de plus en plus en compte les effets caténaires, qui nécessitent une capacité de rotation significative dans les joints structurels. Dans ce contexte, le présent travail se concentre sur le comportement spécifique des composants de profilés en T soumis à des combinaisons de charges de cisaillement et axiales, en raison de leur rôle critique dans la performance des joints structurels dans des conditions extrêmes.

Les données de référence expérimentales des essais de Mancini à l'Université de Trento, impliquant des angles de chargement inclinés sur un profilé en T, ont été analysées pour comprendre les conditions limites et les configurations de chargement. Les prévisions analytiques de l'Eurocode et d'autres normes (AISC, Australienne, proposition de Song) ont été évaluées par rapport à ces essais. Des divergences significatives ont mis en évidence les limites des codes actuels dans la compréhension du comportement des profilés en T sous des actions combinées.

Pour améliorer la compréhension, un modèle d'éléments finis a été développé dans Abaqus. L'endommagement des matériaux étant exclu des lois constitutives, le modèle s'est limité à capturer la réponse avant l'endommagement. La validation a montré une bonne concordance qualitative avec les résultats de Mancini, bien que les différences de rigidité sont apparues en raison de simplifications de la modélisation et aux paramètres non disponibles (par exemple, le filetage des boulons et les détails d'interactions).

Les conditions limites de rotation et un modèle affiné comprenant des broches de transmission de charge ont été analysés. Le modèle à broches a révélé des concentrations de contraintes et des zones de détachement que les modèles simplifiés ne pouvaient pas saisir. Les analyses de contraintes ont montré des distributions non uniformes le long du boulon, variant de manière significative avec l'inclinaison de la charge. Les angles intermédiaires ne se sont pas comportés comme des combinaisons linéaires de cisaillement et de traction purs, mais ont présenté des effets d'interaction uniques.

Enfin, les effets des moments dans le boulon ont été étudiés. Les contraintes de contact asymétriques au niveau de la rondelle ont indiqué des moments de flexion autour des axes X et Y - ces effets sont ignorés dans les normes de conception actuelles.

Le présent travail démontre la sensibilité de la performance du T-stub aux configurations de chargement et aux hypothèses de modélisation. Elle souligne la nécessité d'affiner les modèles numériques et d'améliorer les critères de conception pour tenir compte des états de contrainte complexes et des effets de moment dans les assemblages boulonnés soumis à des charges combinées.

Contents

List of Figures

List of Tables

Introduction

In traditional construction methods, the concept of structural robustness was not explicitly considered. However, in recent decades, several buildings have experienced catastrophic events, both accidental and intentional, such as the terrorist attacks on the World Trade Center. These events have highlighted the vulnerability of structures to progressive collapse triggered by local damage. According to Eurocode 1-7 [1], robustness is "the ability of a structure to withstand events like fire, explosions, impact or the consequences of human error, without being damaged to an extent disproportionate to the original cause". As a result, new design guidelines have been developed to prevent collapse under accidental loads, including those caused by earthquakes, explosions and fires.

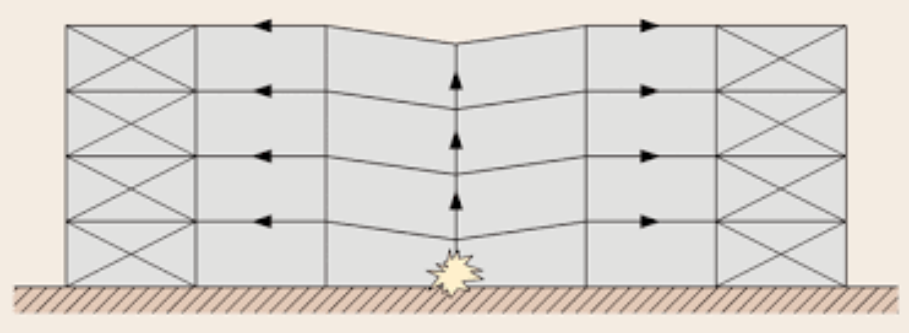

Figure 0.1: Loss of a column event - new equilibrium

Such events can lead to the loss of load-bearing elements, requiring the structure to achieve a new equilibrium state. To maintain stability, the structure must be capable of sustaining large deformations. In this context, the catenary effect and the rotational capacity of the joints play a critical role. The component method, developed by Professor Jaspart [2], is a valuable tool for evaluating joint deformation and resistance. Although the studies carried out on this method mainly dealt with elastic behaviour, further research is required to understand the plastic response and to accurately predict failure mechanisms. Among the various joint components, the T-stub is still under investigation, in contrast to the shear web panel, which has been more extensively studied.

In light of these challenges, it is essential to investigate the T-stub component under combined loading scenarios. The present thesis focuses on the behaviour of T-stubs subjected to simultaneous tensile and shear forces. Current design standards lack accuracy in this specific configuration. Therefore, a state-of-the-art review is presented to analyze the behaviour of T-stubs and bolted connections under combined effects. A major study conducted at the University of Trento [3], supported by experimental testing, serves as a reference for evaluating the reliability of existing standards and safety criteria. A specific specimen from this study is reproduced and further analyzed for several tests to enhance the accuracy of resistance predictions.

To achieve this, the studied specimen is modeled using the nonlinear finite element software Abaqus. The objective is to simulate the reference test and to validate the modeling approach. This will confirm the assumptions made during the modeling process and enable a comprehensive parametric study to explore the influence of various parameters.

The overall goal is to contribute to the understanding of the T-stub behaviour under combined axial and shear loads, a topic that has not been widely investigated to date.

Chapter 1

State of the art

Traditionally, structural joints were assumed to behave as either fully rigid or perfectly pinned, representing two extreme conditions. However, in practice, joint behaviour is more complex and typically falls between these two extremes. Therefore, joints are classified into three categories to better reflect their real performance characteristics.

In this context, as illustrated in Figure 1.1, joint behaviour is evaluated using the following parameters:

- **Rotational stiffness**, $S_{j,init}$, with threshold values defined in Eurocode 3 (Part 1-8) [1];
- **Relative rotation**, ϕ, characterizing the ductility or brittleness of the joint;
- **Bending moment**, M_j, transmitted through the joint.

A hinged joint does not transfer bending moments and is designed solely for shear force transmission. Conversely, a fully rigid joint restricts relative rotation and transmits the entire bending moment. In reality, however, joints always display a degree of flexibility, and even so-called 'hinged' joints transmit a portion of the moment. Hence, most joints are best described as *semi-rigid and partially resistant*.

An effective way to represent the relationship between the transmitted moment and the relative rotation in a joint is by using an equivalent spring.

Joint behaviour can be classified according to three main criteria, based on the properties of the equivalent springs used in the component method:

- **Stiffness**: This criterion reflects the ability of the joint to resist rotation under loading, based on its initial rotational stiffness, $S_{j,init}$. According to Eurocode 3 [1], joints are classified as rigid, semi-rigid, or pinned depending on whether the rotational deformation is negligible, significant but limited, or practically unconstrained. This classification focuses on serviceability behaviour and deformation characteristics, as illustrated in Figure 1.1.
- **Resistance**: While stiffness relates to deformation under service loads, resistance classification considers the capacity of the joint to transmit bending moments up to failure. A joint is categorized as full-strength, partial-strength, or pinned based on the comparison between its moment resistance, $M_{j,Rd}$, and the plastic moment resistance of the connected members. This criterion is essential for assessing the strength hierarchy within the structure and ensuring proper load redistribution. The resistance classification is illustrated in Figure 1.2.

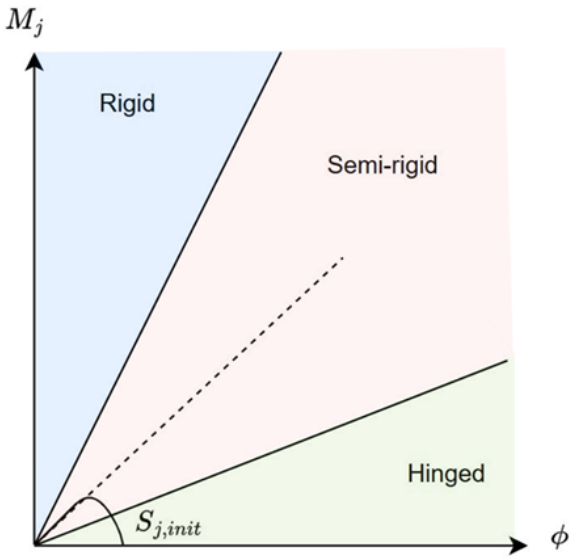

Figure 1.1: Stiffness classification [4]

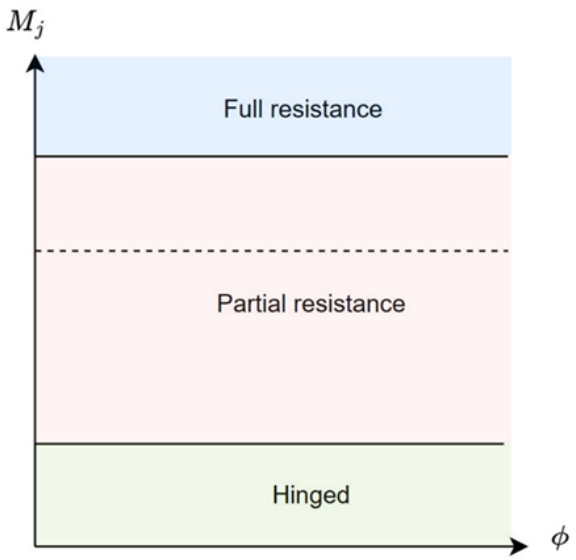

Figure 1.2: Resistance classification [4]

- **Ductility**: refers to the ability of the joint to undergo deformation before failure. Ductility criteria are provided in Eurocode 3 [5] and illustrated in Figure 1.3.

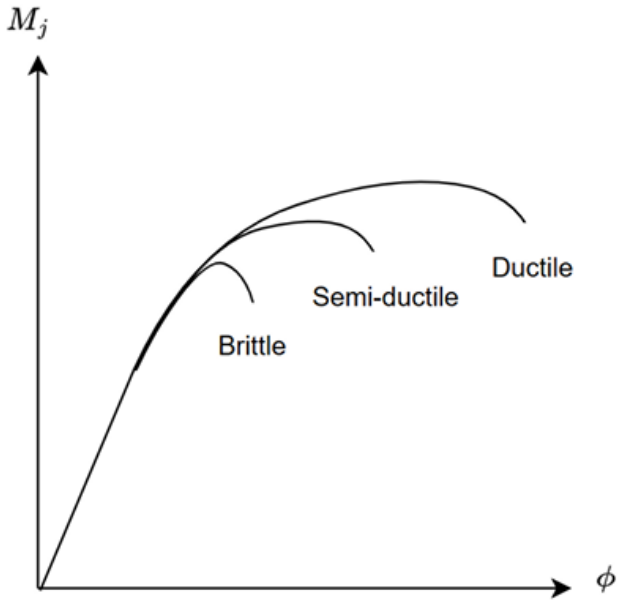

Figure 1.3: Ductility classification [4]

1.1 The component method

The *component method* models a structural joint as an assembly of elementary components, each contributing to the global response of the joint.

Each active component is analyzed and characterized individually. These components are then combined according to rules specified in Eurocode 3 (Part 1-8) [1] to determine the behaviour of the entire joint.

The procedure involves the following steps:

(i) Identification of the active components;

(ii) Determination of the resistance and stiffness of each component;

(iii) Assembly of components into an overall joint model.

As an example, consider a beam-to-column joint using an end-plate with two rows of bolts, as illustrated in Figure 1.4, and subjected to bending moment. Multiple components contribute to the overall behaviour in different regions of the connection.

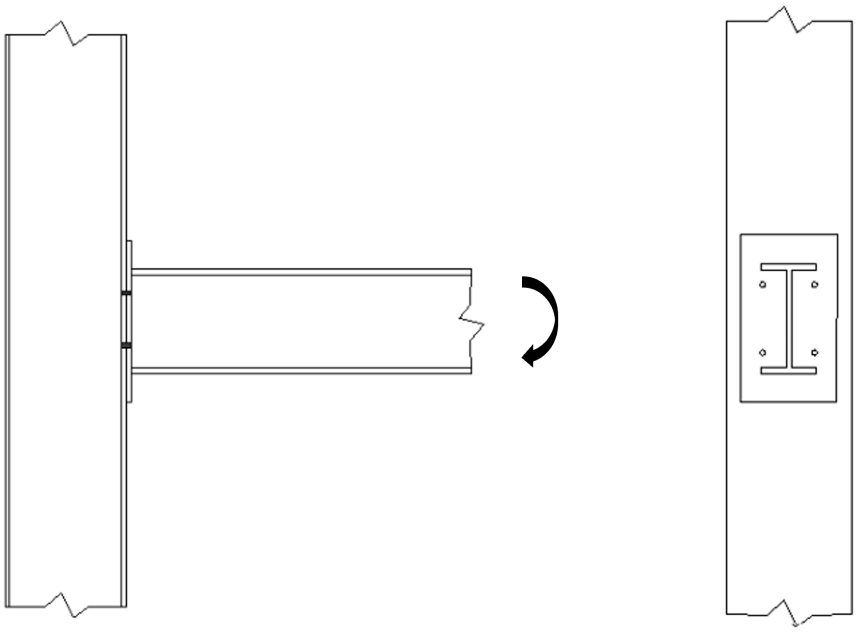

Figure 1.4: Beam-to-column joint [6]

This method can easily be extended to other joint configurations and loading scenarios.

(i) Identification of active components

When a bending moment is applied to the beam, the transfer of forces to the column occurs through several components. In this configuration, the active components, as illustrated in Figure 1.5, typically include:

- Bolts in tension (BT);
- Column flange in bending (CFB);
- End-plate in bending (EPB);
- Beam web in tension (BWT);
- Column web in tension (CWT);
- Column web panel in shear (CWS);
- Beam flange and web in compression (BFWC);
- Column web in compression (CWC).

The joint subjected to bending moment can be divided into two primary zones: the upper zone which develops tensile resistance, and the lower zone, which develops compressive resistance.

Compression zone

In the compression zone, load transfer occurs through direct contact between the beam flange and web (in compression) and the column web. This provides a straightforward and efficient load path. The mechanism can be generalized to a variety of joint types and loading scenarios.

Tension zone

In the tension zone, the force path starts at the top flange of the beam and passes through the end-plate, which undergoes bending. For rows with additional bolts, the beam web in tension provides stiffening and must be included in the mechanical model. The tensile force is transmitted through the bolts to the column flange, which also deforms in bending. Within the column, forces are further distributed through the column web in tension and the panel zone in shear.

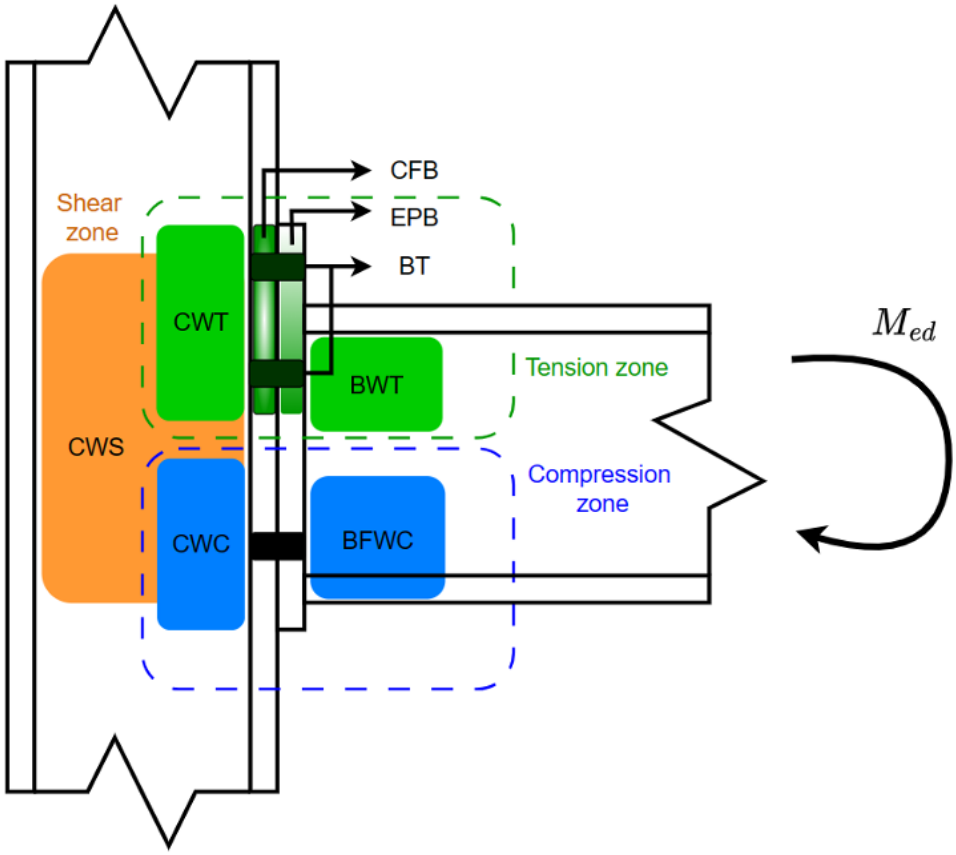

Figure 1.5: Beam-to-column joint : active component [4]

(ii) Characterization of each component

This step is not developed in detail here, as it is thoroughly covered in the Eurocode [5]. The outcome of this characterization is the representation of the behaviour of each individual component using equivalent mechanical elements, typically a dashpot or a tension spring. This idealization is illustrated in Figure 1.6.

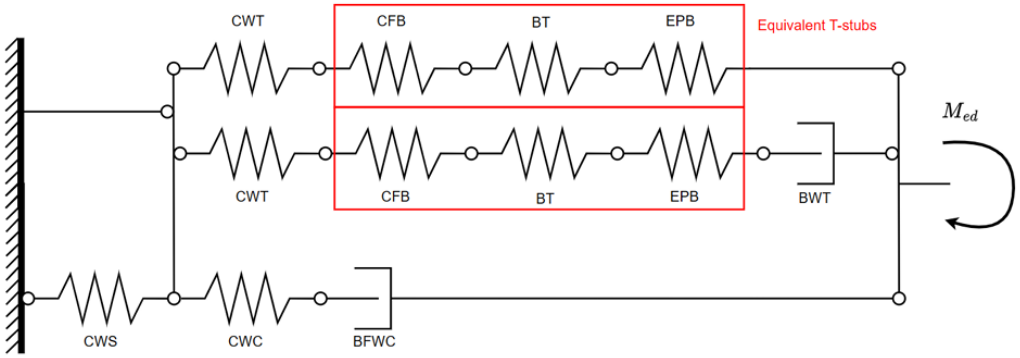

Figure 1.6: Beam-to-column joint : spring and dashpot model [4]

It is noteworthy that similar arrangements of components frequently appear in joint representations based on the component method. These can often be modeled using an equivalent T-stub. When the tension zone includes stiffening elements from the beam, a stiffened T-stub is considered.

Rigidity The initial stiffness of the joint is evaluated by modeling each structural component as an individual spring. The stiffness of each spring corresponds to that of its associated component. These springs – some in compression and others in tension – are arranged in series, as shown in Figure 1.7a. The equivalent stiffness of the system is then determined using the classical formula for springs in series:

$$k_{eq} = \frac{1}{\sum_i \frac{1}{k_i}} \tag{1.1}$$

This reduction leads to an equivalent system, as illustrated in Figure 1.7b. From this, the global rotational stiffness of the joint assembly is computed by summing the equivalent stiffnesses of individual load paths in parallel:

$$k_{assembly} = \sum_i k_{eq,i} \cdot z_i^2 \tag{1.2}$$

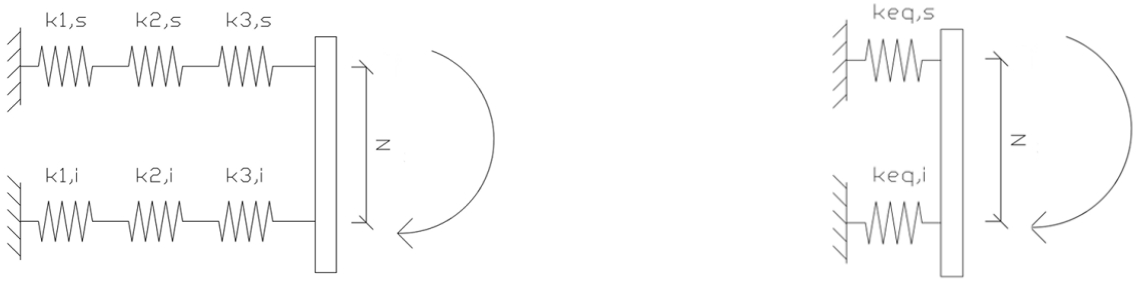

(a) Original spring configuration

(b) Equivalent spring configuration

Figure 1.7: Spring-based representation of a joint assembly [7]

To accurately describe joint behaviour, it is essential to determine both the initial stiffness and the strain-hardening stiffness. The latter represents the deformability of the joint in the range between the development of plastic resistance and the attainment of ultimate resistance. Figure 1.8 presents a typical moment-rotation curve, where K_i denotes the initial stiffness (previously referred to as $S_{j,init}$ in Figure 1.1) and K_{st} represents the strain-hardening stiffness.

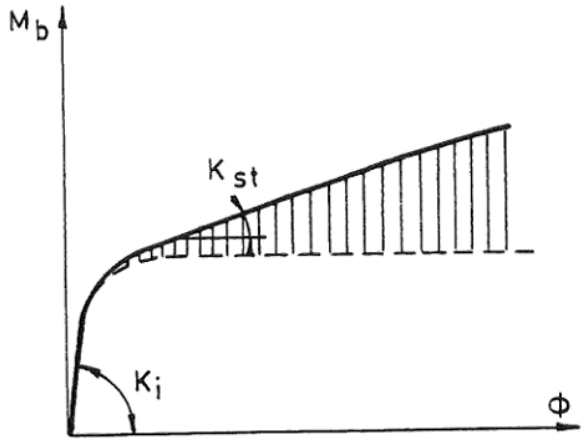

Figure 1.8: Example of a joint stiffness curve[8]

Resistance The strength of each component is evaluated individually in accordance with the provisions of the Eurocode, considering interaction and group effects where applicable (e.g. in flange or end-plate bending failures). The analysis follows an elastic-plastic approach with strain hardening, as proposed in the thesis of Professor J.-P. Jaspart [8]. This distinction enables differentiation between plastic and ultimate resistance for each component, which is modeled using a bilinear moment-rotation relationship.

(iii) Assembly of components

With steps 1 and 2 completed, all individual components are characterized in terms of stiffness and resistance. The third step involves assembling the components to derive the global joint response. This is achieved using the static theorem, which states that internal forces must be distributed in accordance with the following three conditions:

- Equilibrium between internal and external forces must be maintained.
- Plasticity criteria must be respected: each component must be capable of withstanding the internal forces to which it is subjected.
- Maximum deformability criteria must be fulfilled: the deformation capacity of any cross-sectional element must not be exceeded.
- Compatibility of displacements between the various components must be ensured.

These criteria are reflected in the assembly process, in which the individual springs are reduced into an effective equivalent spring, as shown in Figure 1.9.

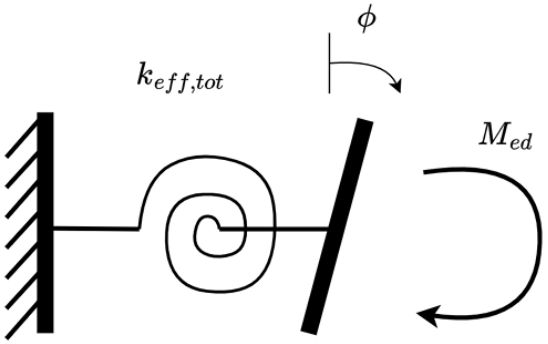

Figure 1.9: Simplified model of a "beam + joint" system [4]

Based on the explanations above, the joint response can now be clearly described and computed. This method is applicable in robustness analyses, where the joint is represented using linear or torsional equivalent springs. Moreover, the catenary effect – associated with large deformations and redistribution of forces – can also be accounted for through the ductility of the joint. However, activating this contribution requires a substantial reserve of ductility in the system.

1.2 The T-stub component

The T-stub component is a reference model prescribed by Eurocode 3 for the representation of flange and web behaviour under applied loads. This idealization allows the replacement of tension-loaded elements with an equivalent T-stub. The T-stub is connected by its flange to a theoretically rigid support and is subjected to tensile, flexural and shear loads.

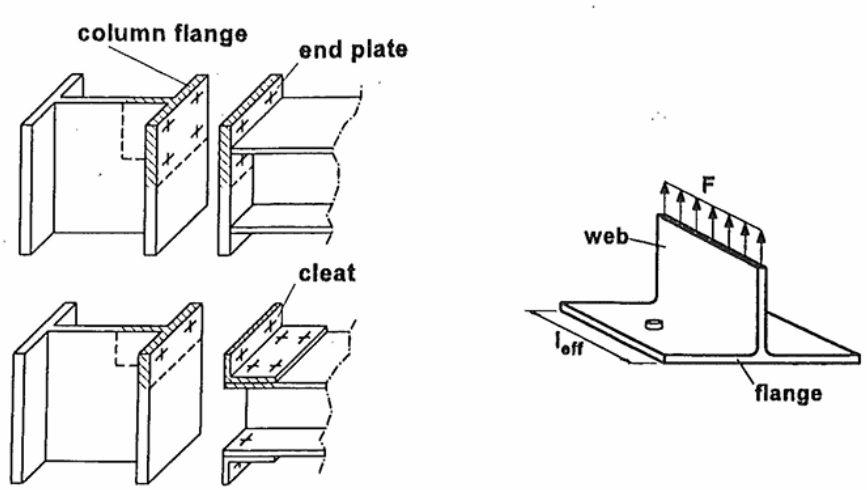

Figure 1.10: T-stub idealization [2]

The flange thickness of the T-stub corresponds to the physical thickness of the component it represents. However, its length is idealized as an effective length (ℓ_{eff}), which provides a resistance equivalent to that of the real component, as illustrated in Figure 1.10. This effective length is a theoretical construct and does not correspond to the actual physical length. It is determined based on various parameters detailed in Eurocode 3 [9].

The response of the idealized T-stub is primarily governed by the material properties and geometric configuration. The resistance of the T-stub under pure tension is computed using the formulae provided in **prEN 1993-1-8** [9].

Three principal failure modes are identified for T-stub components, and the plastic resistance of the T-stub is defined by the lowest resistance among them. These modes are defined as follows:

- **Mode 1:** Formation of a plastic mechanism.
- **Mode 2:** Mixed failure involving both bolt and flange deformation.
- **Mode 3:** Bolt failure, typically occurring in the presence of a thick flange.

Figure 1.11 illustrates the different failure modes of the T-stub. The distance n, at which the force Q is applied relative to the bolt axis, is defined as:

$$n = \min(e\,;\, 1.25m) \tag{1.3}$$

where:
- m is the distance between the considered weld toe and the bolt axis;
- e is the minimum edge distance measured from the bolt axis.

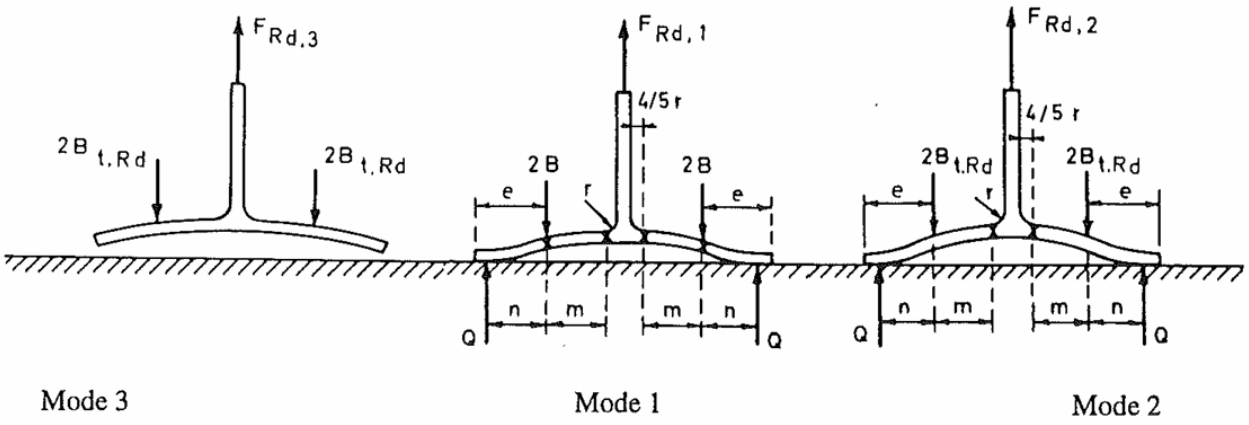

Figure 1.11: T-stub failure modes [2]

The ductility of the connection is influenced by the failure mode, as shown in Figure 1.12.

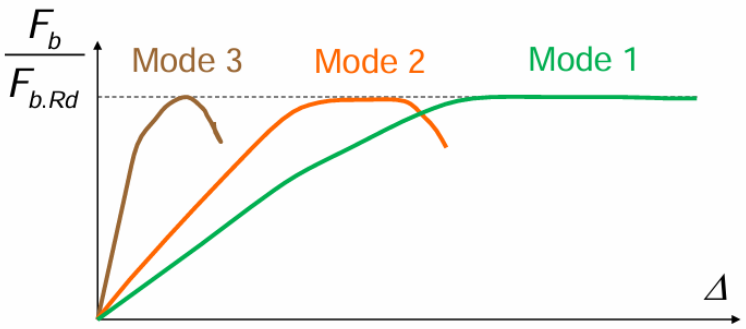

Figure 1.12: Ductility for different failure modes [10]

1.2.1 Mode 3:

When the T-stub flange is relatively thick compared to the bolts, failure tends to occur within the bolts themselves, typically by thread stripping or necking in the threaded region. This brittle failure mode is known as Mode 3 and is characterized by a brittle and sudden rupture. An illustration of this failure mode is provided in Figure 1.11, and the resistance is calculated as:

$$F_{T,3,Rd} = \sum B_{t,Rd} = \sum \frac{0.9 \cdot f_{ub} \cdot A_s}{\gamma_{M2}} \tag{1.4}$$

where:
- f_{ub} is the ultimate tensile strength of the bolt;
- A_s is the tensile stress area of the threaded portion of the bolt shank;
- γ_{M2} is the partial safety factor for the resistance of fasteners in tension, as defined in Eurocode [9];
- $B_{t,Rd}$ is the tensile resistance of an individual bolt.

1.2.2 Mode 2:

Mode 2 occurs due to bolt failure induced by prying action after plastic hinges form at the weld toe. The failure mode is illustrated in Figure 1.11 and the resistance is given by:

$$F_{T,2,Rd} = \frac{2M_{pl,2,Rd} + n \cdot B_{t,Rd}}{m+n} \tag{1.5}$$

where:

$$M_{pl,2,Rd} = \frac{0.25 \cdot \ell_{eff,2} \cdot t_f^2 \cdot f_y}{\gamma_{M2}} \tag{1.6}$$

- $M_{pl,2,Rd}$ is the plastic moment resistance associated with Mode 2;
- $\ell_{eff,2}$ is the effective length for plastic hinge development in Mode 2;
- t_f is the thickness of the T-stub flange;
- f_y is the yield strength of the steel;
- γ_{M2} is the partial safety factor for fracture resistance, according to Eurocode [9];
- m is the distance from the weld toe to the bolt axis;
- $n = \min(e\,;\, 1.25m)$ is the lever arm between the bolt axis and the line of action of the force Q.

1.2.3 Mode 1:

When the tensile capacity of the bolts exceeds the yield strength of the flange, plastic yielding begins at the weld toe, forming a plastic hinge. This generates prying forces at the edge of the flange, increasing the tensile demand on the bolts. If the flange is thin enough, bolt failure is unlikely, and a second plastic hinge may form near the bolt line, creating a fully developed plastic mechanism. This situation is referred to as Mode 1 failure.

The tensile resistance in this case, referred as **Method 1**, is calculated by:

$$F_{T,1,Rd} = \frac{4 \cdot M_{pl,1,Rd}}{m} \tag{1.7}$$

where:

$$M_{pl,1,Rd} = \frac{0.25 \cdot \ell_{eff,1} \cdot t_f^2 \cdot f_y}{\gamma_{M0}} \tag{1.8}$$

and:

- $M_{pl,1,Rd}$ is the plastic moment resistance for Mode 1;
- $\ell_{eff,1}$ is the effective length associated with Mode 1 plastic hinge formation;
- t_f is the thickness of the flange;
- f_y is the yield strength of the steel;
- γ_{M0} is the partial safety factor for the resistance of cross-sections, as specified in Eurocode [9].

Experimental comparisons have shown that the Eurocode formula for Mode 1 is often overly conservative. To address this, Professor Jaspart proposed a refined model for Mode 1, detailed in the annex 3 to his thesis [2], and further explained below.

- Accounting for bolt size:
  In the initial formulation, bolt forces are idealized as point loads, neglecting the physical dimensions of the bolt and washer. To provide a more realistic representation, the load transmitted by the bolt can be assumed to be linearly distributed over a width d_w, corresponding to the diameter of the bolt or washer. To simplify this distribution while maintaining accuracy, Professor Jaspart proposed an equivalent representation using two concentrated forces. These forces are applied symmetrically with respect to the bolt axis, each positioned at a distance e_w, as illustrated in Figure 1.13.

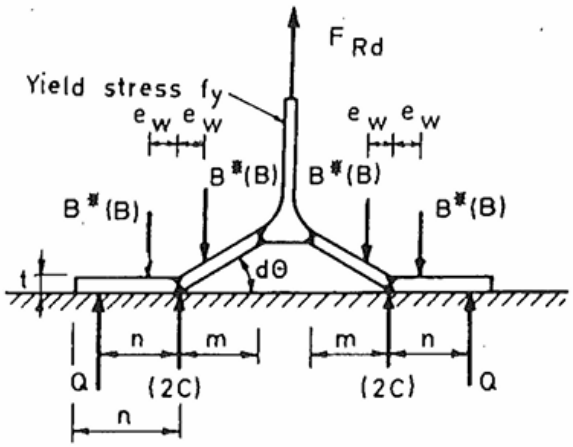

Figure 1.13: Modified T-stub accounting for bolt width [2]

Applying the virtual work principle and equilibrium conditions leads to a revised expression for the limiting force:

$$F_{Rd,1} = \frac{(8n - 2e_w)\ell_{eff,1} m_{pl,Rd}}{[2mn - e_w(m+n)]} \tag{1.9}$$

where $e_w = d_w/4$. This revised formulation is referred to as **Method 2**, while the original is referred to as **Method 1**.

- Accounting for bolt preloading:
  The original analytical model does not consider the influence of bolt preloading. However, in real assemblies, bolts are often preloaded during installation, which affects how forces are transmitted through the joint. When an external tensile force is applied, the initial increase in bolt tension is minimal, as it is balanced by a reduction in the compression between the flange and the base plate (noted 2C in Figure 1.13).

  This situation continues until the compressive force in the plates is entirely overcome, when $N = N_{bD}$ in Figure 1.14 at which point plate separation occurs. From this stage onward, the bolts carry the full external load, and the joint behaviour becomes statically determinate. This transition point is critical because it marks a change in the load transfer mechanism, which significantly influences joint resistance.

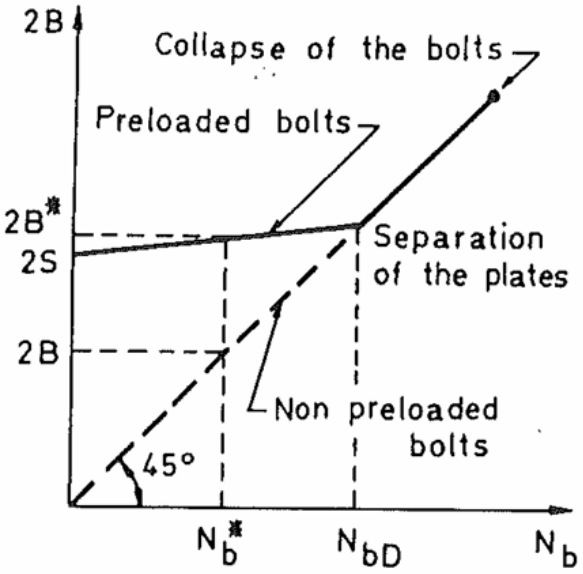

Figure 1.14: Bolt forces versus external loads [2]

Professor Jaspart introduced a refined model that accounts for this preloading effect by modifying the force distribution within the T-stub mechanism. His proposal results in a more realistic prediction of the joint resistance prior to plate separation and improves the accuracy of Mode 1 resistance evaluation. These refinements apply only to Mode 1 and do not affect the formulations for Modes 2 and 3.

1.2.4 Summary of the three Modes

The governing failure mode is the one corresponding to the minimum of the resistances calculated for the three possible modes:

$$F_{T,Rd} = \min\left(F_{T,1,Rd}\,;\, F_{T,2,Rd}\,;\, F_{T,3,Rd}\right) \tag{1.10}$$

1.3 Effective lengths

The parameter ℓ_{eff} appeared in the previous equations (1.6, 1.8, 1.9), yet it was not explained in detail. In fact, the effective length depends on the specific failure mode that develops within the T-stub component.

A T-stub is referred to as "short" when its actual length equals the effective length ($L = \ell_{eff,i}$). In this configuration, the yield mechanism is characterized by two straight plastic hinges forming at the bolt holes and the weld toe, as illustrated in Figure 1.15b.

As previously mentioned, the concept of effective length enables the simplification of complex, real-world T-stub geometries into idealized models with representative plastic mechanisms. The mechanisms discussed here are limited to configurations with a single bolt row, which correspond to the configurations investigated in this thesis. This approach was first developed by Zoetemeijer [11], whose work established the foundation for the widely accepted plastic deformation mechanisms and corresponding effective lengths.

These mechanisms are illustrated in Figure 1.15, with their respective expressions given below:

$$\text{From Figure 1.15a} \quad \ell_{eff,nc1} = 4m + 1.25n \tag{1.11}$$

$$\text{From Figure 1.15b} \quad \ell_{eff,nc2} = L \tag{1.12}$$

$$\text{From Figure 1.15c} \quad \ell_{eff,cp} = 2\pi m \tag{1.13}$$

Here, "nc" refers to "non-circular pattern" and "cp" to "circular pattern".

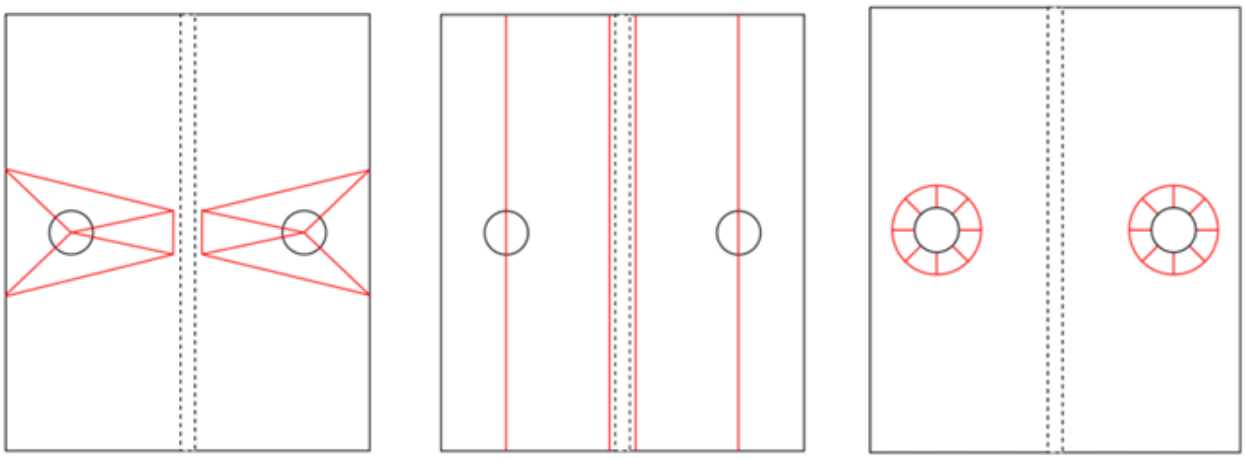

(a) (b) (c)

Figure 1.15: Effective lengths for typical plastic mechanisms [4]

In addition to these expressions, two refined effective lengths were introduced by Warnant [6]. Although not included in Eurocode provisions, these lengths are proposed for their improved accuracy when modeling isolated T-stubs. The proposed expressions are:

$$\ell_{eff,nc,W} = \frac{L \cdot m}{2(m+n)} + m \cdot \left(0.0876 \left(\frac{n}{m}\right)^3 - 0.6816 \left(\frac{n}{m}\right)^2 + 3.1143\frac{n}{m} + 0.9786\right) \tag{1.14}$$

$$\ell_{eff,c,W} = \frac{2L - 2m + \pi m}{2} \tag{1.15}$$

Equations 1.14 and 1.15 correspond respectively to the configurations illustrated in Figures 1.16a and 1.16b below.

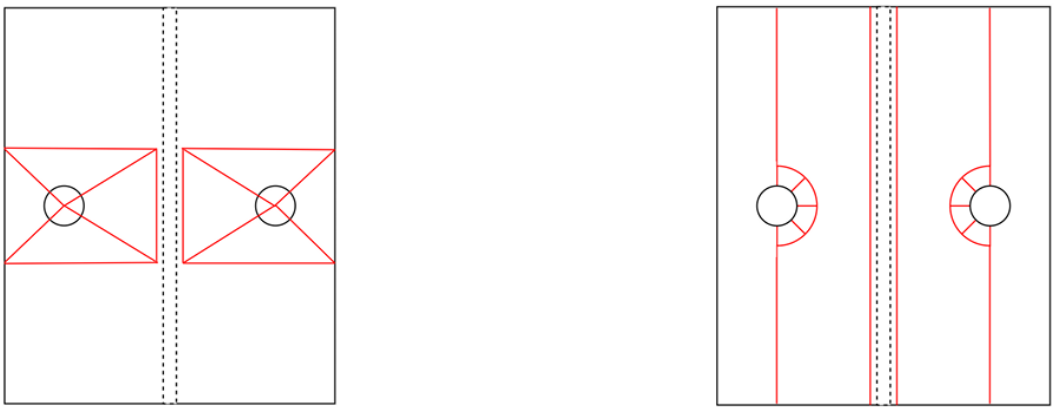

(a) (b)

Figure 1.16: Effective lengths proposed by Warnant [4]

Among all possible mechanisms, the one with the smallest effective length is the most likely to occur, as it corresponds to the minimum plastic dissipation energy. It should be noted that circular yielding patterns are not applicable to Mode 2 failure. This is because Mode 2 involves the formation of a single plastic hinge at the weld toe, followed by bolt failure due to prying. Since no second plastic hinge forms near the bolt, there is no extended plastic region between the weld and bolt where a circular yielding pattern could develop – as is the case in Mode 1.

Consequently, the final expressions for the effective lengths used in Mode 1 and Mode 2 analyses are:

$$\ell_{eff,1} = \min\left(\ell_{eff,nc1},\, \ell_{eff,nc2},\, \ell_{eff,cp},\, \ell_{eff,nc,W},\, \ell_{eff,c,W}\right) \tag{1.16}$$

$$\ell_{eff,2} = \min\left(\ell_{eff,nc1},\, \ell_{eff,nc2},\, \ell_{eff,nc,W}\right) \tag{1.17}$$

1.4 Conclusion of the state of the art

This chapter has provided a comprehensive overview of the theoretical background necessary to analytically describe the behaviour of the T-stub component, which plays a key role in the mechanical performance of bolted assemblies. Understanding the contribution of each individual component is essential for accurately characterizing the global response of the joint.

The fundamentals of the component method were reviewed, including the identification of active zones (tension and compression), the mechanical characterization of each component in terms of stiffness and resistance, and their subsequent assembly into a global model. Particular attention was devoted to the T-stub, which represents the tensile behaviour of end-plate joints. The behaviour of this component was analyzed through the classification of three primary failure modes and their associated plastic mechanisms.

Two distinct approaches were presented for evaluating the plastic resistance of Mode 1:

- **Method 1**: Evaluation without considering bolt-specific effects such as diameter and preloading;
- **Method 2**: An improved formulation accounting for bolt geometry and preload, as proposed by Jaspart.

The concept of effective length was also introduced as a mean to idealize complex T-stub deformations through simplified plastic mechanisms. Several models, including those proposed by Zoetemeijer and Warnant, were presented and compared.

The next chapter applies the theoretical framework developed here to experimental results obtained at the University of Trento, with particular focus on the work of Valerio Mancini [3]. The study investigates T-stub behaviour under combined axial and shear loading, which represents the central topic of this thesis.

Chapter 2

Experimental results from the literature

The case study analyzed by Mancini [3] was carried out in collaboration with several universities, including the Universities of Trento, Brescia, Padova, Trieste, Udine, and IUAV of Venezia. As mentioned in the introduction, the difficulty in addressing accidental loading scenarios was the motivation behind a more in-depth investigation into structural robustness.

One of the reference projects is titled *"Robust Structures by Joint Ductility"*, funded by the European Community. This research focuses on the sudden loss of an internal column in a building due to an accidental event. The aim of the project is to investigate progressive collapse mechanisms that may be triggered by the development of membrane effects within structural members. This leads to a transition in the beam-to-column connection response, from a combination of bending and shear to a combination of axial tension and shear forces.

A high degree of plastic deformability (ductility) is required for all structural elements and joints subjected to combined axial, bending and shear actions.

The reference building used in this research consists solely of HEA 160 profiles for the columns and IPE 140 profiles for the beams, the structure is shown in Figure 2.1.

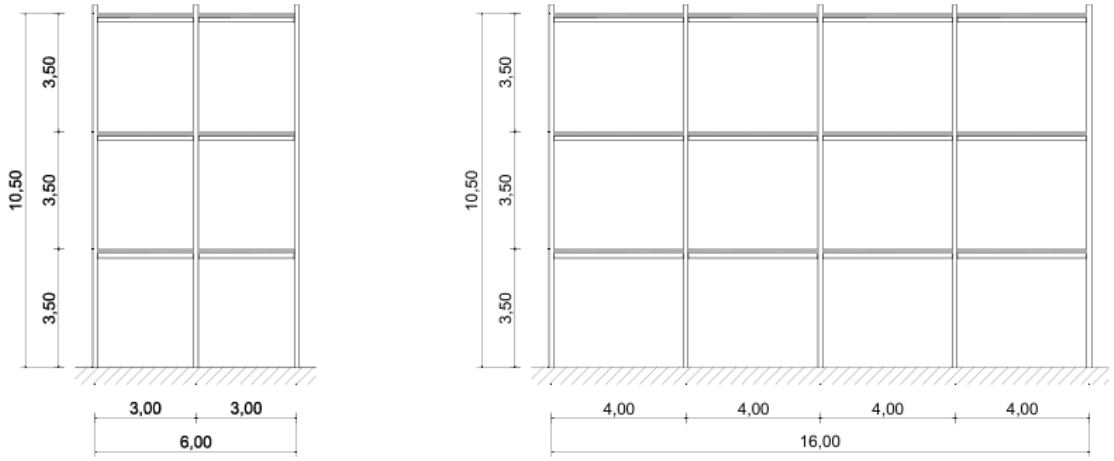

Figure 2.1: Reference building of the research project *"Robust Structures by Joint Ductility"* [12]

Note: The two views shown are perpendicular projections of the same structure, presented to illustrate its geometry from different angles.

The steel grade used for all components is S355. In this structure, the beam-to-column connections are composed of an end-plate with a thickness of 8 mm, welded to the beam and bolted to the column flange using four preloaded grade 8.8 bolts. The bolts are tightened with a torque of 350 N.m.

The main results analyzed in the present thesis are based on the tests conducted at the University of Trento [3], which focused on investigating the behaviour of individual steel and concrete components of the joint under uniaxial or combined loading conditions.

Different universities involved in the project addressed distinct aspects of the experimental program. Substructure tests were carried out at the University of Liege, while joint tests – focused on moment-rotation (M-Φ) and moment-axial force (M-N) interaction curves – were performed at the University of Stuttgart. The University of Trento concentrated on the behaviour of basic joint components in steel and concrete, including unstiffened and stiffened T-stub specimens.

Specifically, the "end-plate T-stub connected to the column" was tested under pure tension, whereas the "full steel connection on a rigid support" and the "full steel connection on the column" were tested under various combinations of bending moment (M), axial force (N) and shear force (V). An example of a test setup for a reference steel connection is illustrated in Figure 2.2.

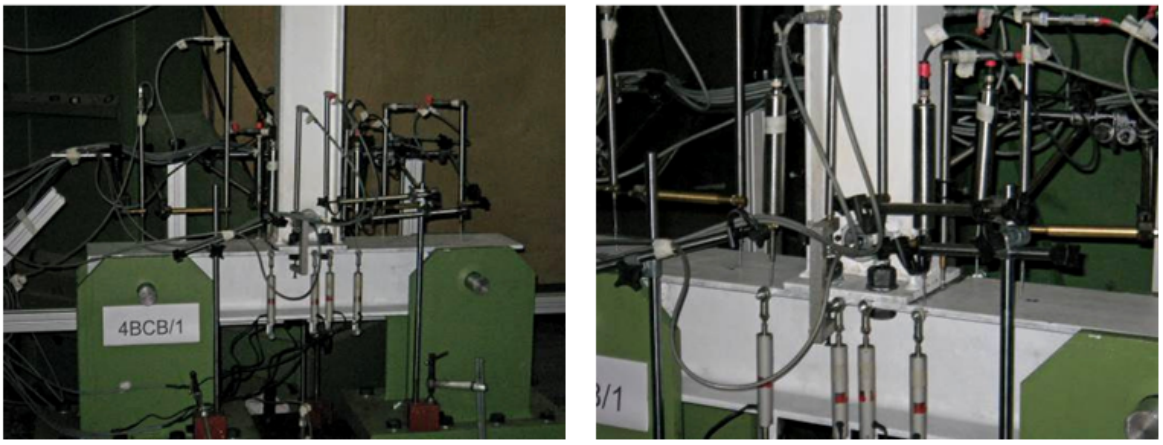

Figure 2.2: Test on reference steel connection (adapted from [3])

These experimental investigations serve as the foundation for developing detailed guidelines aimed at ensuring adequate structural safety, including resistance to accidental loads and prevention of progressive collapse.

2.1 T-stub under combined axial and shear loads : Trento

2.1.1 Specimens

In the experimental campaign conducted at the University of Trento, a wide range of specimens with varying geometries were tested. Among the 95 experiments performed, two primary types of tests were conducted:

- Tests on stiffened T-stubs, aimed at evaluating the influence of stiffening elements;
- Tests on unstiffened T-stubs, subjected to either pure axial loading or combined axial and shear loading conditions.

The investigated joints included both steel-concrete composite connections and fully steel connections. Only the latter are relevant to the present study.

The specimen considered in this thesis is a T-stub cut from a HEA 160 profile. It is connected to a rigid support using two M20 class 8.8 bolts inserted into holes with a diameter of $d_0 = 22\,\text{mm}$. The web of the T-stub is reinforced on both sides with welded steel plates measuring $100 \times 256 \times 5\,\text{mm}$, in order to increase its stiffness and prevent undesired failure mechanisms in the web that are not relevant to the objectives of the test. Additionally, the web is fastened by three steel pins with a diameter of 30 mm.

The configuration is illustrated in Figure 2.3:

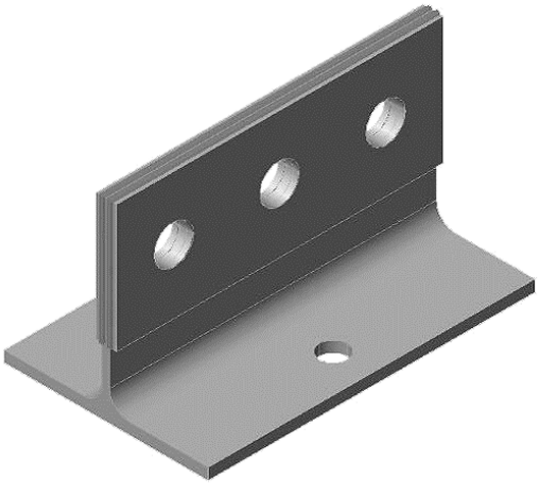

Figure 2.3: Column T-stub specimen

The dimensions of the T-stub used in the calculations are derived from the ArcelorMittal catalog [13] and are 256x152x160 mm. The bolts are of grade 8.8, type HR, and consist of both threaded and unthreaded portions.

The geometric properties of the original specimen, made from an HEA 160 profile and referred to as 1CC, are illustrated in Figure 2.4 and summarized in Table 2.1.

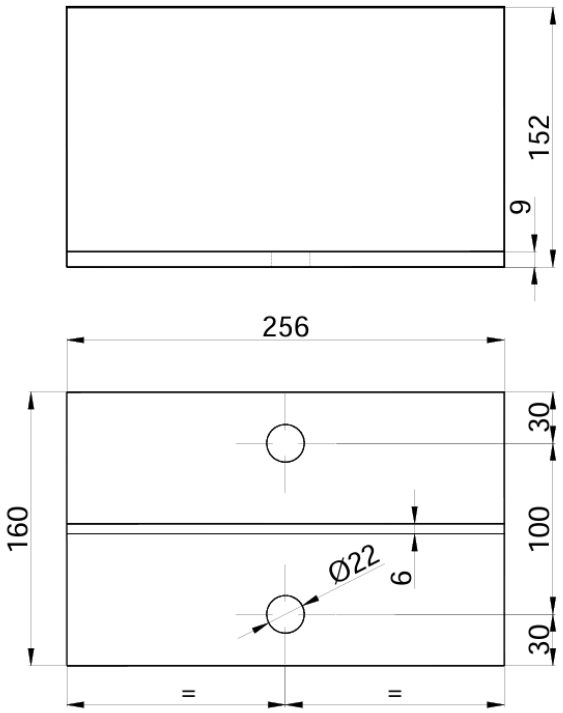

Figure 2.4: 1CC Test geometry (dimensions in mm)

Some geometric clarifications are required to compute the parameters related to the T-stub section. The T-stub has a width of 160 mm, denoted as w, which is used to determine the parameter m – the distance between the considered weld toe and the bolt axis – calculated using Equation 2.1.

The weld radius is taken as 0.8 times the profile radius [2]. Given a nominal radius of 15 mm for a HEA 160 section, the considered value becomes:

$$r_{\text{considered}} = 0.8 \cdot 15 = 12\,\text{mm}$$

The minimum edge distance is denoted as $e_{\text{min}} = 30\,\text{mm}$, and the web thickness is $t_w = 6\,\text{mm}$. Based on these values, the parameter m can be derived from the total width as follows:

$$160 = (e_{\text{min}} + m + r_{\text{considered}}) \cdot 2 + t_f \tag{2.1}$$

$$m = \frac{160 - t_f}{2} - e_{\text{min}} - r_{\text{considered}} \tag{2.2}$$

$$m = \frac{160 - 6}{2} - 30 - 12 = 35\,\text{mm} \tag{2.3}$$

The distance "n" – defined as the distance from the edge of the T-stub to the axis of the bolt hole, measured from the bolt axis – can be calculated using Jaspart's formula as follows:

$$n = \min\left(e_{\text{min}}; 1.25\,m\right) \tag{2.4}$$

$$= \min\left(30\,; 1.25 \cdot 35\,\right) = 30\,\text{mm} \tag{2.5}$$

This value is determined based on assumptions that are valid only within the elastic range.

In the Table 2.1 the geometrical values of the T-stub specimen 1CC are summarized.

parameter	value	unit
m	35	mm
n	30	mm
w	160	mm
L	256	mm
t_f	9	mm
t_w	6	mm
d_0	22	mm

Table 2.1: Geometrical properties of T-stub specimen 1CC

Note: The T-stub 1CB, used for pure tensile tests, has exactly the same geometrical properties as the T-stub 1CC.

2.1.2 Tests under axial and shear load: set-up and procedure

To investigate the behaviour of the T-stub under varying combinations of axial and shear forces, a custom test setup was developed. It consisted of two curved box-section frames, with the specimen acting as the link between the upper and lower parts. The flange was connected to the upper frame using two M20 class 8.8 bolts, while the web was fixed to the lower part through three pins of 30 mm diameter. By adjusting the pin location connecting the box sections to the actuator and the laboratory floor, various loading conditions could be achieved through rotation of the setup, as illustrated in Figure 2.5. The loading angle φ was defined based on the axial (N) and shear (V) components of the applied force F:

$$\varphi = \arctan\left(\frac{N}{V}\right) \tag{2.6}$$

An angle of $\varphi = 0°$ corresponded to pure shear, by increasing φ (by steps of 15°) the axial force component was progressively increasing. The test setup was specifically designed to eliminate any bending moment on the specimen during loading.

Figure 2.5: Testing apparatus for T-stub tested under axial and shear force [14]

Figure 2.6 illustrates different combinations of axial and shear forces, corresponding to inclination angles of 0°, 30°, 45°, and 60°, from left to right.

Figure 2.6: Tests on T-stub under different angles of inclination [14]

To monitor the deformation of the specimens, a total of fourteen displacement transducers were employed (Figure 2.7). Two transducers measured displacements parallel to the T-stub flange (TR01 and TR02), corresponding to the shear response, while the remaining twelve transducers (from TR03 to TR14) recorded displacements perpendicular to the flange, associated with the tensile behaviour. On the Figure 2.7, the transducers set-up is represented.

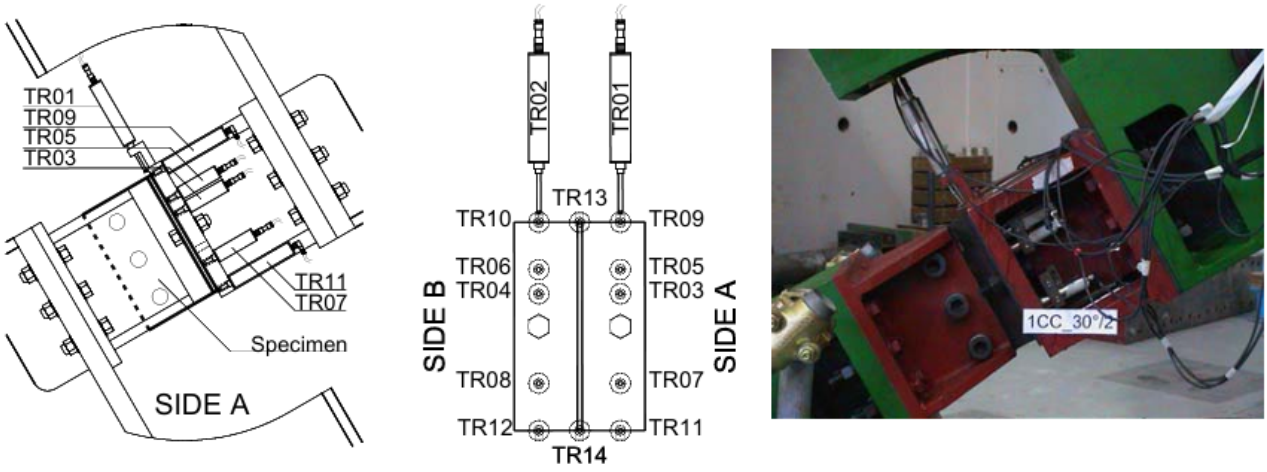

Figure 2.7: Tests on T-stub - transducers set-up [14]

It should be noted that due to the geometric and mechanical constraints of the test apparatus, pure tensile loading ($\varphi = 90°$) could not be achieved. As shown in Figures 2.5 and 2.6, the setup could not be rotated to a full 90° position, which prevented the execution of tests under pure axial tension. These tests were therefore conducted using a separate experimental configuration designed to monitor the corresponding displacement behaviour. The specimen used for this test shares the same material properties and geometric dimensions as the 1CC specimen but is designated as 1CB.

2.1.3 Material tests and properties

Some tests were performed on the materials to predict their behaviour.

- **Tests on steel plates**
  The results of the tests conducted on the steel specimens are presented in Table 2.2. These include the plastic and ultimate resistance values for the various T-stub configurations.

specimen	f_y [MPa]	f_u [MPa]
1CC	392.2	523.2

Table 2.2: Strength characteristics for Trento tests, steel plates

- **Tensile tests on bolts**
  Tensile tests were conducted on M20 bolts of class 8.8 under two preloading conditions: snug-tight and a preload force of 125 kN, corresponding to a tightening torque of 350 Nm. During testing, the elongation of the bolt shank was monitored using a strain gauge transducer with a travel capacity of 2.5 mm and an accuracy of 0.1%. The transducer was removed upon reaching the maximum load. The resulting load-elongation relationships were interpolated using polynomial functions, providing an accurate fit to the experimental data illustrated in Figure 2.8. As expected, the preload condition had minimal influence on the collapse strength, with the average failure load recorded at 228.829 kN for class 8.8 bolts.

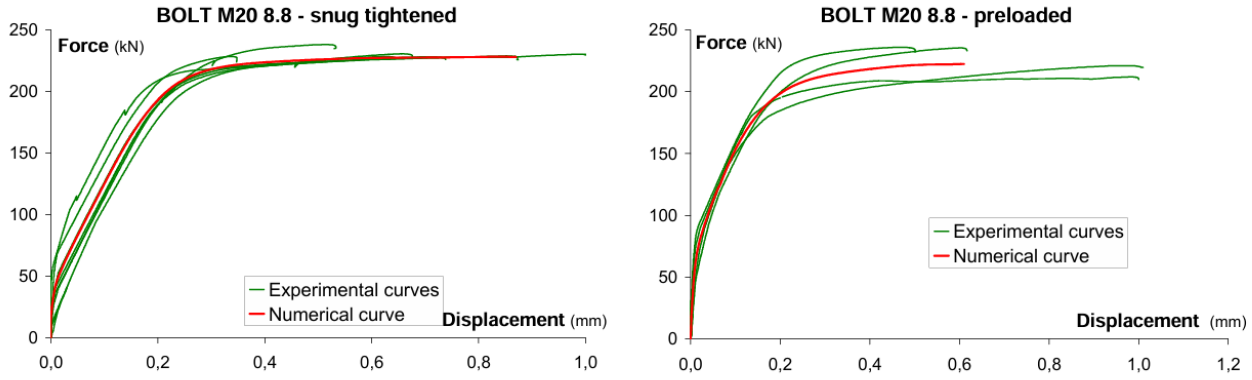

Figure 2.8: Load-displacement curves for bolts M20 class 8.8 [14]

2.1.4 T-stub test results

All sixteen T-stub specimens (1CC series) were successfully tested, with failure mode 1 consistently occurring due to bolt rupture.

Although displacement data from all transducers were recorded and processed, this analysis focuses specifically on transducers TR13 and TR14 – positioned at the ends of the flange – to evaluate displacements perpendicular to the flange. In addition, the transducers TR01 and TR02, which measure displacements parallel to the T-stub flange, are also considered. This selection is guided by the study of Mancini, which offers the most detailed analysis of these particular transducers and provides the most thoroughly documented corresponding Abaqus simulations.

- **Results for transducers 13 and 14 (TR13-14)**

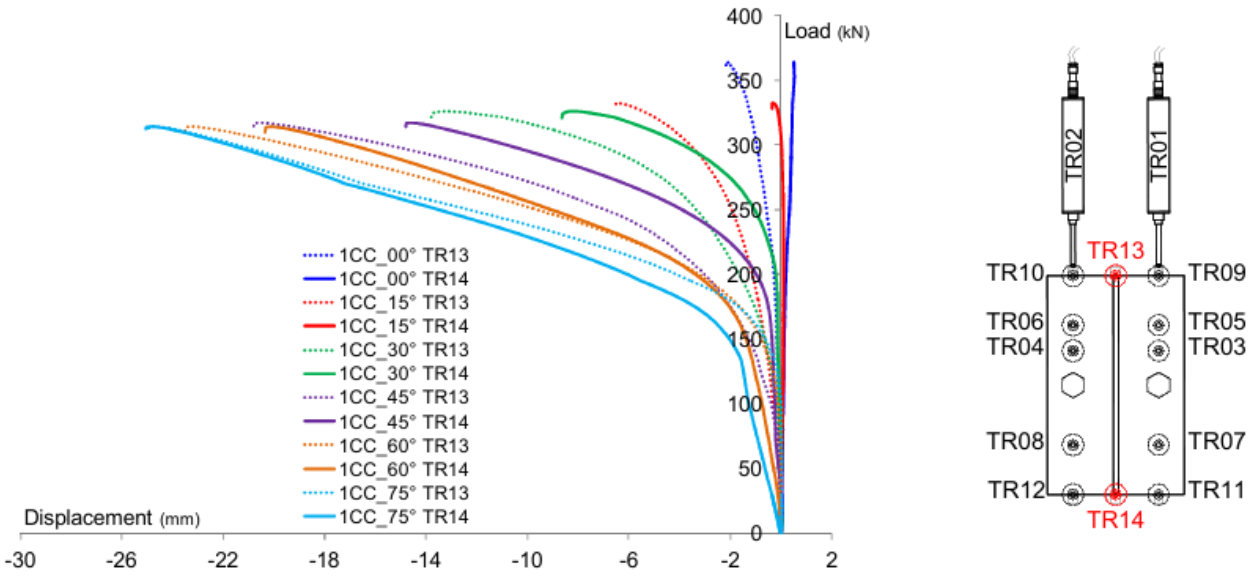

Figure 2.9: Load-displacement curves for different φ values, for transducers TR13 and TR14 [3]

Displacement measurements from transducers TR13 and TR14, located at opposite ends of the T-stub flange, highlighted a decreasing asymmetry in flange deformation with increasing inclination angle φ. At $\varphi = 75°$, the flange behaviour appears nearly symmetric. Transverse displacements were

also recorded at $\varphi = 0°$, likely due to parasitic bending moments caused by the gradual deformation of bolts and the flange, slightly shifting the resultant load. Nevertheless, this effect remains limited: the average displacement difference between TR13 and TR14 at collapse is under 2 mm for $\varphi = 0°$, while it reaches approximately 5 mm for $15° < \varphi < 45°$. From $\varphi = 60°$ onwards, the increasing dominance of the axial force further reduces the asymmetry.

- **Results for transducers 01 and 02 (TR02-02)**

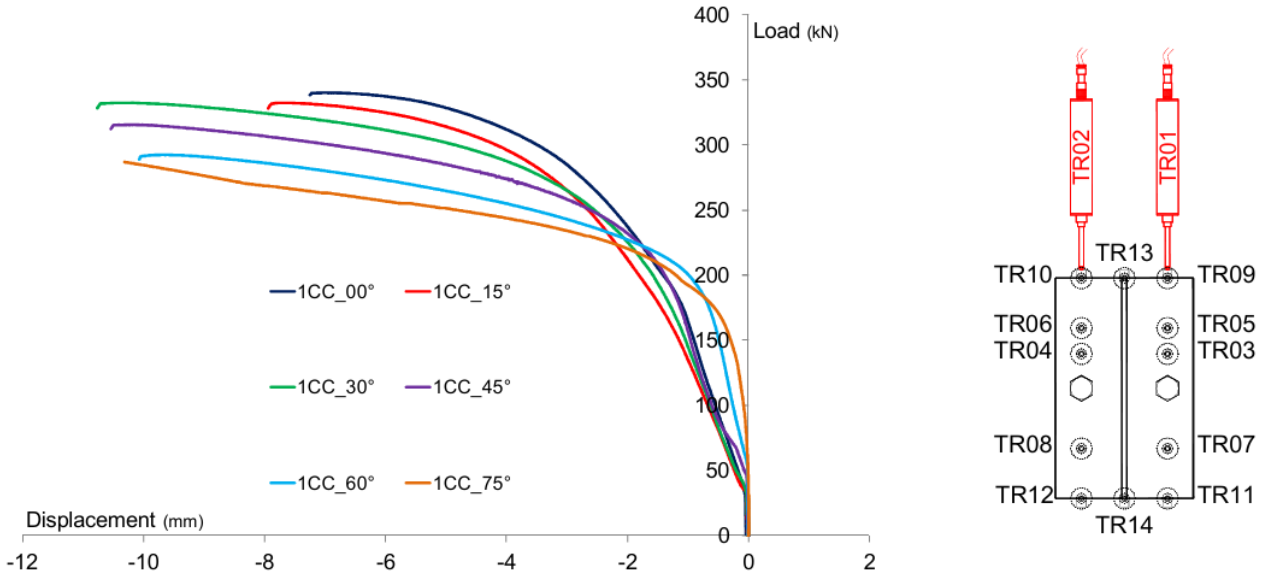

Figure 2.10: Load-displacement curves for different φ values, for transducers TR01 and TR02 [3]

The load-displacement curves recorded by transducers TR01 and TR02 (Figure 2.10) indicate a general trend of decreasing stiffness with increasing load inclination angle φ, reflecting a shift in the load transfer mechanism. For inclination angles $0° \leq \varphi \leq 30°$, where shear dominates over axial force, the initial stiffness remains relatively consistent across tests, and failure is primarily driven by bearing and shear fracture of the bolt shanks. In contrast, for $\varphi > 45°$, the curves show a stiffer initial response due to restrained longitudinal displacements of the T-stub flange. Notably, the largest displacements at failure occur in tests with $30° \leq \varphi \leq 75°$. For angles $\varphi \geq 60°$, a slow initial displacement is followed by a sudden increase around 200 kN, attributed to the formation of a plastic mechanism in the flange and specific characteristics of the displacement acquisition system.

- **Deformation of specimen components**
  Deformations varied with the loading angle, showing more pronounced bending and flange deformation at higher inclination angles. Displacement measurements confirmed that maximum flange deformation occurred at its extremities. Additionally, shear forces introduced asymmetry in the deformation, particularly at lower inclination angles, affecting the overall deformation behaviour.

Figures below present the bolts, bolt holes and specimen flange deformations observed at failure for several tests performed on the specimen.

(a) 1CC_00° - pure shear (b) 1CC_60°

Figure 2.11: Bolts deformations at collapse [3]

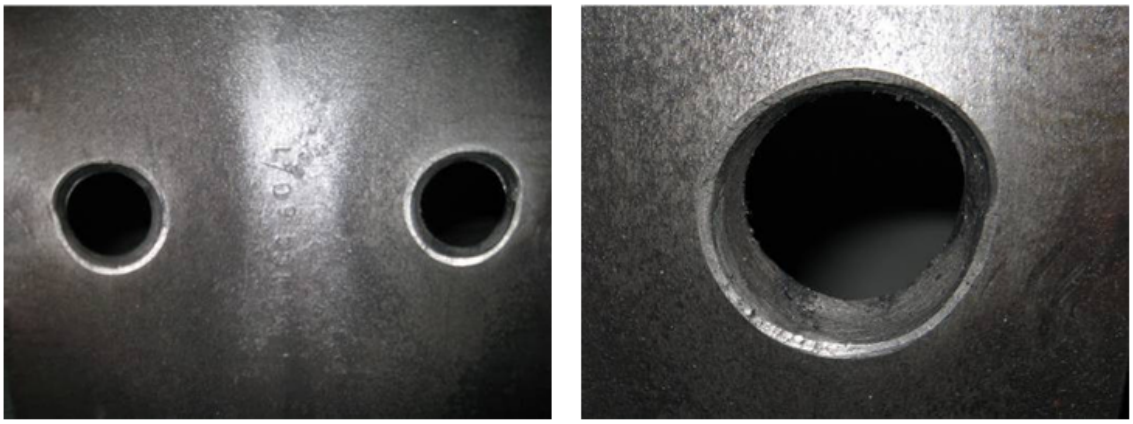

Figure 2.12: Deformation of bolt holes at collapse [3]

Note: The inclination angle is not provided for the pictures shown.

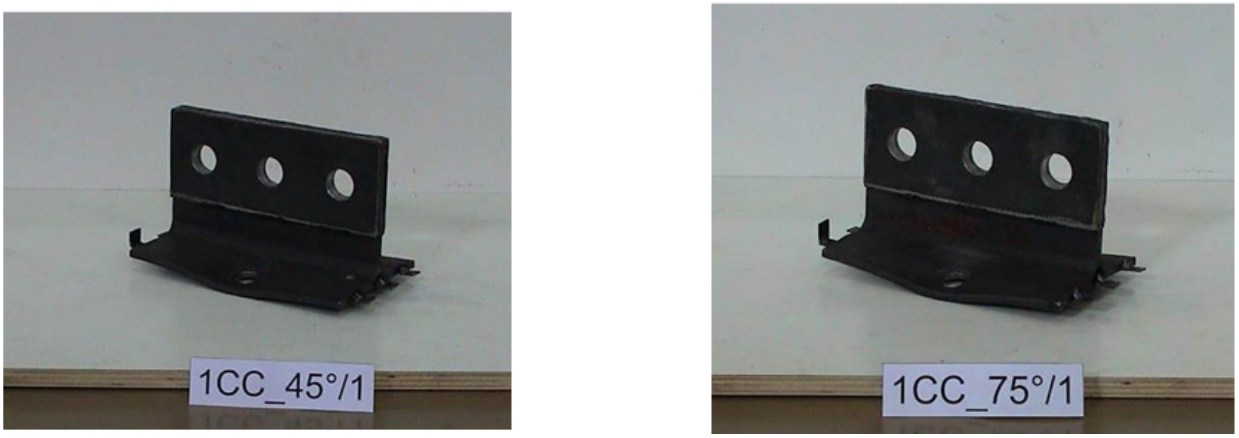

(a) (b)

Figure 2.13: Specimen flanges deformation at collapse [3]

- **Graphical representation of the results**

Table 2.3 presents the average collapse loads obtained from the tests. A graphical representation of these results is shown in Figures 2.14 and 2.15.

Test angle (deg)	Collapse load (kN)	Axial component (kN)	Shear component (kN)
0	352.55	0.00	352.55
15	334.40	86.55	323.01
30	329.20	164.60	285.10
45	316.08	223.50	223.50
60	314.44	272.31	157.22
75	305.00	294.61	78.94
90	285.728	285.728	0.00

Table 2.3: T-stub experimental collapse loads

In both figures, the red markers correspond to experimental data, while the blue lines illustrate the average trend between the horizontal and vertical axis values.

Figure 2.14 illustrates how the total failure load (F) varies with the inclination angle φ of the applied load.

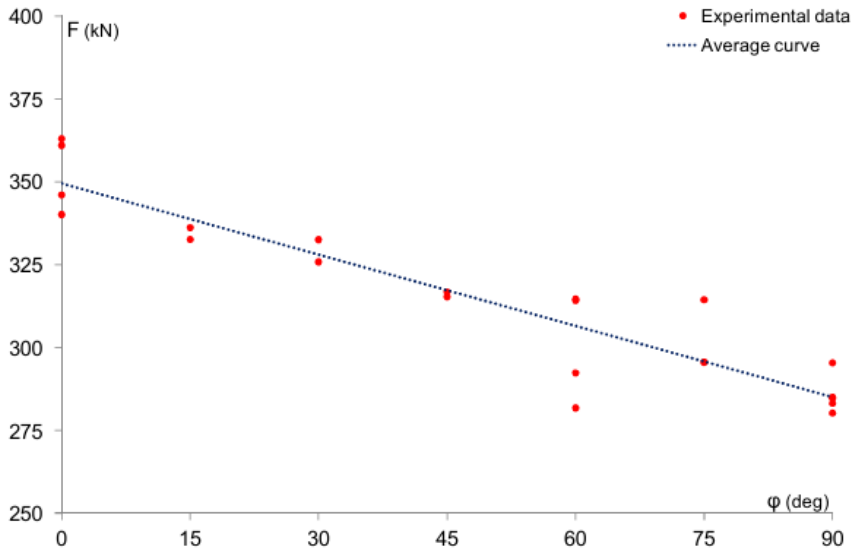

Figure 2.14: Collapse loads vs. inclination angles φ [3]

Figure 2.15 depicts the relationship between the axial (N) and shear (V) components of the load F at collapse.

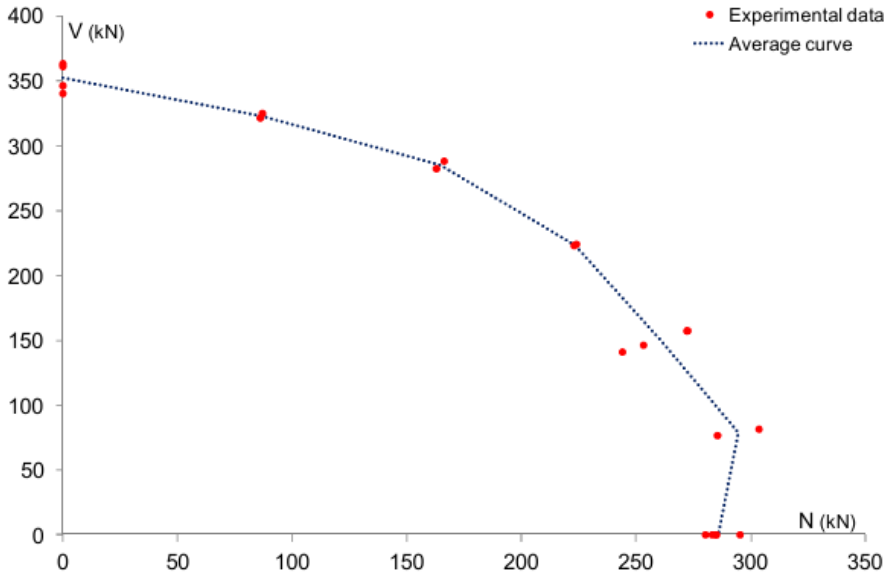

Figure 2.15: Axial vs. shear component of collapse loads [3]

The results indicate a notable interaction between axial and shear forces. As shown in Figure 2.14, the total failure load decreases approximately linearly, with a reduction of about 11 kN for every increase of 15° in the inclination angle [3].

Chapter 3

Analytical calculations

Analytical calculations are conducted to assess whether existing design codes adequately capture the complex behaviour and accurately predict the resistance observed in the experimental results from Trento, presented in Section 2.

3.1 Introduction

The dimensions of the T-stub and the bolt type considered in this study have already been presented in Section 2.1.1. The bolt has both a threaded and an unthreaded portion. The gross cross-sectional area of the unthreaded portion is calculated as:

$$A = \frac{\pi \cdot d^2}{4} = \frac{\pi \cdot 20^2}{4} = 314.159\,\text{mm}^2 \tag{3.1}$$

The standard refers to ISO 898-1 for the value of A_s, which represents the tensile stress area of the threaded portion and is defined as:

$$A_s = 0.78 \cdot A = 0.78 \cdot 314.159 = 245.04\,\text{mm}^2 \tag{3.2}$$

Based on the previously calculated cross-sectional area, the ultimate engineering tensile strength can now be determined. The average measured collapse load for M20 grade 8.8 bolts was 228,829 kN [14]. Using the tensile stress area of the threaded portion of the bolt ($A_s = 245.04\,\text{mm}^2$), the ultimate tensile strength is calculated as:

$$f_{ub} = \frac{228\,829}{245.04} = 933.83\,\text{MPa} \tag{3.3}$$

The reference case examined corresponds to the 1CC specimen from Mancini's testing campaign, illustrated in Figure 2.4.

The washers are modeled based on EN 14399-6 (M20) from the FATOR catalog [15], with dimensions given in Section 4.1.1, including a thickness of 4 mm.

3.1.1 T-stub geometry parameter

All relevant geometric parameters of the T-stub have already been detailed in Section 2.1.1. In addition, the yield strength f_y and ultimate tensile strength f_u of the material are provided in the study by Baldassino [14], with the following values:

$$f_y = 392.2\,\text{MPa} \tag{3.4}$$

$$f_u = 523.2\,\text{MPa} \tag{3.5}$$

3.1.2 Bolt geometry parameter

The bolts are of grade 8.8, type HR, and consist of both threaded and unthreaded portion. None information was provided to fix the dimension details. The only available information to define the bolt geometry is based on Figure in Mancini's work [3] in his modelling part, illustrated in Figure 3.1a. All the values of the measured geometrical dimensions are illustrated in Figure 3.1b.

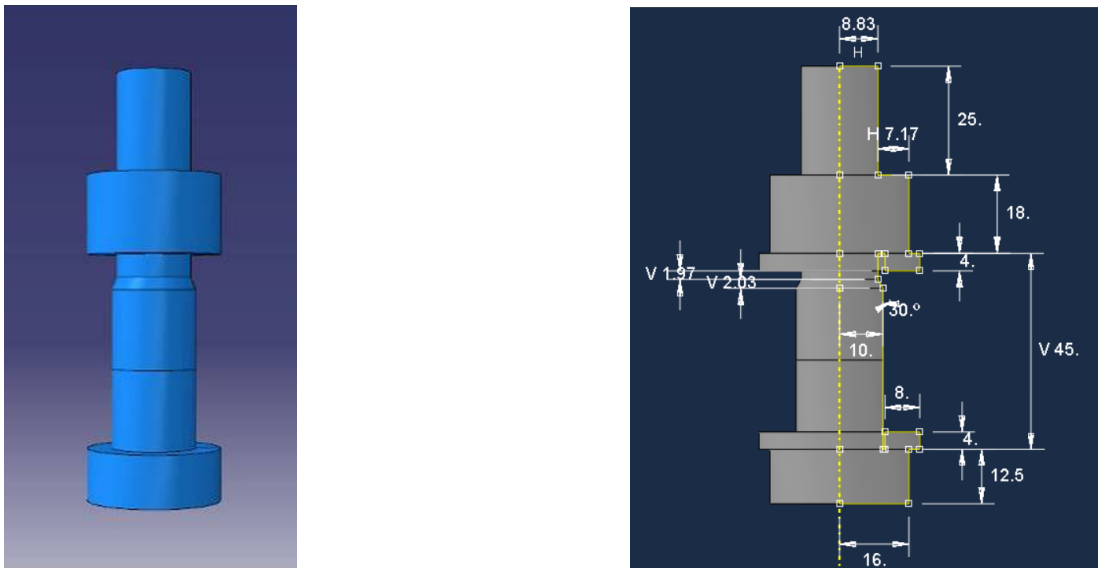

(a) Figure of bolt geometry provided by Mancini [3] (b) Bolt dimensions

Figure 3.1: Bolt geometry parameter

In Mancinis work, the washer was modelled as a separate part, whereas in the present study, it is integrated with the bolt. The washers are based on the specifications of EN 14399-6 (M20) from the FATOR catalog [15], with dimensions: internal diameter = 21 mm, external diameter = 37 mm and thickness = 4 mm.

3.1.3 T-stub and forces

When a T-stub is subjected to tension, different forces arise. The following figure illustrates these forces:

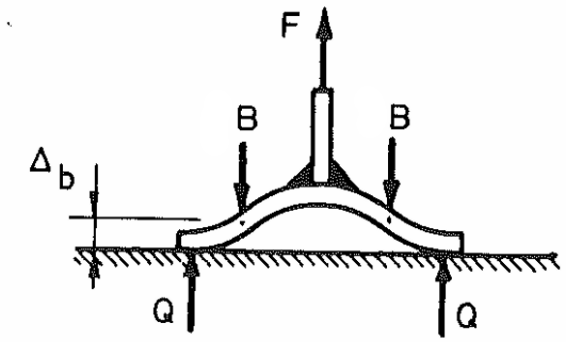

Figure 3.2: T-stub deformability and associated forces [2]

In this context:

- **F** represents the tensile force applied to the web of the T-stub.
- **B** corresponds to the force acting on each bolt.
- **Q** is the prying force between the flange of the T-stub and the rigid foundation (in this case study).

The prying force **Q** is assumed to act as a point load, located at 75% of the distance "n" [16].

Two different mechanical configurations can arise:

- Case 1: No plastic hinge forms at the weld between the web and the flange (elastic response).
- Case 2: Two plastic hinges formed on each side of the weld between the web and the flange.

The two cases are illustrated in Figure 3.3:

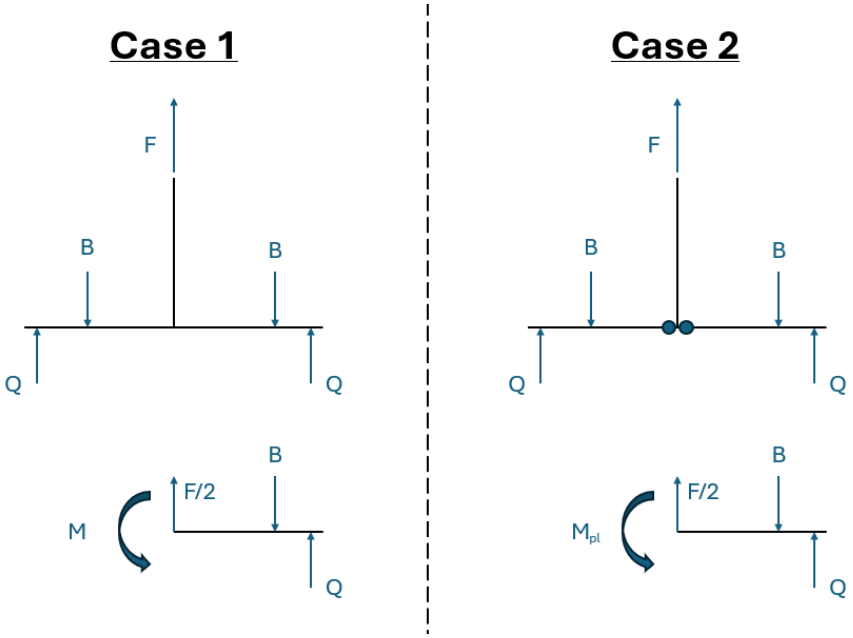

Figure 3.3: Illustration of cases 1 and 2

3.2 Resistance calculation of the T-stub

3.2.1 T-stub resistance under tension

The resistance of the T-stub under pure tension is calculated using the formulae provided in the Eurocode **prEN 1993-1-8** [9].

In this document, partial safety factors (e.g., γ_{M0}, etc.) are omitted, as the calculations are intended for verification purposes rather than for design. Consequently, these coefficients will not appear in the general formulae.

Verifications are performed using Method 1, although Method 2 (presented in Section 1.2) is often considered more accurate. However, in this case, the formation of a short or partial mechanism is not expected, and all effective lengths are determined according to Method 1. Therefore, applying Method 2 in conjunction with effective lengths derived from Method 1 would lead to inconsistent or incorrect results.

As outlined in the state of the art in Section 1.2, three distinct failure modes are identified for T-stub connections. The following expressions correspond to the "design resistance $F_{T,Rd}$ of an equivalent T-stub in tension" in the presence of prying forces [9].

Mode 1

The design resistance for Mode 1 is calculated for the situation without backing plates, using the following formula (method 1):

$$F_{T,1,Rd} = \frac{4 \cdot M_{pl,1,Rd}}{m} \tag{3.6}$$

where:

$$M_{pl,1,Rd} = 0.25 \cdot l_{eff,1} \cdot t_f^2 \cdot f_y \tag{3.7}$$

where $l_{eff,1}$ denotes the effective length associated with mode 1, as defined in Section 1.2. The other parameters are defined above and in Section 2.1.1, while $l_{eff,1}$ is calculated as follows:

$$l_{eff,1} = \min(l_{eff,cp};\ l_{eff,nc};\ l_{eff,W};\ L) \tag{3.8}$$

The letters "nc" refers to "non circular pattern", "cp" refers to "circular pattern" and "W" refers to "Warnant" formula.

The effective lengths for a column flange, as defined in the Eurocode and presented in Section 1.3, are calculated as follows:

$$l_{eff,cp} = 2 \cdot \pi \cdot m = 2 \cdot \pi \cdot 35 = 219.91 \text{ mm} \tag{3.9}$$

$$l_{eff,nc} = 4 \cdot m + 1.25 \cdot e = 4 \cdot 35 + 1.25 \cdot 30 = 177.5 \text{ mm} \tag{3.10}$$

where $m = 35\,mm$, $e = 30\,mm$, and L represents the length of the T-stub, previously defined as $L = 256\,mm$.

In addition to these lengths, the additional effective lengths $l_{eff,nc,W}$ and $l_{eff,c,W}$, introduced by Warnant in his work [6] and presented in Section 1.3, are also considered. Although not included in the Eurocode, these lengths are proposed due to their accuracy in isolated T-stub. The Equations 1.14 and 3.12, by substituting the known values are given by:

$$l_{eff,nc,W} = \frac{256 \cdot 35}{2(35+30)} + 35 \cdot \left(0.0876 \left(\frac{30}{35}\right)^3 - 0.6816 \left(\frac{30}{35}\right)^2 + 3.1143\frac{30}{35} + 0.9786\right)$$

$$l_{eff,nc,W} = 181 \text{ mm} \tag{3.11}$$

$$\ell_{eff,c,W} = \frac{2 \cdot 256 - 2 \cdot 35 + \pi \cdot 35}{2} = 275.98 \text{ mm} \tag{3.12}$$

The effective length $l_{eff,1}$ is determined as the minimum value among the four calculated effective lengths. Using the computed values, Equation 3.8 becomes:

$$l_{eff,1} = \min(219.91;\ 177.5;\ 181;\ 275.98) = 177.5 \text{ mm} \tag{3.13}$$

Calculation of the Plastic Moment and Design Resistance

Using the calculated effective length $l_{eff,1}$, the plastic moment is obtained as:

$$M_{pl,1,Rd} = 0.25 \cdot l_{eff,1} \cdot t_f^2 \cdot f_y \tag{3.14}$$

$$M_{pl,1,Rd} = 0.25 \cdot 177.5 \cdot 9^2 \cdot 392.2 = 1\,409\,713.9 \text{ N.mm} \tag{3.15}$$

Finally, for Mode 1, the design resistance in tension is calculated as:

$$F_{T,1,Rd} = \frac{4 \cdot 1\,409\,713.9}{35} = 161\,110.16 \text{ N} \tag{3.16}$$

Mode 2

The design resistance for Mode 2 is calculated using the following formula:

$$F_{T,2,Rd} = \frac{2M_{pl,2,Rd} + n \cdot B_{t,Rd}}{m + n} \tag{3.17}$$

where:

$$M_{pl,2,Rd} = 0.25 \cdot l_{eff,2} \cdot t_f^2 \cdot f_y \tag{3.18}$$

and:

$$l_{eff,2} = l_{eff,nc} = 177.5 \text{ mm} \tag{3.19}$$

Substituting the known values:

$$M_{pl,2,Rd} = 0.25 \cdot 177.5 \cdot 9^2 \cdot 392.2 = 1\,409\,713.9 \text{ N.mm} \tag{3.20}$$

Calculation of the bolt tension resistance $B_{t,Rd}$

The value of $B_{t,Rd}$ corresponds to the total tensile resistance of the bolts in the equivalent T-stub. It is calculated using the following formula:

$$B_{t,Rd} = n_b \cdot 0.9 \cdot f_{ub} \cdot A_s \tag{3.21}$$

where:
- $f_{ub} = 933.83$ MPa (ultimate tensile strength of the bolt),
- $A_s = 245.04\,\text{mm}^2$ (tensile stress area of the bolt),
- $n_b = 2$ (number of bolts)

The factor of 2 accounts for the presence of two bolts in the T-stub flange, as the basic expression for $B_{t,Rd}$ (excluding the number of bolts, n_b) corresponds to the resistance of a single bolt. It is assumed that the tensile and/or shear force applied to the T-stub is evenly distributed between the two bolts.

Performing the calculation:

$$B_{t,Rd} = 2 \cdot 0.9 \cdot 933.83 \cdot 245.04 = 411\,892.2 \text{ N} \tag{3.22}$$

Final Calculation of $F_{T,2,Rd}$

By substituting the values of $M_{pl,2,Rd}$ and $B_{t,Rd}$ into the initial expression, the design resistance of the T-stub under Mode 2 is:

$$F_{T,2,Rd} = \frac{2 \cdot 1\,409\,713.9 + 30 \cdot 411\,892.2}{35 + 30} = 233\,479.9 \text{ N} \tag{3.23}$$

Mode 3

The design resistance for Mode 3 corresponds to the tensile resistance of the bolts (Equation 3.22):

$$F_{T,3,Rd} = B_{t,Rd} = 411\,892.2 \text{ N} \tag{3.24}$$

T-stub in pure tension: Design resistance

The design resistance of the T-stub in pure tension is determined by the minimum value among the three calculated modes (for method 1):

$$F_{T,\text{resistance}} = \min\left(F_{T,1,Rd}; F_{T,2,Rd}; F_{T,3,Rd}\right) = F_{T,1,Rd} = 161\,110.16\,\text{N} \tag{3.25}$$

Failure occurs according to Mode 1, which corresponds to the formation of four plastic hinges in the T-stub.

By analyzing the calculated values and comparing them with the experimental results obtained during Mancini's tests for T-stub under pure tension [3], the following values are obtained:

Type of Value	Value	Unit
Mode 1	161 110.16	N
Mode 2	233 479.9	N
Mode 3	411 892.2	N
Mancini Yielding	174 240	N

Table 3.1: Design and experimental tension resistances for the T-stub

This comparison shows that the experimentally observed yielding resistance is approximately 8.15% higher than the design resistance corresponding to Mode 1 failure. This indicates that the Eurocode-based analytical approach provides a conservative estimation of the resistance of the T-stub under pure tension.

3.2.2 T-stub bearing resistance under shear load

According to the Eurocode [9], the design bearing resistance for individual fasteners in normal round holes, subject to shear and/or tension, must be verified for bolts. The general formula for bearing resistance is given by:

$$F_{b,Rd} = k_m \alpha_b \, f_u \, d \, t \tag{3.26}$$

where:
- k_m is a correction factor for steel grades (for steel grades up to S460: $k_m = 1$).
- α_b is a coefficient depending on the position of the fastener

For end fasteners:

$$\alpha_b = \min\left(\frac{e_1}{d_0}, 3\frac{f_{ub}}{f_u}, 3\right) \tag{3.27}$$

Given the following parameters:

- Edge distance: $e_1 = \dfrac{L - d_0}{2} = \dfrac{256 - 22}{2} = 117$ mm
- Hole diameter: $d_0 = 22$ mm
- Ultimate tensile strength of the bolt: $f_{ub} = 933.83\,\text{MPa}$
- Ultimate tensile strength of the plate: $f_u = 523.2$ MPa
- Bolt diameter: $d = 20$ mm
- Flange thickness: $t = 9$ mm

With all the above parameters, the value of α_b is determined as:

$$\alpha_b = \min\left(\frac{117}{22},\, 3 \cdot \frac{933.83}{523.2},\, 3\right) = \min\left(5.32,\, 5.35,\, 3\right) = 3 \tag{3.28}$$

Substituting these values into Equation (3.26):

$$F_{b,Rd} = 1 \cdot 3 \cdot 523.2 \cdot 20 \cdot 9 = 282\,528 \text{ N} \tag{3.29}$$

Bearing Resistance of the T-Stub

Since the T-stub includes two bolts and assumes an equal distribution of force between them, the total bearing resistance is calculated as follows:

$$F_{b,Rd,\text{T-stub}} = 2 \cdot F_{b,Rd} = 2 \cdot 282\,528 = 565\,056 \text{ N} \tag{3.30}$$

Thus, the bearing resistance of the T-stub under axial and shear load is 565 056N.

3.3 Bolt under combined efforts

3.3.1 Calculation of resistance for isolated bolts according to several standards

Extensive research on isolated bolts has been conducted through a large-scale program across various universities, where the work of Yunchen Song proves particularly useful in this study [17].

There are different methodologies for predicting the resistance of isolated bolts, including the Eurocode [9], the American standard (AISC 360) [18], the Australian standard (AS 4100)[19], and a new and improved formula proposed by Song [20]. The calculation of bolt resistance depends on whether the shear plane passes through the threads (noted as TT) or the unthreaded shank (noted as TS).

The following notations are used throughout the formulae:

- $B_{t,Rd}$: Bolt resistance in tension
- $B_{v,Rd}$: Bolt resistance in shear

a) Three design codes formulations

- Eurocode [9]:

$$\frac{B_{t,Ed}}{1.4 \cdot B_{t,Rd}} + \frac{B_{v,Ed}}{B_{v,Rd}} \leq 1 \tag{3.31}$$

Certain extreme limits are imposed to ensure physically acceptable values. For instance, if $B_{v,Ed} = 0$, a direct application of the formula would yield $B_{t,Ed} \leq 1.4 \cdot B_{t,Rd}$, which is not physically reasonable. To address this, an upper limit of $B_{t,Ed} = B_{t,Rd}$ is enforced. This constraint results in a bi-linear interaction in the graphical representation, as illustrated in Figure 3.4a.

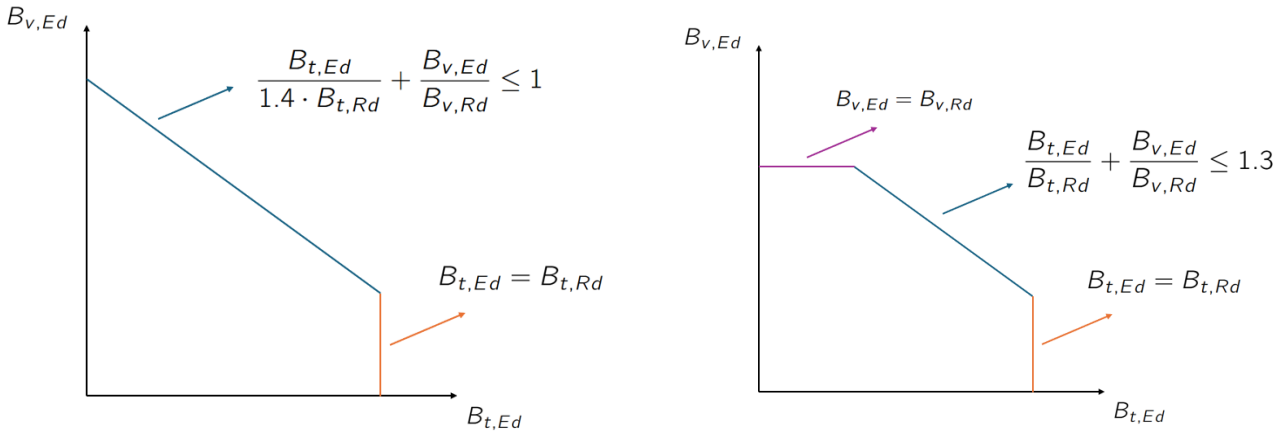

(a) Eurocode bi-linear curve

(b) Australian tri-linear curve

Figure 3.4: Illustration of Eurocode and American interaction curves with limiting criteria

- American Standard (AISC 360) [18]:

$$\frac{B_{t,Ed}}{B_{t,Rd}} + \frac{B_{v,Ed}}{B_{v,Rd}} \leq 1.3 \tag{3.32}$$

  Similarly to the Eurocode, the American standard imposes limits on extreme values. Specifically, two cases can arise: if $B_{t,Ed} = 0$, the interaction formula simplifies to $B_{v,Ed} \leq 1.3 \cdot B_{v,Rd}$. Conversely, if $B_{v,Ed} = 0$, it results in $B_{t,Ed} \leq 1.3 \cdot B_{t,Rd}$.
  Since these outcomes are not physically acceptable, an upper limit is imposed, setting the maximum values equal to the respective resistances in both shear and tension. This constraint leads to a tri-linear interaction in the graphical representation, as illustrated in Figure 3.4b.

- Australian Standard (AS 4100) [19] and Song's Formula [20]:

$$\left(\frac{B_{t,Ed}}{B_{t,Rd}}\right)^2 + \left(\frac{B_{v,Ed}}{B_{v,Rd}}\right)^2 \leq 1 \tag{3.33}$$

  While the mathematical formulations are similar for the AS 4100 standard and Song's formula, the key difference lies in the calculation of the parameter $B_{v,Rd}$.

b) Resistance formulations by design codes

The following table summarizes the specific expressions used to calculate the resistance in tension and shear for each standard. The first line under "Bolt in shear" column refers to the case where the shear plane passes through the threads (TT), while the second line corresponds to the case where the shear plane passes through the unthreaded shank (TS). And the values are calculated in the last two columns of the Table.

Design Code	Bolt in Tension $B_{t,Rd}$	Bolt in Shear $B_{v,Rd}$	$B_{t,Rd}$ [N]	$B_{v,Rd}$ [N]
EC3 1-8	$0.9f_{ub}A_s$	TT: $0.6f_{ub}A_s$ TS: $0.6f_{ub}A$	205 946.1	TT: 137 297.4 TS: 176 022.3
AISC 360	$0.75f_{ub}A$	TT: $0.5f_{ub}A$ TS: $0.625f_{ub}A$	220 027.9	TT: 146 685.25 TS: 183 356.6
AS 4100	$f_{ub}A_s$	TT: $0.62f_{ub}A_s$ TS: $0.62f_{ub}A$	228 829	TT: 141 873.9 TS: 181 889.7
Song	$f_{ub}A_s$	TT: $0.65f_{ub}A_s$ TS: $0.59f_{ub}A$	228 829	TT: 148 738.8 TS: 173 088.6

Table 3.2: Resistance formulations for isolated bolts according to different standards

Note: The definitions of A, A_s, and f_{ub} were provided at the beginning of Section 3, and their numerical values were calculated in Equations 3.1, 3.2 and 3.3.

For all verifications and calculations, the shear resistance of the bolts ($B_{v,Rd}$) is evaluated under the assumption that rupture and force transmission occur through the threaded portion. This approach yields conservative results compared to calculations based on the unthreaded shank.

Calculation of extreme values

The extreme interaction values of axial force and shear force on the bolts can be derived by fixing one force component to zero. Specifically:

- Setting $B_{t,Ed} = 0$ yields the maximum shear resistance.
- Setting $B_{v,Ed} = 0$ yields the maximum tension resistance.

By performing these calculations, the extreme axial and shear resistance values are obtained for each standard. These values are calculated (using formulae 3.31, 3.32 and 3.33) and are summarized in Table 3.3.

	$B_{t,Ed}$[N]	$B_{v,Ed}$[N]
EC3 1-8	0 205 946.1	137 297.4 0
AISC 360	0 220 027.88	146 685.25 0
AS 4100	0 228 829	141 873.98 0
Song	0 228 829	148 738.85 0

Table 3.3: Extreme axial and shear resistance values according to different standards

As previously explained, the interaction curves exhibit different shapes depending on the standard: bi-linear for the Eurocode, and tri-linear for the American standard (AISC 360). Using the previously calculated resistance values, the lengths of the interaction plateaus can be determined using the following equations:

- **Eurocode:** $B_{t,Ed} = B_{t,Rd}$

$$B_{v,Ed} = B_{v,Rd} \cdot \left(1 - \frac{B_{t,Ed}}{1.4 \cdot B_{t,Rd}}\right) = 137\,297.4 \cdot \left(1 - \frac{205\,946.1}{1.4 \cdot 205\,946.1}\right) = 39\,227.83\,\text{N} \quad (3.34)$$

- **American Standard (AISC 360):**
  If the value of $B_{t,Ed}$ is fixed and equal to upper bound $B_{t,Rd}$:

$$B_{v,Ed} = B_{v,Rd} \cdot \left(1.3 - \frac{B_{t,Ed}}{B_{t,Rd}}\right) = 146\,685.25 \cdot \left(1.3 - \frac{220\,027,88}{220\,027,88}\right) = 44\,005.58\,\text{N} \quad (3.35)$$

  If the value of $B_{v,Ed}$ is fixed and equal to upper bound $B_{v,Rd}$:

$$B_{t,Ed} = B_{t,Rd} \cdot \left(1.3 - \frac{B_{v,Ed}}{B_{v,Rd}}\right) = 220\,027,88 \cdot \left(1.3 - \frac{146\,685.25}{146\,685.25}\right) = 66008.36\,\text{N} \quad (3.36)$$

Calculation of intermediate values

To generate the interaction curves, a fixed tensile load ($B_{t,Rd}$) was selected, and the corresponding shear resistance ($B_{v,Rd}$) was calculated for each standard.

The following section illustrates the calculation procedures for the different design standards based on a given value of $B_{t,Ed}$. The derived formulae are as follows:

- **Eurocode:**

$$\frac{B_{t,Ed}}{1.4 \cdot B_{t,Rd}} + \frac{B_{v,Ed}}{B_{v,Rd}} \leq 1 \quad \Rightarrow \quad B_{v,Ed} \leq B_{v,Rd}\left(1 - \frac{B_{t,Ed}}{1.4 \cdot B_{t,Rd}}\right) \quad (3.37)$$

- **American Standard (AISC 360):**

$$\frac{B_{t,Ed}}{B_{t,Rd}} + \frac{B_{v,Ed}}{B_{v,Rd}} \leq 1.3 \quad \Rightarrow \quad B_{v,Ed} \leq B_{v,Rd}\left(1.3 - \frac{B_{t,Ed}}{B_{t,Rd}}\right) \quad (3.38)$$

- **Australian Standard (AS 4100) and Song's Formula:**

$$\left(\frac{B_{t,Ed}}{B_{t,Rd}}\right)^2 + \left(\frac{B_{v,Ed}}{B_{v,Rd}}\right)^2 \leq 1 \quad \Rightarrow \quad B_{v,Ed} \leq B_{v,Rd} \cdot \sqrt{1 - \left(\frac{B_{t,Ed}}{B_{t,Rd}}\right)^2} \quad (3.39)$$

To illustrate the application of these formulae, the calculated values are presented for a selected axial load of $B_{t,Ed} = 100\,000$ N.

The corresponding shear resistances predicted by the different standards are as follows:

- **Eurocode:**

$$B_{v,Ed} = 137\,297.4\left(1 - \frac{100\,000}{1.4 \cdot 205\,946.1}\right) = 89\,678.3\text{N} \quad (3.40)$$

- **American Standard (AISC 360):**

$$B_{v,Ed} = 146\,685.25\left(1.3 - \frac{100\,000}{220\,027.9}\right) = 124\,024.2\text{N} \quad (3.41)$$

- **Australian Standard (AS 4100):**

$$B_{v,Ed} = 141\,873.9 \cdot \sqrt{1 - \left(\frac{100\,000}{228\,829}\right)^2} = 127\,609.6\text{N} \quad (3.42)$$

- **Song's Formula:**

$$B_{v,Ed} = 148\,738.8 \cdot \sqrt{1 - \left(\frac{100\,000}{228\,829}\right)^2} = 133\,784.3\text{N} \quad (3.43)$$

3.3.2 Results: bolts under combined efforts

The following graph presents the calculated resistance of the individual bolts according to the different design standards.

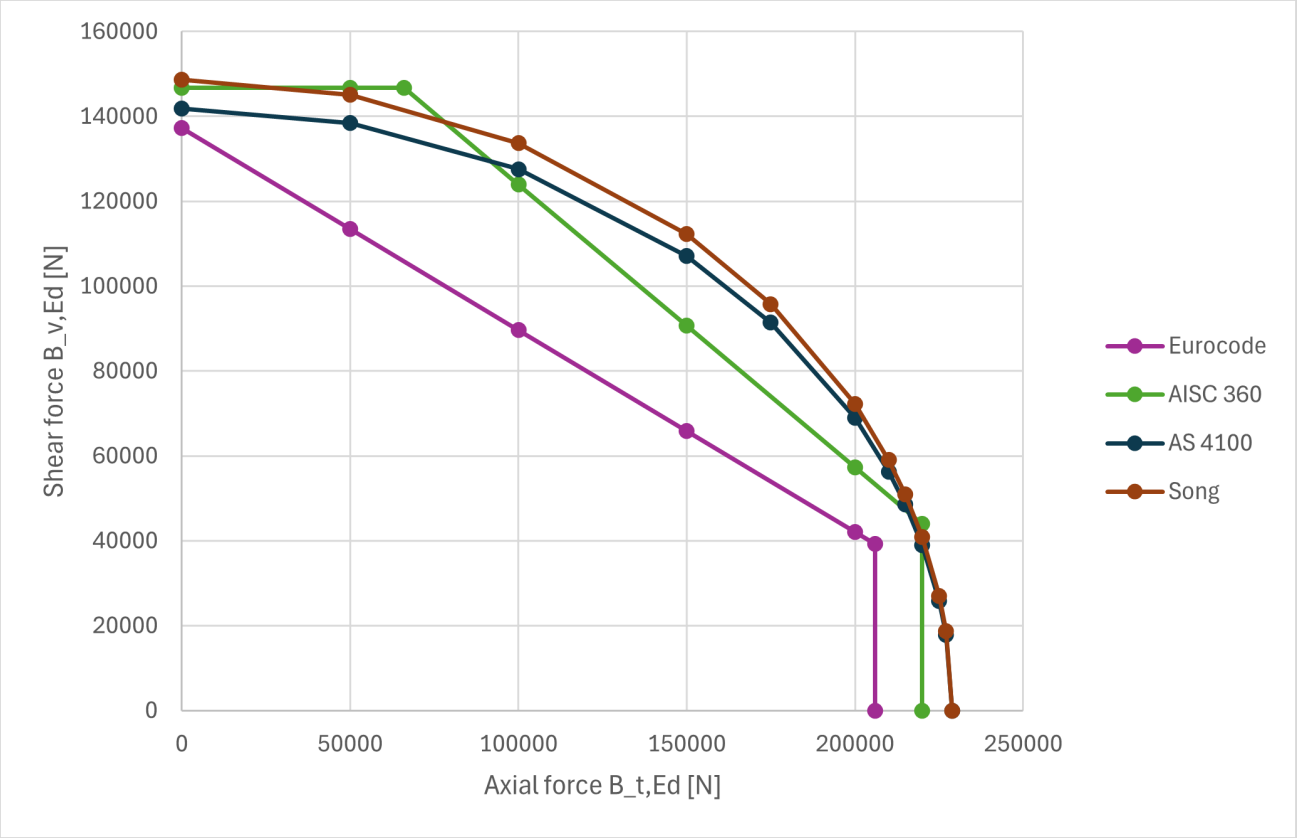

Figure 3.5: Interaction diagram for bolt resistance under combined axial and shear forces

From the Figure 3.5, it can be observed that the Eurocode and American standards provide more conservative (i.e., safer) estimates compared to the other methodologies. The imposed limits for both the Eurocode and the American standard are clearly visible, as previously discussed. Specifically, the Eurocode exhibits a bi-linear interaction curve, while the American standard presents a tri-linear interaction. .

3.4 Calculations: Case 1 and Case 2

The method used to calculate the forces applied to the T-stub model, as illustrated in Figure 3.2, depends on the magnitude of the applied tensile force F.

The calculations needed to obtain the value of the force making the transition between these two cases will be detailed in Section 3.5.

3.4.1 Case 1: No formation of a plastic hinge ($M < M_{pl,1,Rd}$)

The situation illustrated on the left of Figure 3.3 applies.

The equilibrium conditions are based on Jaspart's formula [2](for compatibility of displacements at the bolt position) 3.46, vertical equilibrium 3.44 and moment equilibrium 3.45:

$$F + 2Q = 2B_t \tag{3.44}$$

$$\frac{F}{2} \cdot (m+n) = n \cdot B_t + M \tag{3.45}$$

$$F = B_t \cdot q \tag{3.46}$$

The geometrical parameters m and n are known, and the applied tensile force F is fixed. To verify whether the condition $M < M_{pl,1,Rd}$ is satisfied, the moment M is computed using Equation (3.45).

The parameter q is determined using Jaspart's formulation for preloaded bolts. The bolts are initially preloaded up to 125 kN, and this preloading is explicitly considered in the subsequent calculations [2]:

$$q = \frac{Z_e a_{e1} + Z_{cf}\alpha_{cf1}}{Z_e \alpha_{e2} + Z_{cf}\alpha_{cf2} + \frac{k_2 k_3^*}{2A_s(k_2+k_3^*)}} \tag{3.47}$$

The terms in the equation correspond to dimensions illustrated in Figures 3.6 and 3.7.

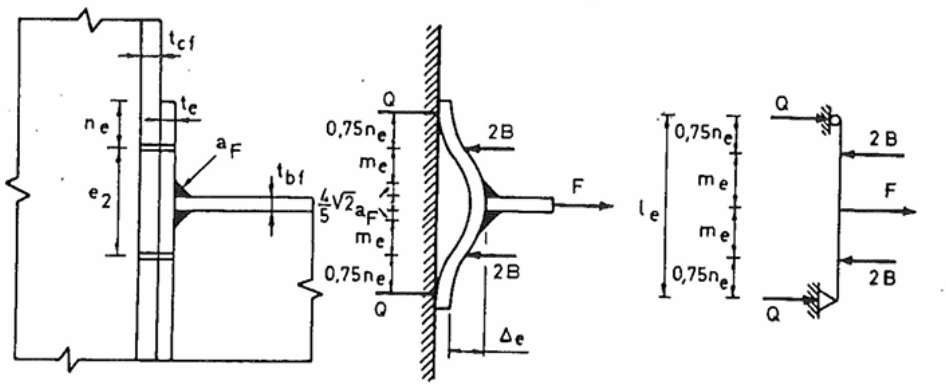

Figure 3.6: End plate geometry (Jaspart model [2])

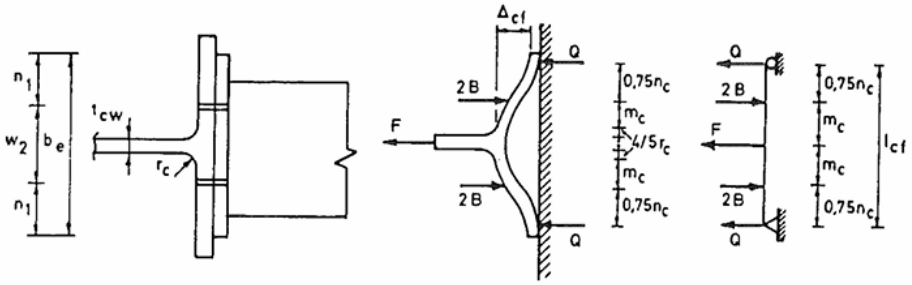

Figure 3.7: Column flange geometry (Jaspart model [2])

The geometric parameters are defined as follows:

$$Z_e = \frac{\ell_e^3}{w_e t_e^3} \qquad Z_{cf} = \frac{\ell_{cf}^3}{w_{cf} t_{cf}^3}$$
$$\alpha_{e1} = 1.5\alpha_e - 2\alpha_e^3 \qquad \alpha_{cf1} = 1.5\alpha_{cf} - 2\alpha_{cf}^3$$
$$\alpha_{e2} = 6\alpha_e^2 - 8\alpha_e^3 \qquad \alpha_{cf2} = 6\alpha_{cf}^2 - 8\alpha_{cf}^3$$
$$\ell_e = 2(m_e + 0.75n_e) \qquad \ell_{cf} = 2(m_e + 0.75n_l)$$
$$2w_e = b_e \qquad 2w_{cf} = e_2 + 1.5n_e$$
$$\alpha_e = \frac{0.75n_e}{\ell_e} \qquad \alpha_{cf} = \frac{0.75n_l}{\ell_{cf}}$$

The parameters k_1, k_2, k_3^* and k_4 are computed as:

$$k_1 = \ell_s + 1.43\ell_t + 0.71\ell_n, \quad k_2 = \ell_s + 1.43\ell_t + 0.91\ell_n + 0.4\ell_w, \quad k_3^* = \frac{t_e + t_{cf}}{5}, \quad k_4 = 0.1\ell_n + 0.2\ell_w \tag{3.48}$$

Given that the T-stub is in contact with a rigid foundation, calculations on the column flange are omitted. This simplifies the expression for q to:

$$q = \frac{Z_e a_{e1}}{Z_e \alpha_{e2} + \frac{k_2 k_3^*}{2A_s(k_2 + k_3^*)}} \tag{3.49}$$

Using the provided dimensions:

$$\ell_e = 145\ mm, \quad w_e = 128\ mm, \quad t_e = 9\ mm, \quad t_{cf} = 28\ mm, \quad m_e = 50\ mm,$$
$$n_e = 30\ mm, \quad b_e = 256\ mm, \quad n_1 = 30\ mm, \quad e_2 = 100\ mm, \quad A_S = 245.04\ mm^2,$$

Bolt dimensions are illustrated in Figure 3.8 as follows:

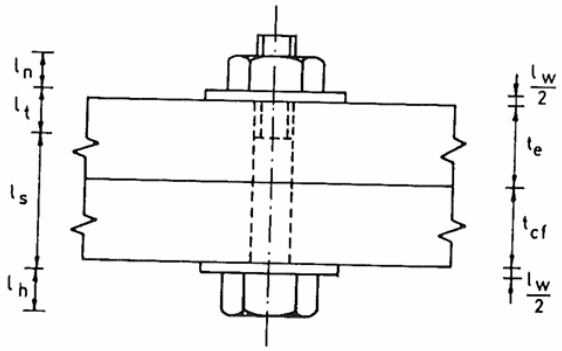

Figure 3.8: Bolt dimensions (Jaspart model [2])

$$\ell_s = 38\ mm, \quad \ell_t = 7\ mm, \quad \ell_n = 18\ mm, \quad \ell_w = 8\ mm$$

Note: some dimensions are found thanks to FATOR catalog [15].

After calculating the necessary parameters:

$$Z_e = 32.671, \quad \alpha_{e1} = 0.225, \quad \alpha_{e2} = 0.11458, \quad k_2 = 67.59, \quad k_3^* = 7.4, \quad k_4 = 3.4$$

The resulting value of q is:

$$q = \frac{32.671 \cdot 0.225}{32.671 \cdot 0.11458 + \frac{67.59 \cdot 7.4}{2 \cdot 245.04 \cdot (67.59+7.4)}} = 1.959 \tag{3.50}$$

Using these values, the forces B_t, Q, and the moment M can be computed:

$$B_t = \frac{F}{q}, \quad Q = \frac{2B_t - F}{2}, \quad M = \frac{F}{2} \cdot (m+n) - n \cdot B_t \tag{3.51}$$

3.4.2 Case 2: Formation of plastic hinge ($M > M_{pl,1,Rd}$)

In this case, the formation of plastic hinges at the connection between the web and both sides of the flange reduces the number of equilibrium conditions to be considered. The scheme of the situation is illustrated on the right of the Figure 3.3, with small blue circles representing the two plastic hinges. Only the vertical equilibrium and the moment equilibrium equations are required.

The moment is known as it reaches the plastic capacity, meaning $M = M_{pl,1,Rd}$. By applying a known value of F, the following calculations can be performed based on the equations (3.44) and (3.45) :

$$B_t = \left(\frac{F}{2} \cdot (m+n) - M_{pl,1,Rd} \right) / n, \qquad Q = \frac{2 \cdot B_t - F}{2} \tag{3.52}$$

3.5 Calculation of resistance

Two different approaches can be used to evaluate the resistance of the model. The first involves applying a force to the T-stub and subsequently calculating the forces induced in the bolts. The second approach consists in determining the required force to be applied to the T-stub, based on the known forces acting on the bolts.

These two approaches offer distinct methods for calculating and representing the resistance of the system. One represents the resistance of the T-stub, while the other represents the resistance of the bolts.

3.5.1 Bolt under combined efforts

Calculation of the force transmitted from the T-stub to the bolts

The forces applied to the T-stub under experimental conditions are provided in the results of Mancini's tests [3]. These values are given for both the yielding and collapse states. The angle of inclination represents the orientation of the applied tensile force relative to the T-stub:

- An angle of 0° corresponds to pure shear loading.
- An angle of 90° corresponds to pure tensile loading.

In accordance with its assumptions, the Eurocode neglects the influence of flexural forces acting on the bolt.

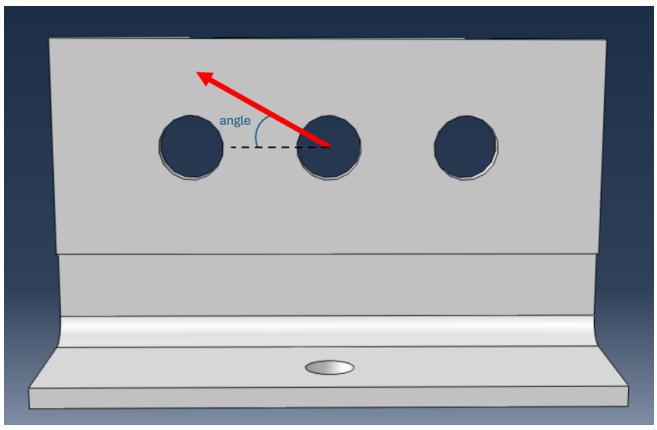

Figure 3.9: Illustration of the applied force on the plate

The measured values for the yield condition of the T-stub are presented in Table 3.4 (and extracted from the graph illustrated in Appendix A1):

Angle of inclination	Axial force [N]	Shear force [N]
0°	0	352 422.5
30°	156 740	271 210
45°	176 380	176 365
60°	176 490	102 220
75°	183 440	49 700
90°	174 240	0

Table 3.4: **YIELD** results of Mancini [3]

Similarly, the values corresponding to the collapse condition of the T-stub are shown in Table 3.5:

Angle of inclination	Axial force [N]	Shear force [N]
0°	0	352 550
15°	86 550	323 010
30°	164 600	285 100
45°	223 500	223 500
60°	272 310	157 220
75°	294 610	78 940
90°	285 728	0

Table 3.5: **COLLAPSE** results of Mancini [3]

Calculation of forces induced on the bolt

Before proceeding with the calculations, it is necessary to determine whether the system corresponds to Case 1 or Case 2, as defined in Section 3.1.3. This distinction depends on the force applied to the T-stub and the resulting internal forces in the bolts.

To identify the transition point between the two behaviours (Case 1 or Case 2), the plastic moment resistance $M_{pl,1,Rd}$ must be considered. This value, calculated in Equation 1.8, is given as:

$$M_{pl,1,Rd} = 1\,409\,713.9\,\text{N.mm} \tag{3.53}$$

By substituting the expression for the bolt force B_t from Equation 3.46 into the moment equilibrium Equation 3.45, the following equation is obtained:

$$\frac{B_t \cdot q}{2} \cdot (m+n) = n \cdot B_t + M \tag{3.54}$$

Isolating B_t yields:

$$B_t = \frac{2 \cdot 1\,409\,713.9}{(1.959 \cdot 35 + 1.959 \cdot n - 2 \cdot 30)} = 41\,869.17\,\text{N} \tag{3.55}$$

Substituting this value into Equation 3.46 provides the corresponding applied force:

$$F = B_t \cdot q = 41\,869.17 \cdot 1.959 = 82\,024.27\,\text{N} \tag{3.56}$$

Therefore, the transition between Case 1 and Case 2 occurs at approximately 82 024 N. Specifically:

- **Case 1:** If $F < 82\,024\,\text{N}$, no plastic hinge is formed.
- **Case 2:** If $F \geq 82\,024\,\text{N}$, plastic hinges develop.

Using the derived formulae in equation 3.51, it is now possible to calculate the forces acting on the bolts under the specified experimental conditions. These calculated forces can be directly compared with the predictions provided by various standards for the resistance of bolts under combined axial and shear loading.

Example: Calculation of bolt forces from applied T-stub loads

As an illustrative example, the following section details the calculation of the forces experienced by the bolts when specific loads are applied to the T-stub. The calculation is performed for the following yielding values, corresponding to an inclination angle of 60°, as extracted from Table 3.4:

$$F = 176\,490\,\text{N} \qquad \text{and} \qquad V = 102\,220\,\text{N} \tag{3.57}$$

The first step is to identify whether the system corresponds to Case 1 or Case 2. This requires calculating the bending moment M and comparing it to the plastic moment resistance $M_{pl,1,Rd}$. The tensile force $B_{t,Ed}$ acting on the bolt is calculated using Equation 3.51, from which the moment M is subsequently derived:

$$B_{t,Ed} = \frac{F}{q} = \frac{176\,490}{1.959} = 90\,089.056\,\text{N} \tag{3.58}$$

$$M = \frac{F}{2} \cdot (m+n) - n \cdot B_{t,Ed} = \frac{176\,490}{2} \cdot (35+30) - 30 \cdot 90\,089.056 = 3\,033\,253.31\,\text{N.mm} \tag{3.59}$$

The computed moment exceeds the plastic moment resistance, as calculated in Equation 3.15:

$$M = 3\,033\,253.31\,\text{N.mm} > M_{pl,1,Rd} = 1\,409\,713.88\,\text{N.mm}$$

This indicates the formation of a plastic hinge, corresponding to Case 2, in which the bending moment is limited to $M = M_{pl,1,Rd}$.

Using this adjusted moment, the updated value of the tensile force $B_{t,Ed}$ is calculated by rearranging the expression in Equation 3.51:

$$B_{t,Ed} = \left(\frac{176\,490}{2} \cdot (35+30) - 1\,409\,713.88 \right) / 30 = 144\,207.04\,\text{N} \tag{3.60}$$

The corresponding prying force Q is then obtained as follows:

$$Q = \frac{2 \cdot 144\,207.04 - 176\,490}{2} = 55\,962.04\,\text{N} \tag{3.61}$$

The shear force acting on a single bolt is assumed to be half the total shear force applied to the T-stub, based on the assumption of symmetric load distribution.

The final calculated forces acting on a single bolt are:

$$B_{t,Ed} = 144\,207.04\,\text{N} \quad \text{and} \quad B_{v,Ed} = \frac{V}{2} = 51\,110\,\text{N} \tag{3.62}$$

Based on these calculations and using Mancini's results for yield and collapse resistances (refer to Tables 3.4 and 3.5), the forces supported by the bolts can be accurately represented. These results are illustrated in Figure 3.10.

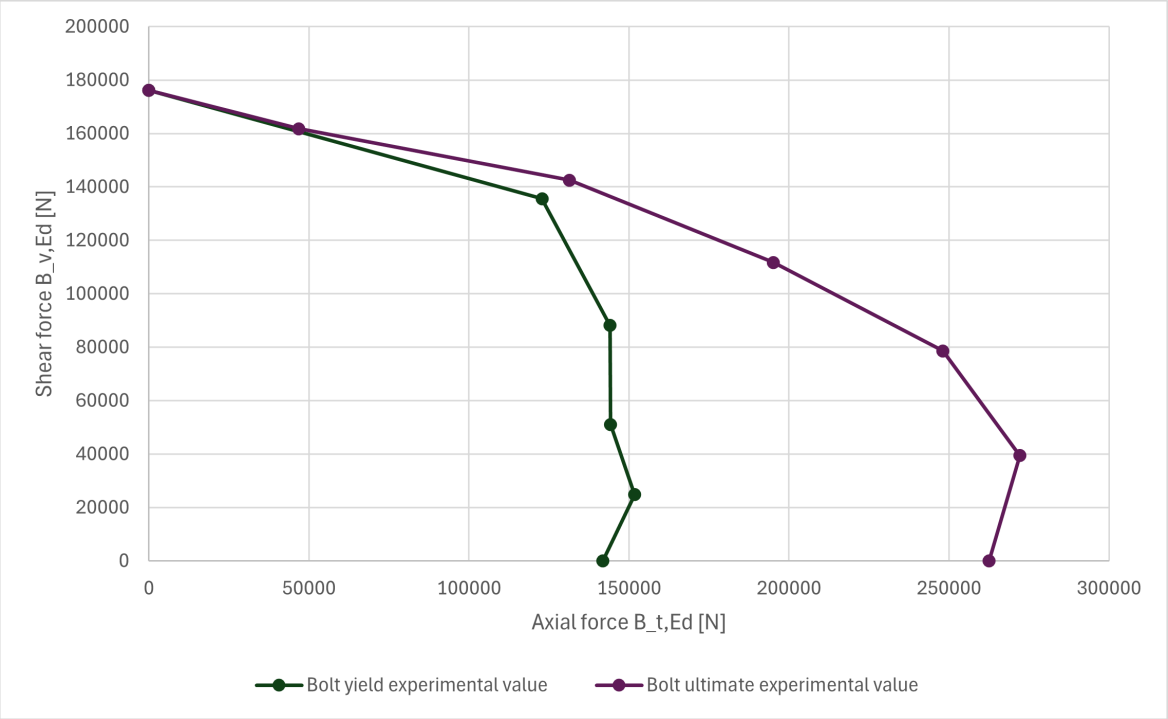

Figure 3.10: Bolt resistance from Mancini's measured values [3]

3.5.2 T-stub under combined efforts

All the previous calculations can be performed by assuming forces applied on the T-stub and then deducing the corresponding forces on the bolts. This allows for a graphical representation of the bolt resistance under combined loading conditions.

The problem can also be approached inversely by assuming forces on the bolts and calculating the corresponding forces required on the T-stub to generate them. Two distinct cases must still be considered: with and without the formation of plastic hinges. The transition between these cases occurs when the value of $B_{t_{Ed}}$ is approximately 41 869.17 N, as calculated in Equation 3.55.

Specifically:

- If $B_{t,Ed} < 41\,869.17\,\text{N}$, no plastic hinges are formed.
- If $B_{t,Ed} \geq 41\,869.17\,\text{N}$, plastic hinges are formed.

The same formulae previously derived are applicable:

- **Without plastic hinge formation:** Refer to Equations (3.44), (3.45) and (3.46)

- **With plastic hinge formation:** Refer to Equation (3.52).

A specific set of forces applied to the bolts is now assumed in order to determine the corresponding forces required on the T-stub to reproduce these internal actions.

Example for given forces
Given the following values for the bolt forces:

$$B_{t,Ed} = 100\,000\,\text{N} \quad \text{and} \quad B_{v,Ed} = 89\,678.35\,\text{N}$$

These force values are calculated using Eurocode formulas, assuming an applied axial force of 100 000 N in the bolt. The corresponding shear force in the bolt is determined using Equation 3.37.

The force F can be determined using Equation 3.51, followed by the calculation of the bending moment M. This moment is then compared to the plastic moment capacity to assess the presence of a plastic hinge.

$$F = q \cdot B_{t,Ed} = 1.955 \cdot 100\,000 = 195\,503.63\,\text{N} \tag{3.63}$$

$$M = \frac{F}{2} \cdot (m+n) - n \cdot B_{t,Ed} = \frac{195\,503.63}{2} \cdot (35+30) - 30 \cdot 100\,000 = 3\,353\,867.975\,\text{N.mm} \tag{3.64}$$

The resulting moment exceeds the plastic moment resistance, indicating the formation of a plastic hinge :

$$M_{pl,1,Rd} = 1\,409\,713.88\,\text{N.mm} \leq M$$

This corresponds to Case 2, where $M = M_{pl,1,Rd}$. Using this condition, F is recalculated using formula 3.52:

$$F = (n \cdot B_{t,Ed} + M) \cdot \frac{2}{m+n} = (30 \cdot 100\,000 + 1\,409\,713.88) \cdot \frac{2}{35+30} = 135\,683.5\,\text{N} \tag{3.65}$$

The prying force Q is then obtained as follows:

$$Q = \frac{2 \cdot B_{t,Ed} - F}{2} = \frac{2 \cdot 100\,000 - 135\,683.5}{2} = 32\,158.25\,\text{N} \tag{3.66}$$

The shear force acting on the T-stub is assumed to be twice the shear force sustained by a single bolt, based on the hypothesis of equal load distribution between bolts.

The final values calculated for the T-stub are the following:

$$F = 135\,683.5\,\text{N} \quad \text{and} \quad V = 179\,356.7\,\text{N} \tag{3.67}$$

The results of the second approach can now be illustrated. This method consists in determining the required forces to be applied to the T-stub, based on known axial and shear forces acting on the bolts. The resulting limit values reflect the T-stub resistance when constrained by the bolt resistance values defined in the different design standards.

These results are represented in the following graph.

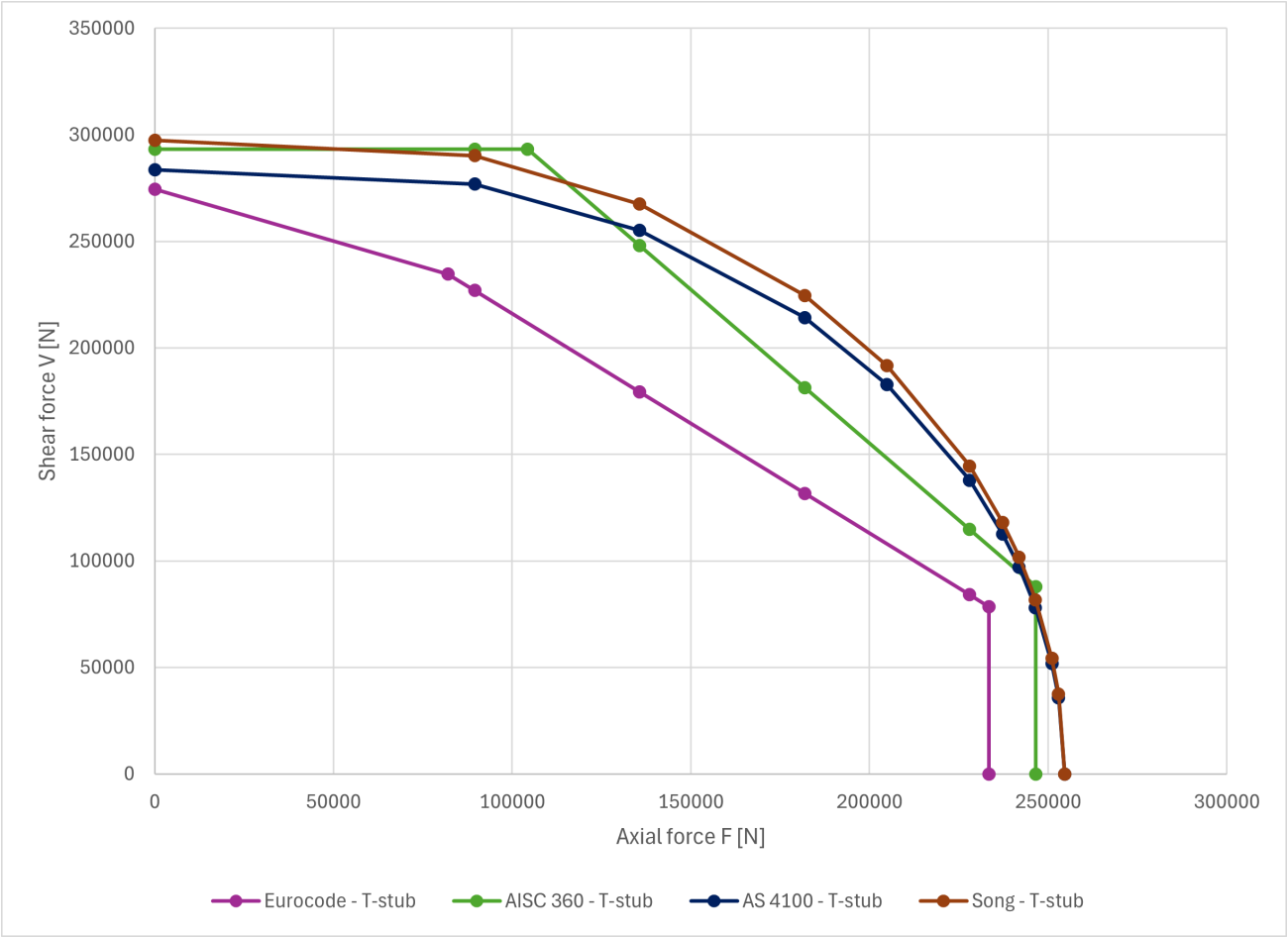

Figure 3.11: Interaction diagram for T-stub resistance under combined axial and shear forces

The change in slope of the Eurocode curve is due to the transition from Case 1 to Case 2 as the tensile force increases. As exposed in a previous section, the transition between the two cases appears at an applied force of 81 024 N. The others standards, as the Australian one, does not present a slope change because of the limitation of the extreme values, as explained in Equation 3.32 and illustrated in Figure 3.4b

3.5.3 T-stub final graph

The final graph illustrates the resistance of the T-stub under combined axial and shear loading. The bearing resistance, representing the shear resistance of the plate, is also shown. The red point indicates the Mode 1 failure, corresponding to the axial force limit associated with this failure mechanism. Additionally, all resistance curves of the T-stub, constrained by the bolt resistance limits specified in the various design standards, are represented.

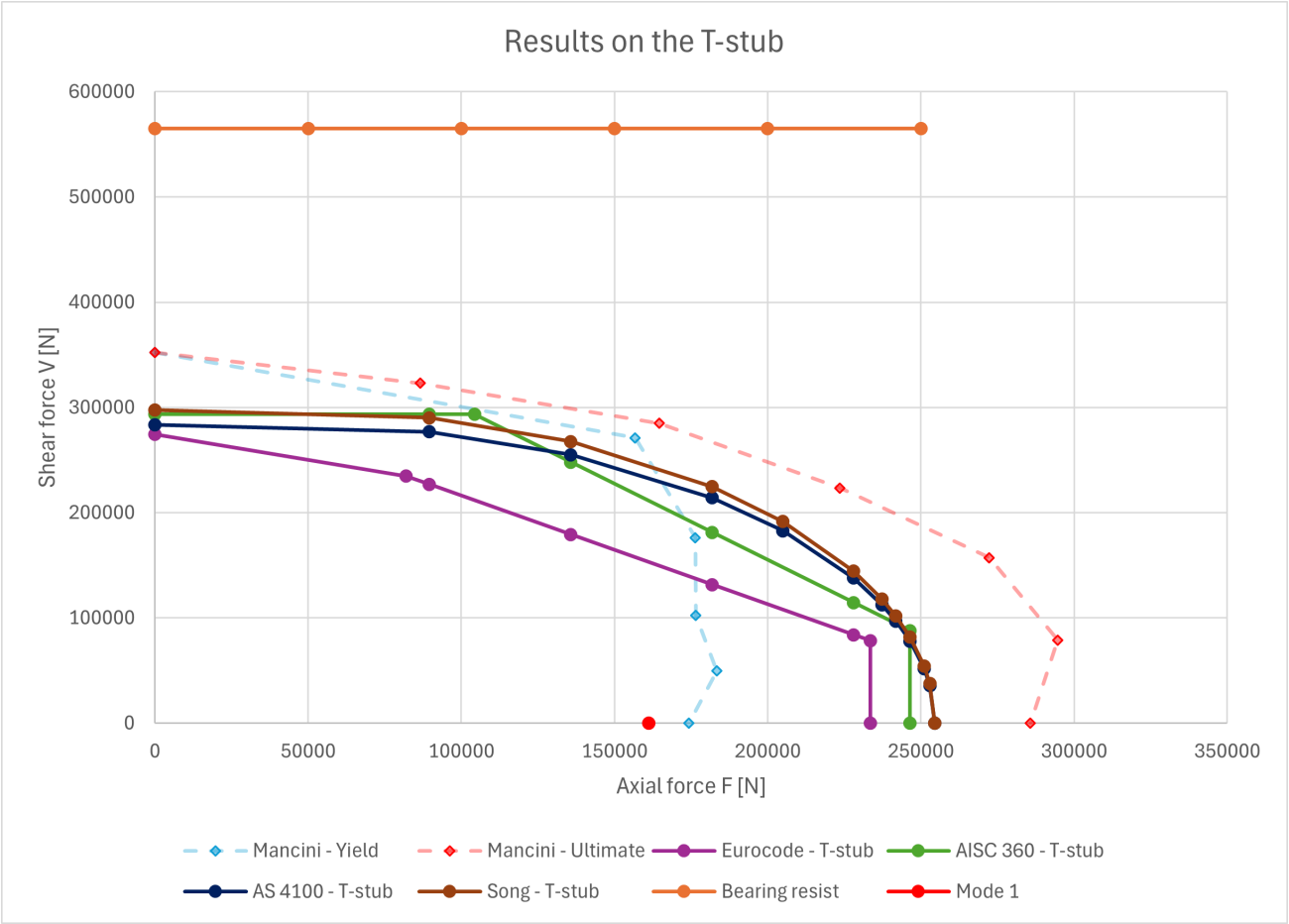

Figure 3.12: Complete interaction diagram for T-stub resistance under combined axial and shear forces

3.5.4 General observations on T-stub resistance

The curves exhibit a non-linear relationship, where an increase in axial force corresponds to a reduction in shear resistance. This behaviour is consistent with the expected response of a bolted connection subjected to combined loading conditions.

Comparison of Yield and Ultimate resistance (Figure 3.10)

- The **Mancini-Yield** curve represents the onset of yielding in the T-stub. It demonstrates a higher shear capacity at low axial forces, indicating that the connection initially provides significant shear resistance before plastic deformation begins.
- The **Mancini-Ultimate** curve characterizes the ultimate failure load, reaching higher axial forces before rupture. This highlights the plastic deformation reserve beyond the yield limit, which contributes to the overall ductility of the connection.

Comparison between design standards for bolts (Figure 3.5)

The comparison between different standards reveals significant variations in predicted capacities:

- The **Eurocode** results exhibit a conservative approach for high axial loads while maintaining substantial shear resistance at lower axial forces.
- The **AISC 360** standard provides less restrictive interaction limits between axial and shear forces, compared to Eurocode. However, its predictions closely align with the **AS 4100** and **Song** models in extreme cases of pure shear or pure axial loading.

- The **Song model** predicts the highest resistance values, indicating a less conservative approach compared to standardized design codes.

A transition in behaviour occurs when plastic hinges develop. This transition influences the overall load-bearing capacity, as the formation of plastic hinges enables force redistribution within the T-stub before failure occurs.

These findings emphasize the necessity of considering both yielding and plastic collapse mechanisms when designing bolted T-stub connections subjected to combined axial and shear loading.

3.5.5 Analysis of the results

The Eurocode and American standards adopt a more conservative approach, ensuring higher safety margins. In contrast, the Australian standard and the Song model provide less restrictive interaction curves, offering a more optimized representation of resistance.

A key observation is that the bearing resistance significantly exceeds the ultimate resistance of the T-stub. This confirms that failure due to insufficient bearing capacity is not a governing mode. Additionally, the resistance associated with **failure mode 3** under pure tension, with a value of 411 892.2 N as calculated in Equation 3.24, is considerably higher than the collapse resistance measured in Mancini's experiments. This indicates that **failure mode 3 is unlikely to occur**.

On the other hand, **failure mode 1** exhibits yield values close to those predicted by the Mancini's tests.

It is also noteworthy that plastic deformation significantly enhances the resistance, particularly for high axial loading scenarios. This increase in capacity is likely attributed to the contribution of the plate rather than the bolts themselves.

Furthermore, the resistance values provided by the standards are consistently more conservative than the experimental results reported by Mancini for collapse. This discrepancy highlights the limitations of current predictive models in accurately capturing the resistance of T-stubs under combined axial and shear loading.

Chapter 4

Numerical modelling

In this thesis, the use of the Finite Element (FE) analysis was chosen due to its ability to provide a comprehensive evaluation of structural behaviour under complex loading conditions. The nonlinear finite element software adopted to model the column T-stub specimen is Abaqus [21]. The modelling process follows a structured methodology, involving the definition of geometry, boundary conditions, material constitutive laws, mesh characteristics, applied loads and constraints.

The first modelling assumption is the introduction of a symmetry plane along the mid-plane of the T-stub web (see Figure 4.1). This assumption is justified by the specific loading conditions and is adopted to reduce the complexity of the model and enhance computational efficiency.

It is important to note that Abaqus allows for user-defined unit systems. In this study, the consistency is maintained by adopting tons [T] for mass, seconds [s] for time, and millimeters [mm] for length. Accordingly, force and stress are respectively expressed in Newtons [N] and Megapascals [MPa].

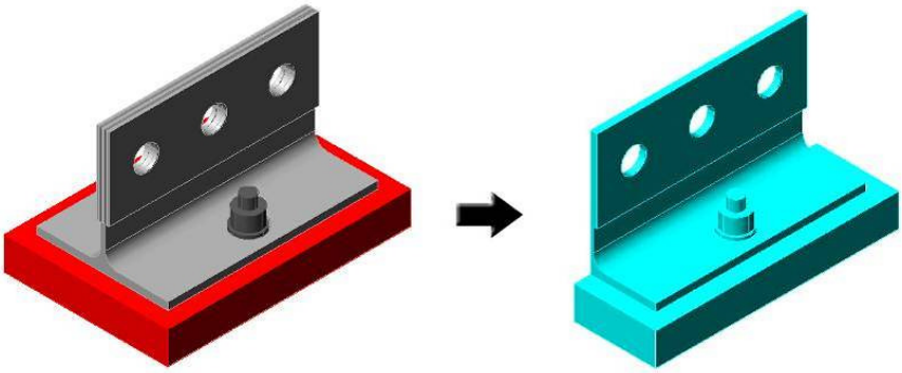

Figure 4.1: Symmetry simplification applied to the finite element model [3]

4.1 Modelling of the column T-Stub

4.1.1 Parts of the model

The T-stub assembly is composed of three primary parts. The dimensions used for each component are based on the average experimental values of specimens reported by Mancini [3].

- **T-stub**
  The T-stub, comprising the flange, web and welded plates, is modelled as a single solid part. The geometric profile corresponds to a HEA 160 section, as described in Section 2.1.1. A 2D representation of the dimensions is shown in Figure 4.2a, while the 3D extruded model – featuring the bolt

and pin holes – is illustrated in Figure 4.2b. The cell partition, already visible in the 3D figure, will be discussed in the subsequent section 4.1.3 about meshing.

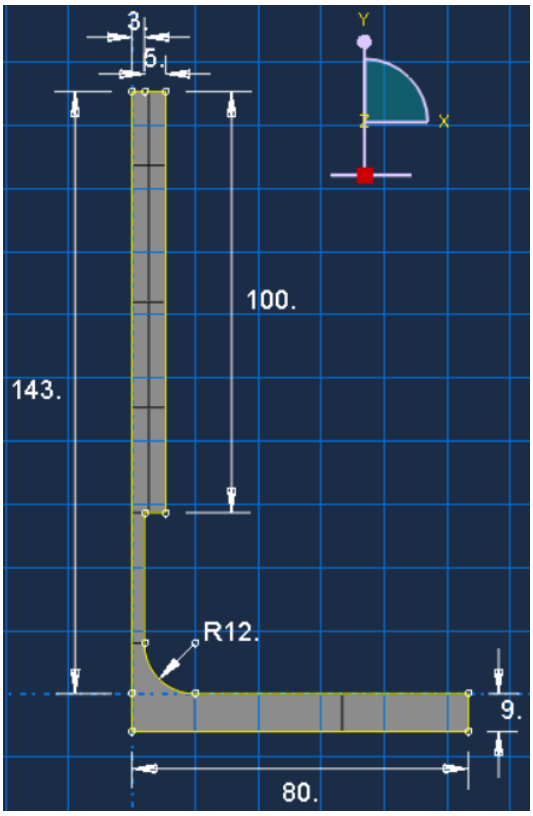

(a) T-stub dimensions in 2D (all dimensions in mm)

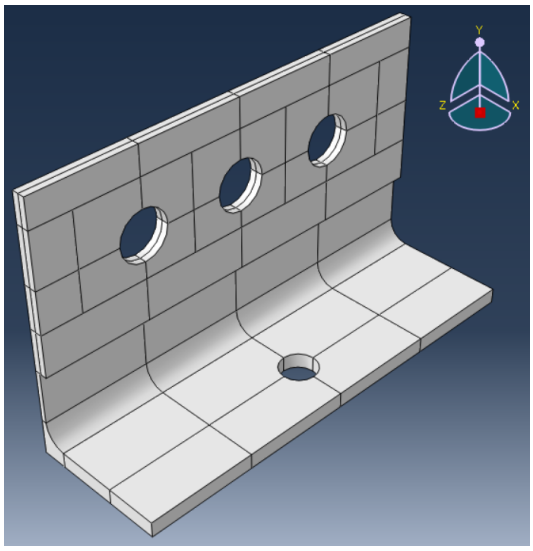

(b) 3D illustration of T-stub

Figure 4.2: Illustration of the T-stub part

Note: The extrusion depth is 256 mm.

The positions of the bolt and pin holes are shown in Figure 4.3.

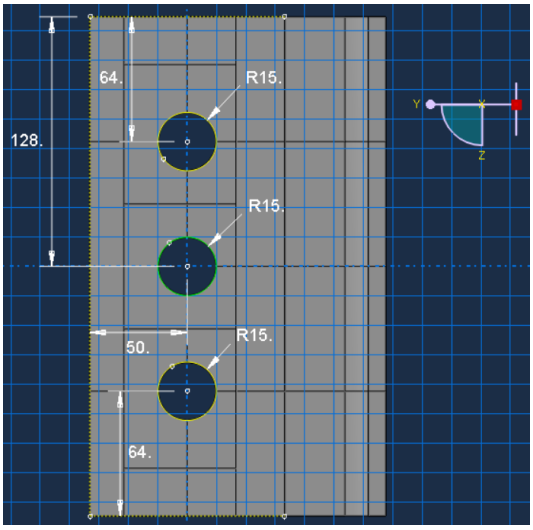

(a) Pin holes layout

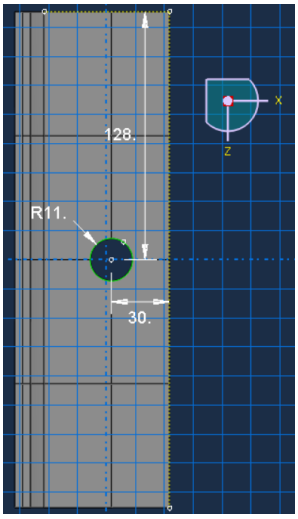

(b) Bolt hole layout

Figure 4.3: Positions of the bolt and pin holes (grid spacing: 15 mm; all dimensions in mm)

- **Foundation**
  The foundation represents the rigid support with a thickness of 28 mm and including a central hole of 22 mm in diameter. The 2D and 3D views of the foundation are shown in Figure 4.4.

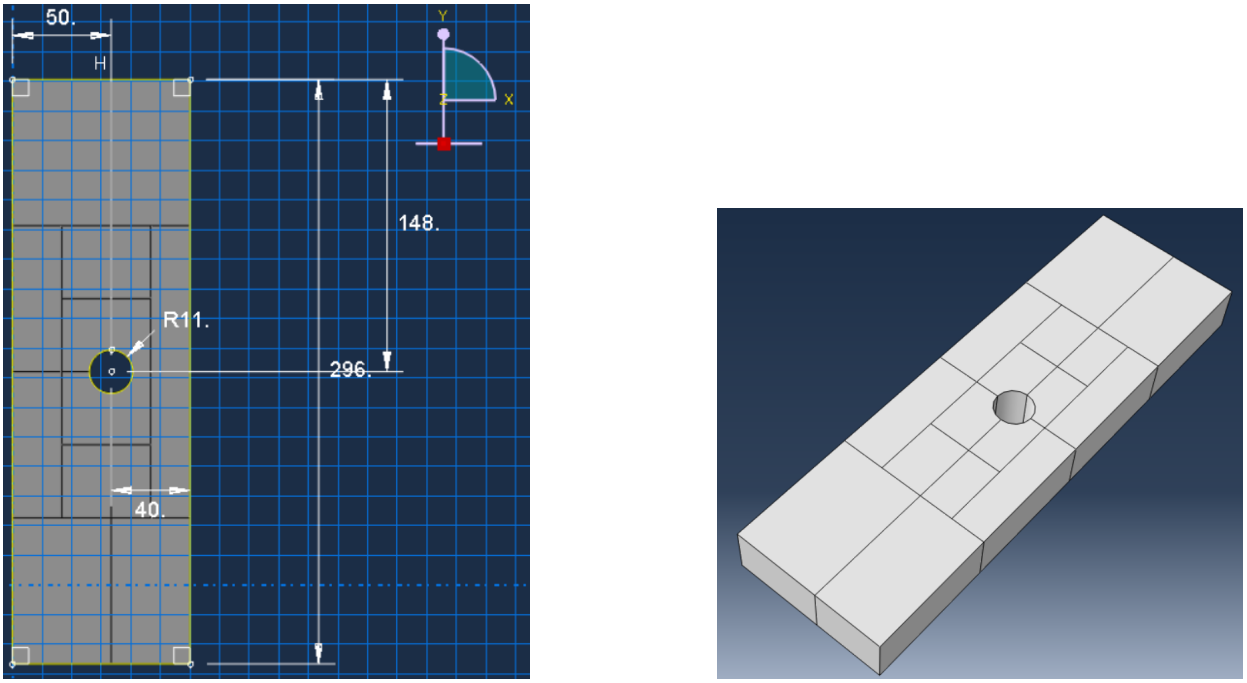

(a) 2D view of the foundation (all dimensions in mm) (b) 3D view of the foundation

Figure 4.4: Illustration of the foundation part (grid spacing: 15 mm)

- **Bolt**
  The bolt, nut and washers are modelled as a single solid part for simplicity and computational efficiency. Since bolt failure governs the structural response, its modelling is critical. The bolt comprises threaded and unthreaded sections, as shown in Figures 4.5a and 4.5b.

  As already mentioned, the bolts used are of grade 8.8 and type HR, providing an ultimate engineering tensile strength (Equation 3.3). The bolt has both a threaded and an unthreaded portion. The gross cross-sectional area of the unthreaded portion and the effective tensile area for the threaded section were previously calculated in Equations 3.1 and 3.2, respectively.

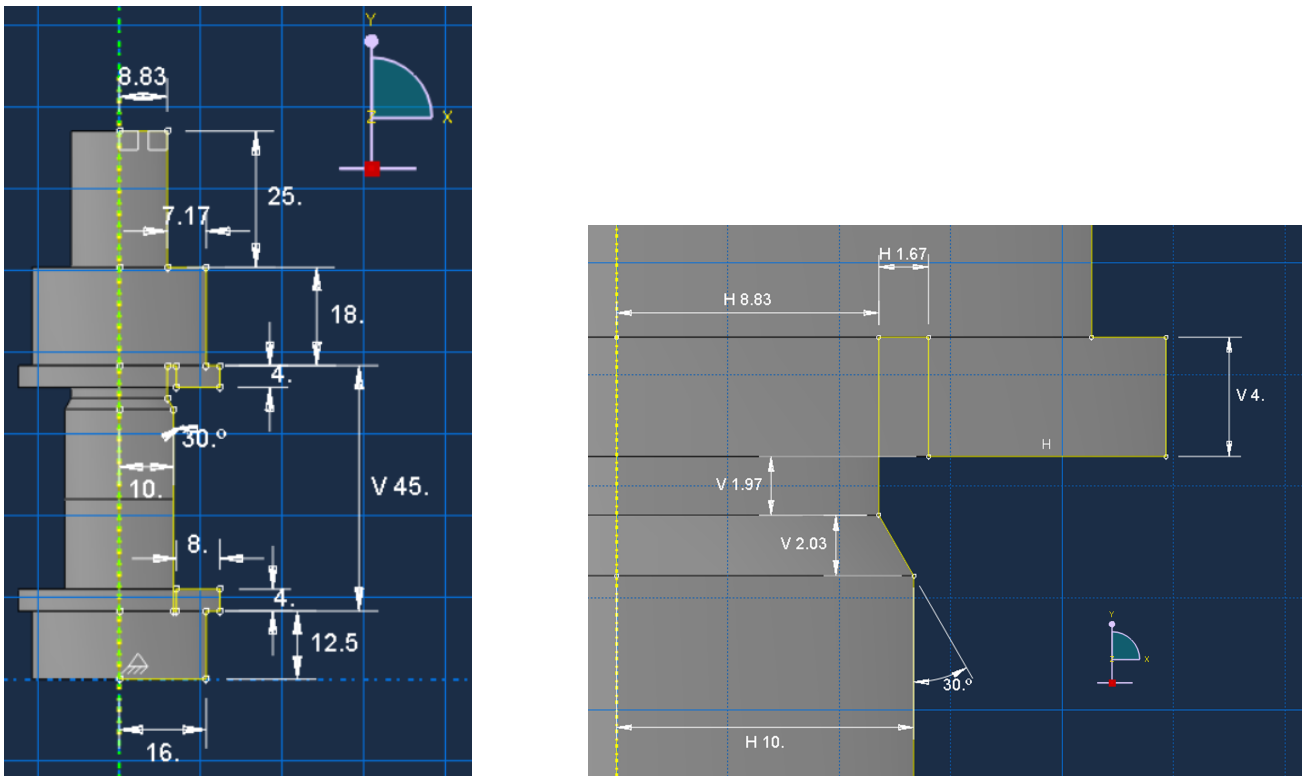

(a) Bolt dimensions (2D)

(b) Detailed bolt sketch (transition area)

Figure 4.5: Bolt modelling and dimensions (all dimensions in mm)

The washers are modelled based on EN 14399-6 (M20) from the FATOR catalog [15], with dimensions given in Figures 4.6 and Table 4.1.

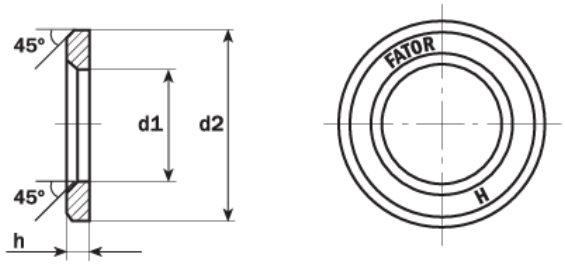

Figure 4.6: Washer dimensions [15]

Parameter	Value	Unit
d_1	21	mm
d_2	37	mm
h	4	mm

Table 4.1: Geometrical parameters of the washer

- **Assembly**
  To replicate the experimental conditions reported in [3] and to prevent slippage of the T-stub on the support at low loads, the bolt was intentionally placed eccentrically. Specifically, the T-stub was shifted in the direction of the shear force so that the bolt shank was in contact with the hole surfaces of both the T-stub flange and the support. This arrangement also eliminates numerical instabilities due to rigid body motion and ensures initial contact across all relevant surfaces.

  The contact regions are highlighted in Figure 4.7, which shows the interface between the bolt shank and both the foundation and the T-stub flange. The shear force applied on the T-stub is directed to the left in the figure.

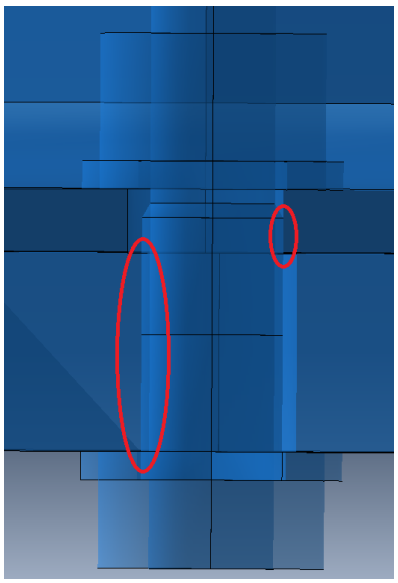

Figure 4.7: Assembly cut view showing contact interfaces

The final assembled view is presented in Figure 4.8.

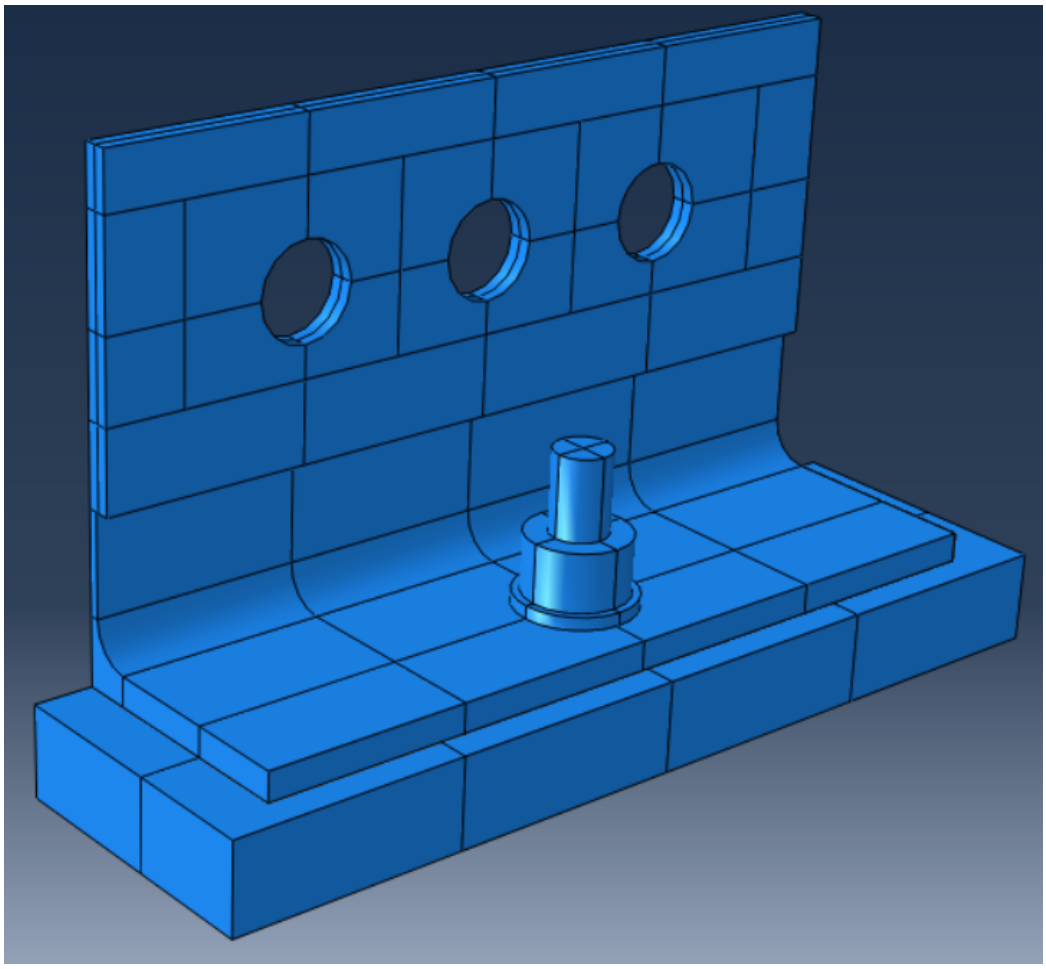

Figure 4.8: Complete model assembly

4.1.2 Material constitutive laws

The numerical model incorporates three different materials, each defined by its stress-strain relationship. All materials share a Young's modulus E of 210 000 MPa and a density of $7.85 \cdot 10^{-9}$ T/mm^3.

These materials correspond to the three structural components introduced in Section 4.1.1: the **foundation**, the **bolt** and the **T-stub**. The materials used for the foundation and the bolt are modelled using simplified elastic-plastic **bilinear** constitutive laws. In contrast, the T-stub is modelled using a more refined **quad-linear** stress-strain relationship, developed according to the guidelines of FprEN 1993-1-14:2025 [22], as illustrated in Figure 4.9 and mathematically defined in Equation 4.1.

Since this study focuses on the pre-damage response of the T-stub, material degradation is not considered. Therefore, damage-related material properties are not included in the analysis.

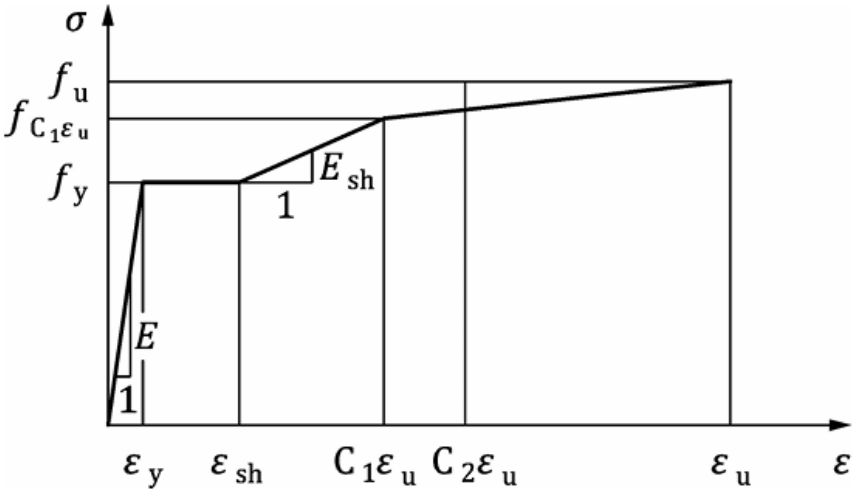

Figure 4.9: Quad-linear stress-strain relationship for the T-stub material [22]

The quad-linear constitutive law is defined by the following piecewise function:

$$\sigma(\varepsilon) = \begin{cases} E\,\varepsilon & \text{for } \varepsilon \leq \varepsilon_y \\ f_y & \text{for } \varepsilon_y < \varepsilon \leq \varepsilon_{sh} \\ f_y + E_{sh}(\varepsilon - \varepsilon_{sh}) & \text{for } \varepsilon_{sh} < \varepsilon \leq C_1\varepsilon_u \\ f_{C_1\varepsilon_u} + \dfrac{f_u - f_{C_1\varepsilon_u}}{\varepsilon_u - C_1\varepsilon_u}(\varepsilon - C_1\varepsilon_u) & \text{for } C_1\varepsilon_u < \varepsilon \leq \varepsilon_u \end{cases} \tag{4.1}$$

where:

- $\varepsilon_y = f_y/E$ is the yield strain (with f_y the yield strength),
- ε_{sh} is the hardening strain, which is given by:

$$\varepsilon_{sh} = 0.1\frac{f_y}{f_u} - 0.055 \text{ but } 0.015 \leq \varepsilon_{sh} \leq 0.03 \tag{4.2}$$

- ε_u is the ultimate strain, which is given by:

$$\varepsilon_u = 0.6\left(1 - \frac{f_y}{f_u}\right) \text{ but } 0.06 \leq \varepsilon_u \leq A \tag{4.3}$$

where A denotes the "elongation after fracture" as defined in the relevant product standard [22].

- C_1 is a material coefficient which is given by:

$$C_1 = \frac{\varepsilon_{sh} + 0.25\,(\varepsilon_u - \varepsilon_{sh})}{\varepsilon_u} \tag{4.4}$$

- E_{sh} is a strain hardening modulus which is given by:

$$E_{\text{sh}} = \frac{f_u - f_y}{C_2 \cdot \varepsilon_u - \varepsilon_{sh}} \tag{4.5}$$

- C_2 is a material coefficient which is given by:

$$C_2 = \frac{\varepsilon_{sh} + 0.4\,(\varepsilon_u - \varepsilon_{sh})}{\varepsilon_u} \tag{4.6}$$

To prepare the material data for input into Abaqus, the engineering strain must first be converted to plastic strain by subtracting the elastic component:

$$\varepsilon_{\text{pl, eng}} = \varepsilon_{\text{eng}} - \varepsilon_{\text{el, eng}} \tag{4.7}$$

Once the plastic strain has been obtained, it must be converted – along with the corresponding stress values – into true stress-true strain properties. This transformation is necessary for compatibility with Abaqus, which requires input data in terms of true stress and plastic (true) strain for material modelling.

The Piluso model, introduced in [23] and validated in [24], is used to refine the post-yield behaviour of the T-stub. The model employs a true stress-strain relationship, obtained from the engineering stress-strain data via the following conversion formulas:

$$\varepsilon_{\text{true}} = \ln(1 + \varepsilon_{\text{eng}}) \tag{4.8}$$

$$\sigma_{\text{true}} = \sigma_{\text{eng}}(1 + \varepsilon_{\text{eng}}) \tag{4.9}$$

Abaqus interprets the final point of the stress-strain curve as the onset of perfectly plastic behaviour, maintaining a constant stress level beyond that point.

T-stub (Plate) material properties

The T-stub material follows the quad-linear relationship. Material properties are summarized in Table 4.2.

Specimen	f_y [MPa]	f_u [MPa]	E [MPa]
1CC	392.2	523.2	210 000

Table 4.2: Material properties of the plate (T-stub)

The computed parameters for the quad-linear law, following Equations in 4.1, are:

$$\varepsilon_y = 0.001867, \quad \varepsilon_{sh} = 0.01996, \quad \varepsilon_u = 0.15$$

$$C_1 = 0.3496, \quad C_2 = 0.4797, \quad E_{sh} = 2514.056$$

The resulting engineering stress-strain data are summarized in Table 4.3.

Point	σ [MPa]	ε [-]
1	392.2	0.001867
2	392.2	0.01996
3	474.075	0.0525
4	523.2	0.15

Table 4.3: Engineering stress-strain data for the T-stub plate

After subtracting the elastic strain (ε_y), the adjusted values are given in Table 4.4a, and finally converted to true values in Table 4.4b.

Point	σ [MPa]	ε [-]
1	392.2	0
2	392.2	0.01809
3	474.075	0.05066
4	523.2	0.14836

(a) Plastic engineering stress-strain data (plate)

Point	σ [MPa]	ε [-]
1	392.2	0
2	399.29	0.0179
3	498.09	0.0494
4	600.82	0.1383

(b) True stress-strain data for the T-stub plate

Table 4.4: Plastic and True strain-strain data for the T-stub plate

These results are visualized in Figure 4.10.

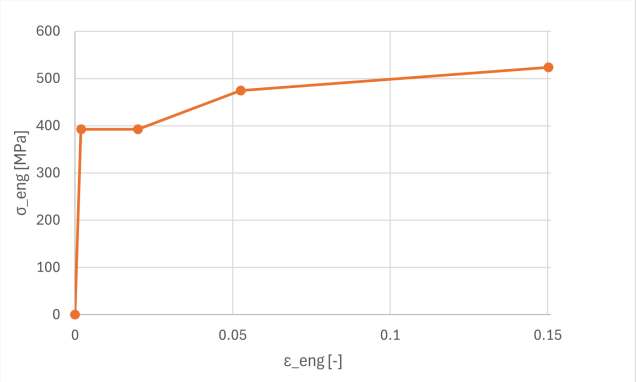

(a) Engineering stress-strain

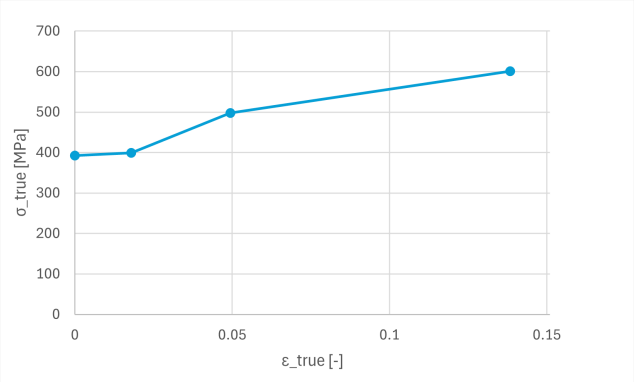

(b) True stress-strain

Figure 4.10: Stress-strain relationships for the T-stub plate

Note: In Abaqus, the stress is assumed constant for strains exceeding 0.1383, corresponding to the last point in the true stress-strain data.

Bolt material properties

As discussed in Section 2.1.3, the average failure load for class 8.8 bolts was 228.829 kN. With a tensile stress area of 245.04 mm^2 (see Section 4.1.1), the ultimate tensile strength is:

$$f_{ub} = \frac{228\,829}{245.04} = 933.83 \text{ MPa} \tag{4.10}$$

It is assumed that the stress increases linearly up to the ultimate strength f_{ub}, beyond which a perfectly plastic behaviour is considered. The considered engineering ultimate strain, corresponding to this ultimate strength, is calculated as:

$$\varepsilon_u = \frac{f_{ub}}{E} = \frac{933.83}{210\,000} = 0.0044 \tag{4.11}$$

An ultimate strain value of 0.05 was adopted for the bolt material, consistent with experimental observations by Daniello [25] on M20 bolts under complex loading conditions. After conversion, the corresponding true stress-strain values are reported in Table 4.5 and illustrated in Figure 4.11.

Point	σ [MPa]	ε [-]
1	933.83	0.0044
2	933.83	0.05

(a) Engineering stress-strain

Point	σ [MPa]	ε [-]
1	933.83	0
2	976.366	0.0445

(b) True stress-strain

Table 4.5: Bolt stress-strain data

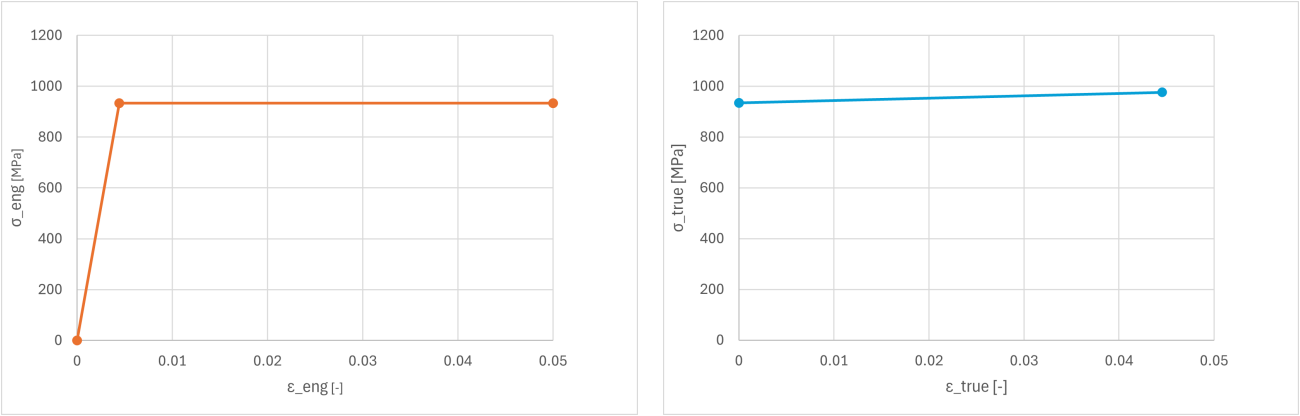

(a) Engineering stress-strain (b) True stress-strain

Figure 4.11: Stress-strain relationships for the bolt material

Foundation material properties

The foundation constitutive law is considered as a bi-linear relationship. The values to consider are the same as the values of point 1 and point 4 of the plate. The *engineering* and *true* stress-strain values of the foundation, reported in Tables 4.6a and 4.6b, are illustrated in Figures 4.12a and 4.12b, respectively.

point	σ [MPa]	ϵ [-]
pt 1	392.2	0.001867
pt 2	523.2	0.15

(a) *engineer*

point	σ [MPa]	ϵ [-]
pt 1	392.2	0
pt 2	600.82	0.1383

(b) *true*, plastic

Table 4.6: Foundation stress-strain properties

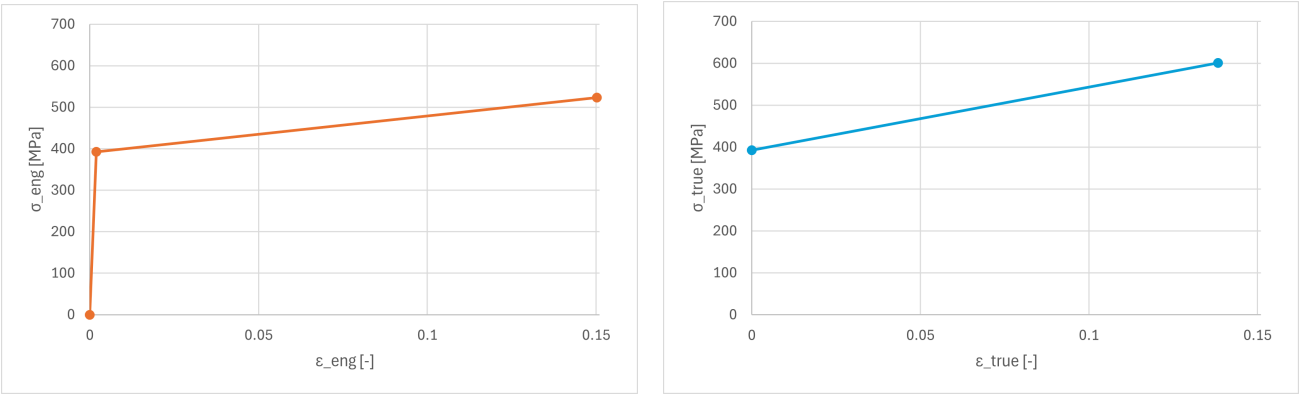

(a) *Engineer* (b) *True*

Figure 4.12: Foundation stress-strain relationship

4.1.3 Mesh definition

The various components modelled in the finite element software were discretized using a sufficiently refined mesh to ensure accurate stress and strain predictions. The element type selected for all components was C3D8R, which is an 8-node linear brick element with reduced integration. Hexahedral elements were used in combination with the "structured" mesh technique to promote regularity and accuracy.

An appropriate partitioning of each geometry was conducted to facilitate meshing, ensuring that each part could be adequately discretized into smaller subregions.

A mesh size of 3 mm was adopted for the bolt, foundation and T-stub. This size provides an adequate number of elements across the T-stub flange thickness and within the bolt to effectively capture stress and strain distributions. This meshing strategy was inspired by the methodology presented by Mancini [3].

Each component of the model, along with its corresponding mesh, is shown in Figures 4.13 and 4.14. The complete assembly of the meshed components is presented in Figure 4.15.

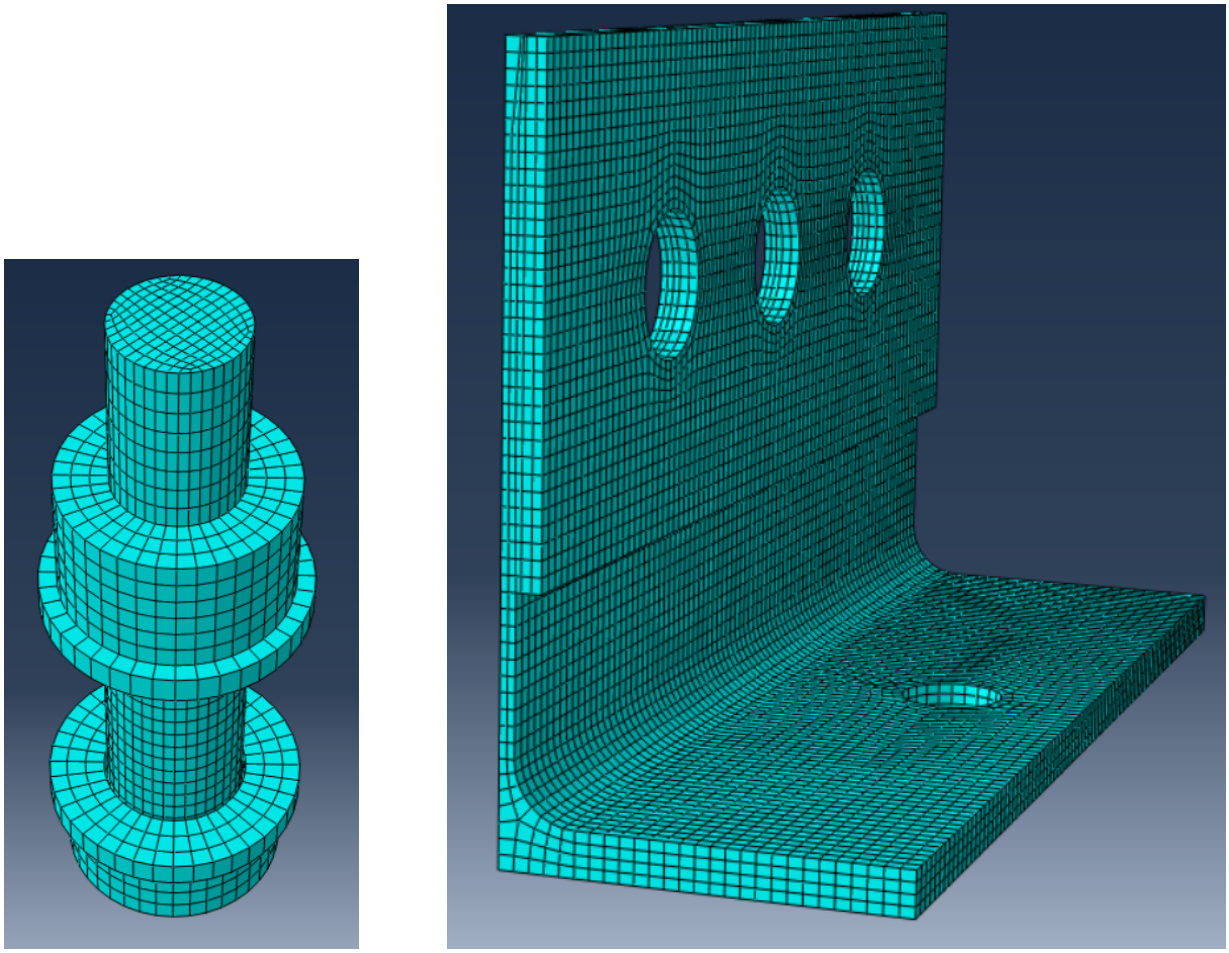

(a) Bolt (b) T-stub

Figure 4.13: Illustration of the meshed bolt and T-stub

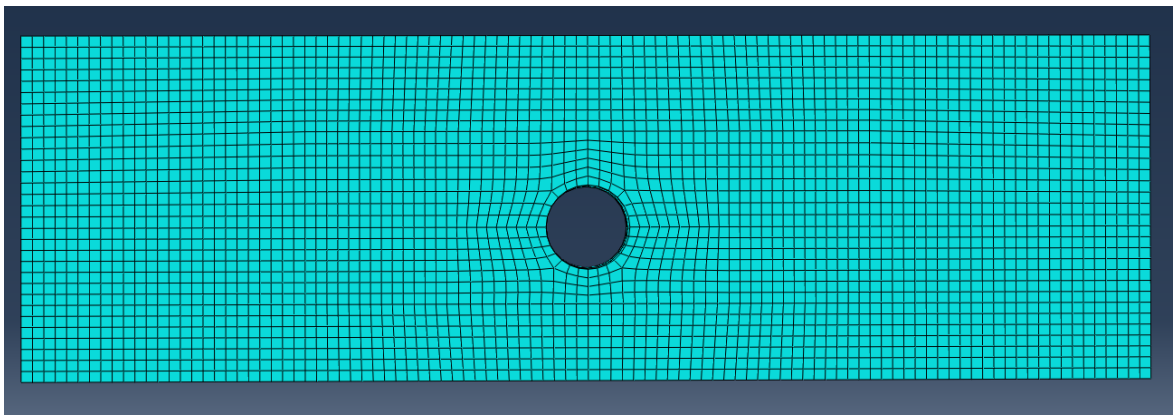

(a) Foundation

Figure 4.14: Illustration of the meshed foundation

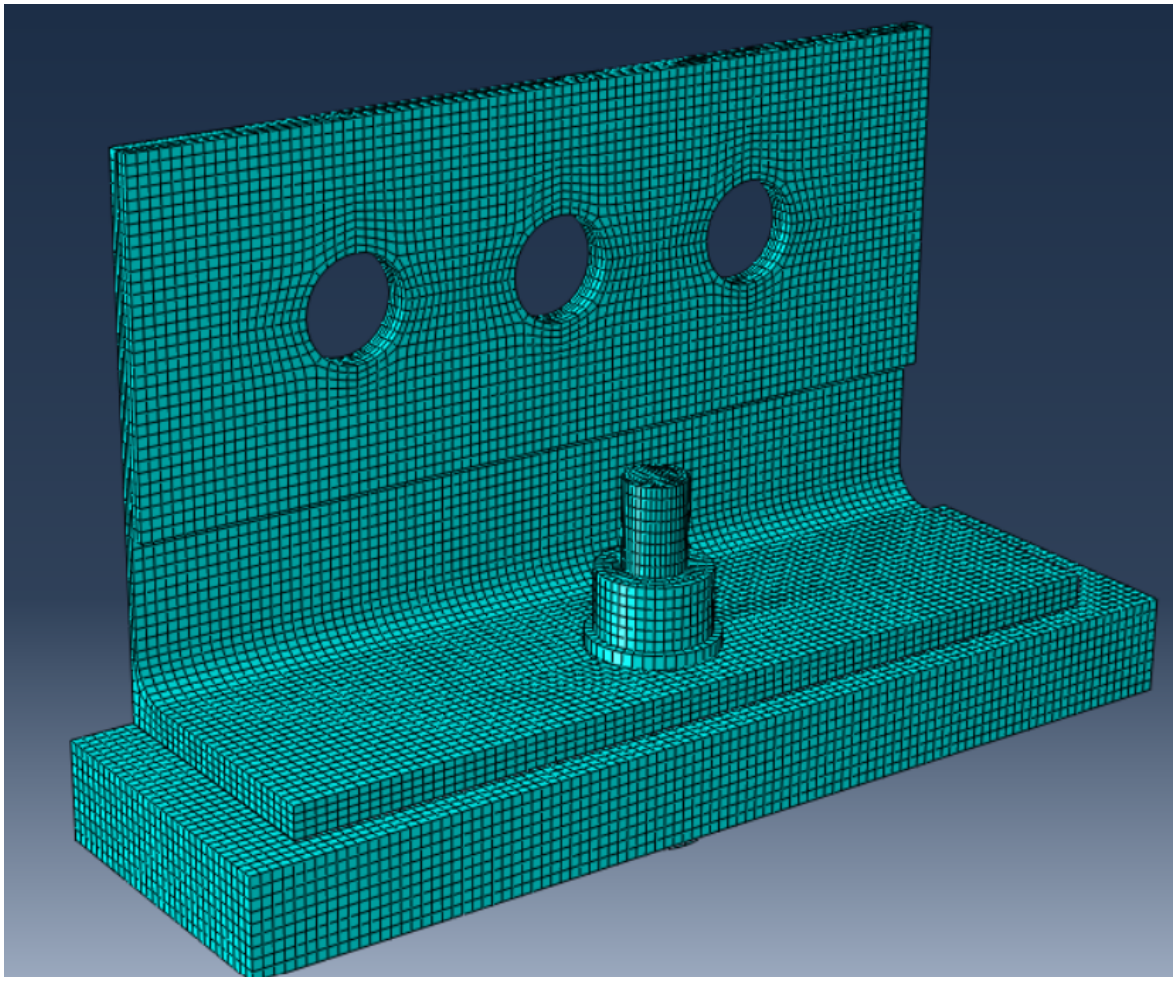

Figure 4.15: Assembly of meshed components

4.1.4 Interactions

The three components are assembled as shown in Figure 4.15, resulting in multiple contact interfaces. Contact interactions were modeled with a "Hard Contact" formulation in the normal direction, while tangential behaviour was governed by Coulomb friction, adopting a friction coefficient of 0.3.

Accurate definition of these interfaces is crucial to reproduce the real contact behaviour observed during experimental tests. In total, seven contact zones were defined:

- Interaction 1: Bottom surface of the flange *with* top surface of the foundation
- Interaction 2: Bottom surface of the top washer *with* top surface of the flange
- Interaction 3: Inner surface of the flange hole *with* transition between threaded and unthreaded parts of the bolt
- Interaction 4: Inner surface of the flange hole *with* unthreaded part of the bolt
- Interaction 5: Inner surface of the flange hole *with* threaded part of the bolt
- Interaction 6: Top surface of the bottom washer *with* bottom surface of the foundation
- Interaction 7: Inner surface of the foundation hole *with* unthreaded part of the bolt

These contact definitions are illustrated in Figures 4.16 and 4.17.

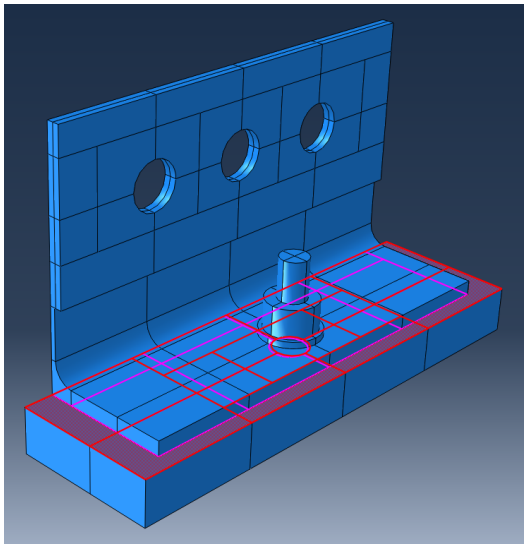

(a) Interaction 1

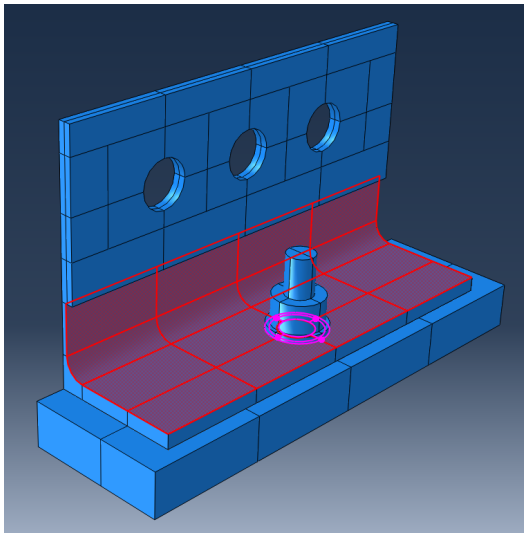

(b) Interaction 2

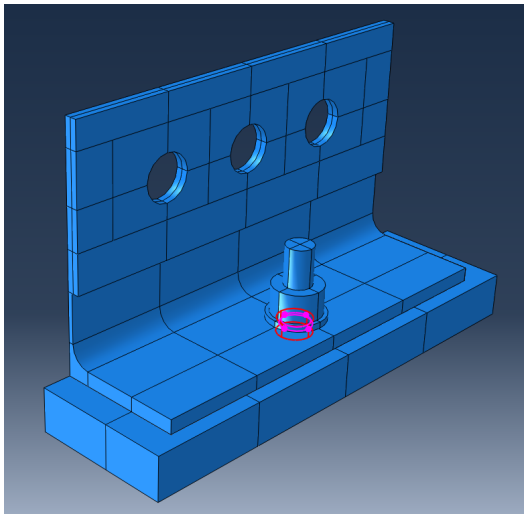

(c) Interaction 3

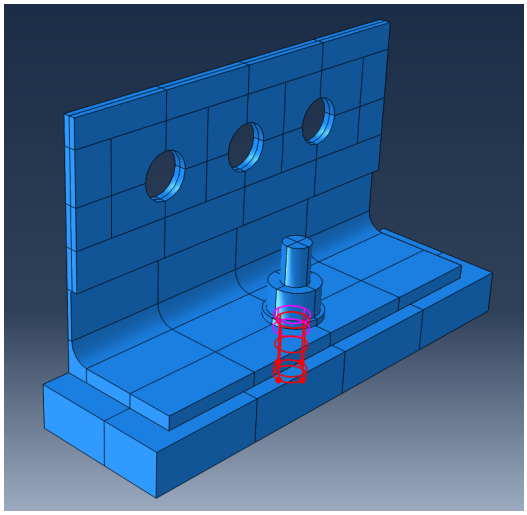

(d) Interaction 4

Figure 4.16: Illustration of assembly interactions 1 to 4

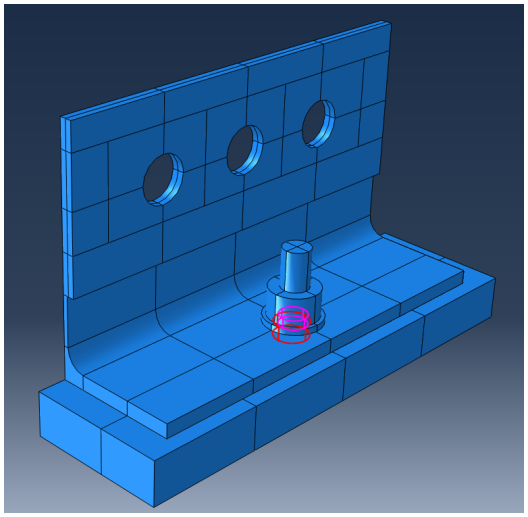

(a) Interaction 5

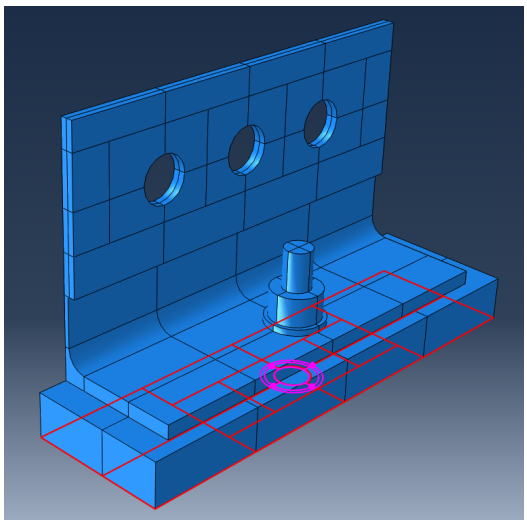

(b) Interaction 6

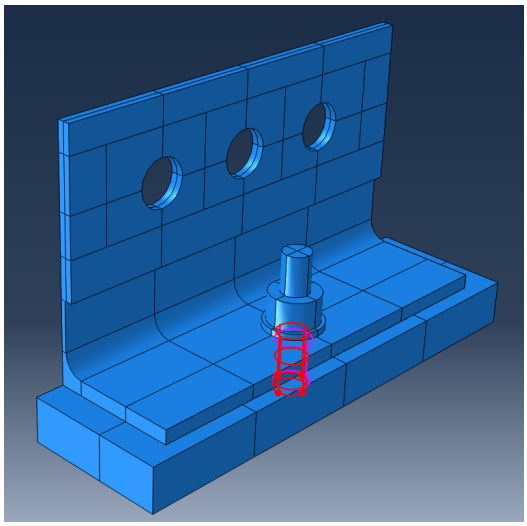

(c) Interaction 7

Figure 4.17: Illustration of assembly interactions 5 to 7

4.1.5 Loads and boundary conditions

The applied boundary conditions, which simulate the restraints imposed during the experimental tests, follow the setup described in Mancini's work [3].

As discussed in Section 4, a symmetry plane was used in the model. A symmetry boundary condition was applied to this plane (Figure 4.18b) to restrict displacements perpendicular to it, ensuring symmetry and global equilibrium. Another boundary condition was applied to the bottom surface of the foundation. This surface was fully constrained (*encastre*) by coupling it to Reference Point 1 (RP1), which was restrained against displacement and rotation in all directions. Through this coupling, the entire surface receives the boundary conditions applied at RP1, as illustrated in Figure 4.18a.

Note: Reference Point 1 (RP1), which is not clearly visible in Figure 4.18a, is located at the midpoint of the foundation length, aligned with the symmetry axis.

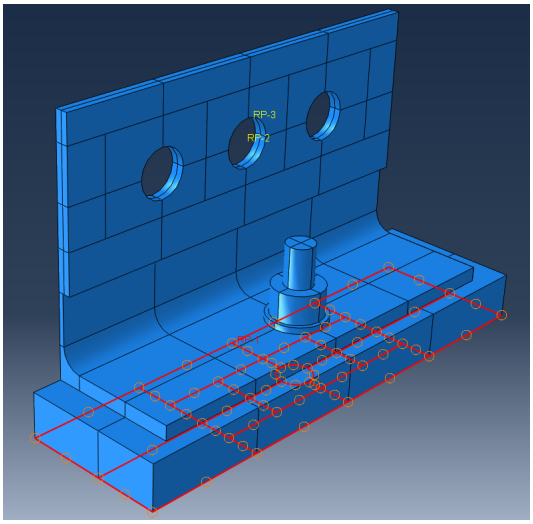

(a) *Encastre* with RP1

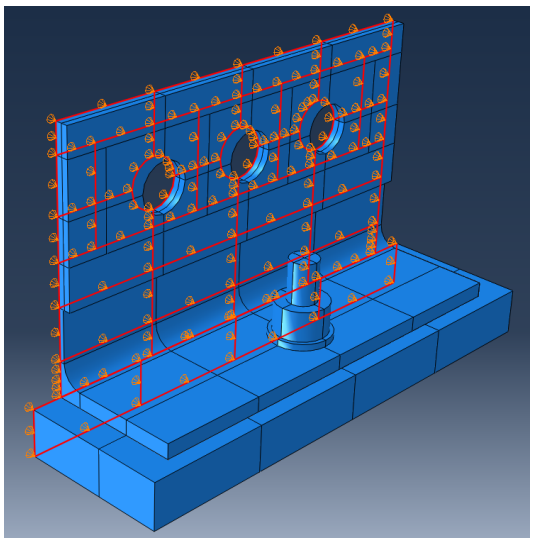

(b) Web symmetry

Figure 4.18: Boundary conditions

The loading was defined in two steps. First, a bolt pretension of 125 kN was applied (Figure 4.19). Then, external loads were gradually increased until collapse. The experimental inclined force was decomposed into two separate forces: a vertical force representing the axial load component and a horizontal force representing the shear load component. The magnitude of these forces depends on the test angle and was applied to the T-stub web, as shown in Figure 4.20a.

To avoid artificial stress concentrations at the load application points, a multi-point constraint (MPC Tie) was used to distribute the loads (Figure 4.20b). This constraint ensures that the pin holes move together, consistent with the experimental configuration.

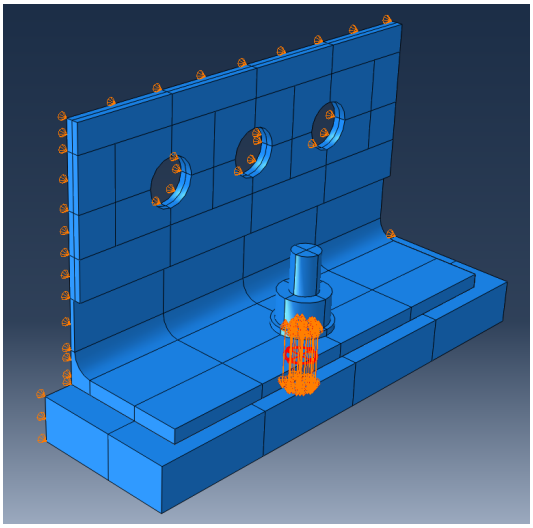

(a) Bolt preloading

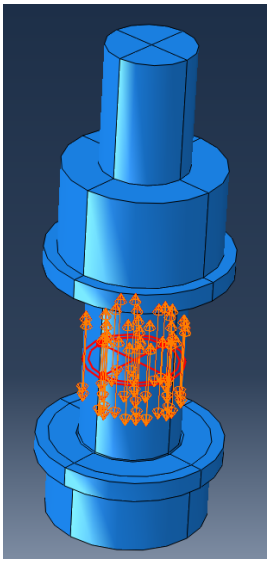

(b) Bolt preloading – zoom

Figure 4.19: Bolt preloading

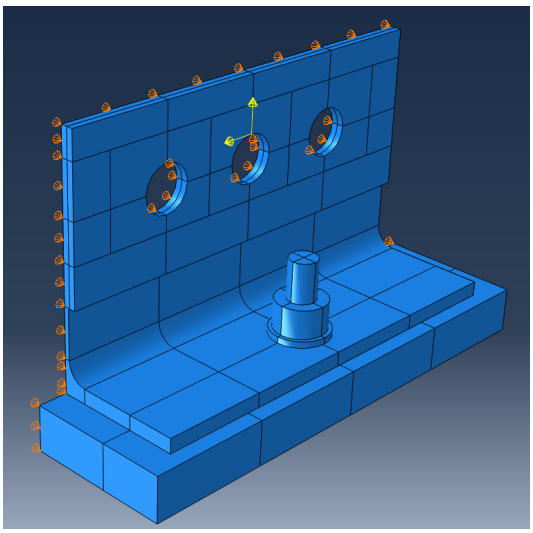

(a) Illustration of force application

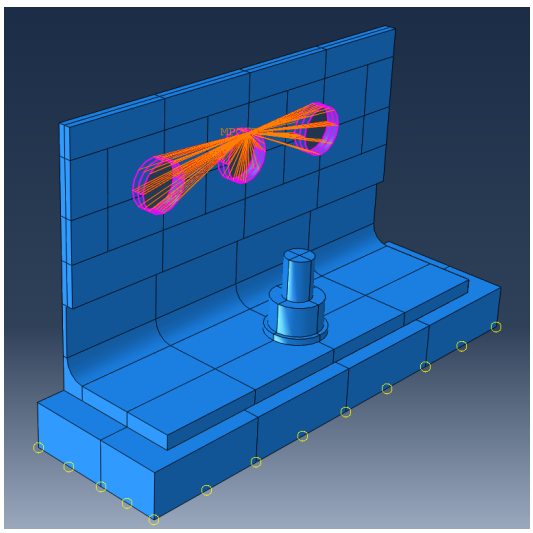

(b) MPC Tie

Figure 4.20: Load application and MPC constraint

Chapter 5

Results and discussions

The analyses presented in this chapter are limited to the material response up to the defined ultimate stress values in the constitutive laws. This limitation arises from the absence of damage modelling in the materials used in the simulations. In other words, material degradation, fracture or any post-ultimate softening behaviour are not implemented in the current model.

As a consequence, the results beyond the last defined point in the stress-strain relationships cannot be considered physically meaningful. For instance, as illustrated in Figure 4.11b, the bolt material is characterized by two points: the onset of plasticity and the ultimate strength. In the case of the bolt, this ultimate stress is 976.366 MPa, corresponding to a true plastic strain of 0.0445 [-]. Beyond this strain, Abaqus assumes a perfectly plastic response by default, which does not reflect the actual behaviour of the material under progressive damage or failure.

Therefore, to ensure the physical relevance of the numerical results, the analysis is restricted to simulation steps in which the plastic strain in the bolt does not exceed 0.0445, corresponding to a stress of 976.366 MPa. As the flange and foundation have not yet reached their respective ultimate limit states, this stress level of 976.366 MPa marks the last valid point of the defined material model. This situation is refered as the ultimate condition, it does not represent the structural collapse of the assembly but rather the onset of material failure.

All results discussed in the subsequent Sections are based on this criterion, ensuring consistency with the assumptions made in the material modelling.

5.1 Validation of the model under pure tension

The T-stub is first analysed under pure axial loading. This loading condition is widely studied in the literature, and its behaviour is well established. According to Eurocode provisions, the bolt is considered to be subjected to pure axial loads, with a uniform distribution of stresses across the radial cross-section.

5.1.1 Observations at the onset of plasticity

Based on the results obtained by Mancini (see Table 3.4), yielding under pure tension occurs at a load of approximately 174 240 N. This implies that, in the load-displacement response, plastic yielding should initiate at an applied force of around 175 000 N.

The raw data extracted from the Abaqus simulation require post-processing. As the model uses Newtons as the force unit and considers only half of the T-stub due to symmetry, the extracted reaction forces must be multiplied by 2 and then divided by 1000 to express the force in kilonewtons.

After this conversion, the timestep corresponding to an axial force (in the Abaqus axis 3 direction) close to 175 000 N can be identified. The closest matching value is 174 611 N. At this load, various field variables can be examined using Abaqus output. The plastic energy dissipation per unit volume (PEMAG) is particularly useful, as it indicates zones where plastic deformation develops. As illustrated in Figure 5.1, plastic strains are observed at the weld toe of the web, confirming the early development of plastic deformation.

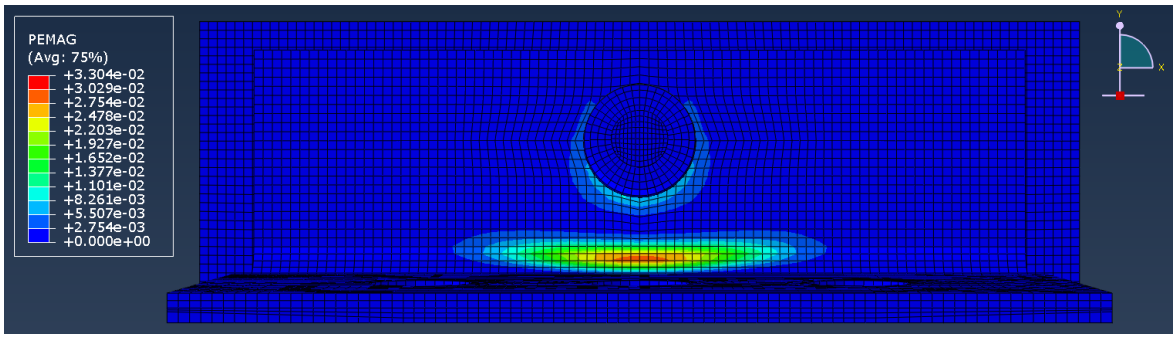

Figure 5.1: Distribution of PEMAG in the T-stub under pure tension

Moreover, the axial force can be calculated at the bolt cross-section using the procedure outlined in Section 3.5.1. For a total applied load of 174 611 N on the T-stub, the load per bolt is calculated to be 142 171 N. This force acts over the threaded area of the bolt, $A_s = 245.04$ mm^2, leading to a predicted tensile stress:

$$f_{u,predicted,b} = \frac{F}{A_s} = \frac{142\,171}{245.04} = 580.2 \text{ MPa} \tag{5.1}$$

In Abaqus, a section cut through the threaded region of the bolt reveals the von Mises stress distribution shown in Figure 5.2. Several key observations are discussed below.

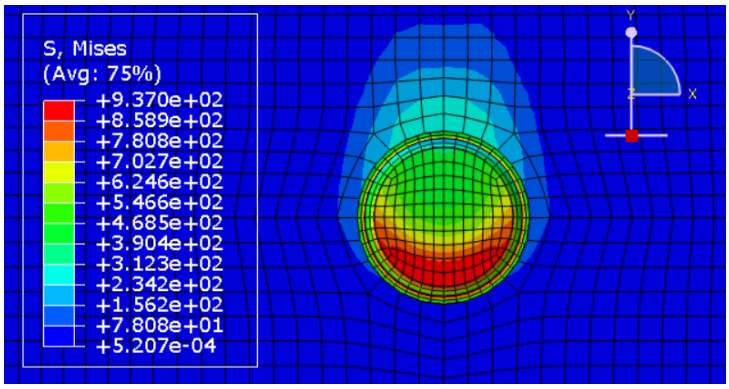

(a) von Mises stress in the bolt

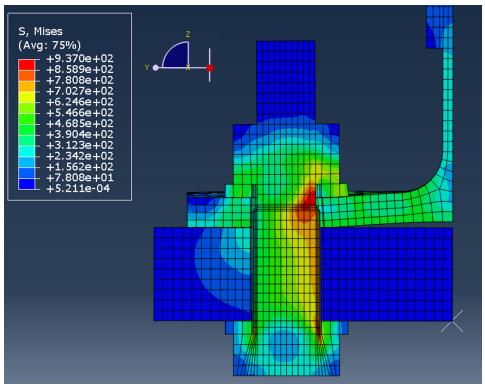

(b) Side view of the assembly

Figure 5.2: Stress distribution at T-stub yield under pure tension

The tensile stress distribution in the bolt is clearly non-uniform, contrary to Eurocode assumptions. The bolt is subjected to tensile forces induced by preloading and T-stub loading. As we know preloading has a uniform effect on bolt, the non-uniform distribution on von Mises stresses must result from T-stub loading. Even under pure axial loading, stress gradients appear across the section of the bolt, suggesting that similar trends – possibly with varying orientations – will emerge under combined loading, as will be discussed in Section 5.5.1.

The measured stress distribution ranges from approximately 300 MPa (on the side furthest from the T-stub web) to around 600 MPa across most of the cross-section, aligning well with the predicted value. A crescent-shaped transitional zone leads to a red-coloured region near the web where stress peak at 934.6 MPa, indicating yielding in the bolt. This plastic behaviour, also confirmed by the PEMAG values (Figure 5.3), with stresses reaching 934.6 MPa in the bolt, is not predicted by the value calculated in Equation 5.1, primarily due to the non-uniform stress distribution across the bolt section.

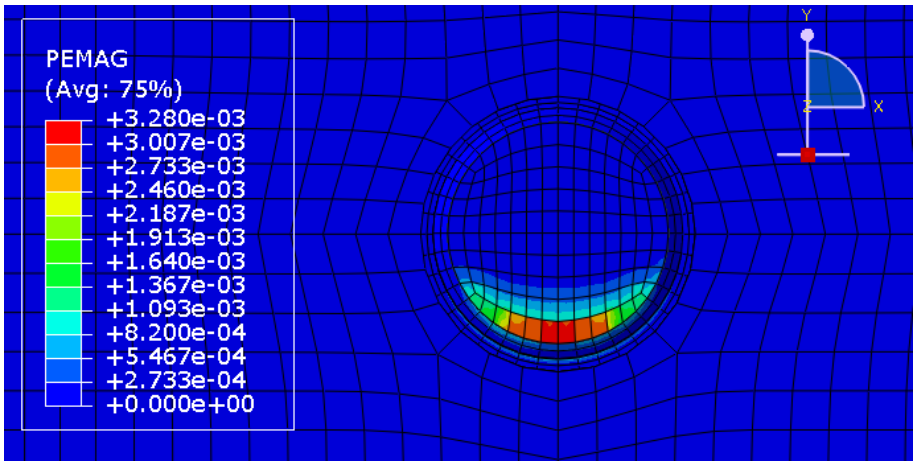

Figure 5.3: PEMAG distribution in the bolt under pure tension, for T-stub yield

5.1.2 Observations at ultimate stress

The ultimate stress state is attained when the first component of the assembly reaches its ultimate stress capacity. The bolt is the first to reach its ultimate limit state of 976.366 MPa. At this simulation time step, the applied force on the T-stub under pure axial loading N is 236, 026 N.

It is clearly observed that, when stresses reach ultimate values, the load on the bolt is not uniformly distributed. Due to plastic deformation, the flange neck undergoes significant distortion, resulting in the formation of an inclination angle at the bolt head level, near the washer. Figure 5.4c illustrates the isolated bolt stress distribution where the deformation and rotation of the bolt head are distinctly noticeable.

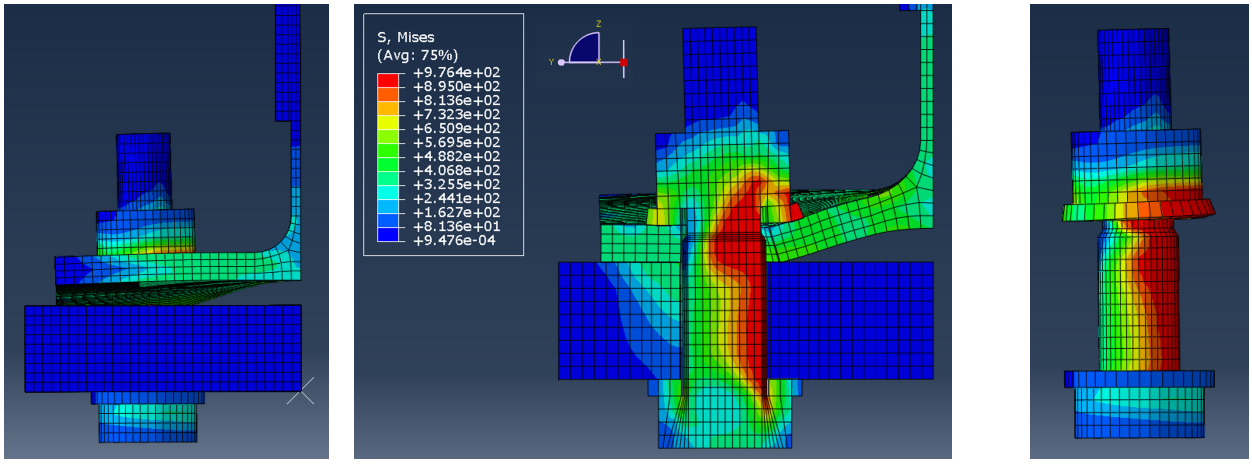

(a) Assembly deformation (b) Cut view of assembly (c) Bolt stress distribution

Figure 5.4: Stress at bolt ultimate load under T-stub axial force

Note: The axis orientation is consistent across all figures and is shown in Figure 5.4b.

The washer plays a critical role in the assembly. At ultimate load, the side of the washer near the web is compressed between the flange and nut, influencing the deformation mode. Furthermore, the lever arm – the distance between the bolt axis and the T-stub web – has a significant effect on bolt head rotation, inducing bending in the bolt shank, which is not accounted for in Eurocode design rules.

The global behaviour is also investigated using displacements recorded by transducers 13 and 14 (Figure 5.5), previously introduced in Figure 2.7. Specimen 1CB, geometrically identical to 1CC, was tested under pure tension and the its load-displacement curve is illustrated in Figure 5.6. Specimen 1CB is designated as the specimen tested under pure tensile force, whereas specimen 1CC is designated as the specimen tested under combined axial and shear forces, as described in Section 2.1.2.

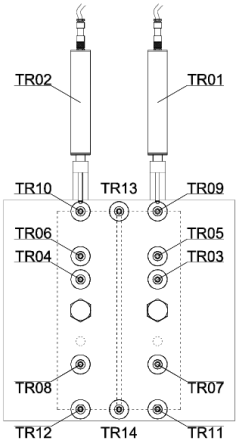

Figure 5.5: Location of transducers instrumentation on the T-stub [3]

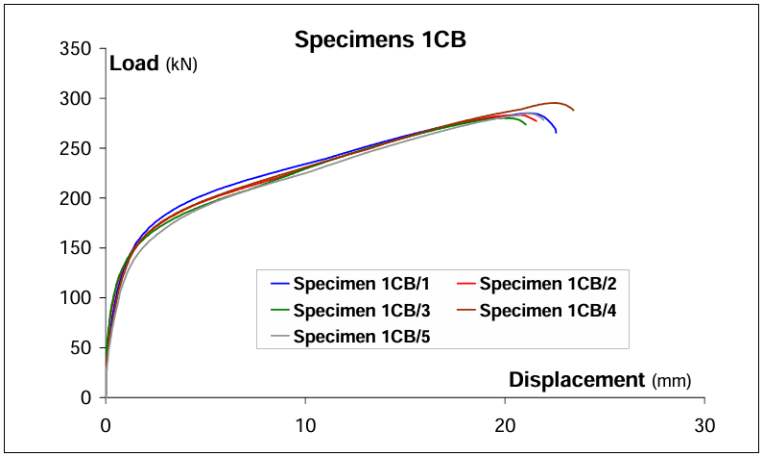

Figure 5.6: Experimental load-displacement response of specimen 1CB under pure tensile force ($\varphi = 90°$) [3]

Experimental and numerical results are compared by calculating the mean vertical displacement (Z-axis) at the location of transducers 13 and 14, referred to as TR13-14. Figure 5.7 shows a good correlation. The dotted curve from Mancini reaches higher load values because the experiment was conducted until collapse failure, whereas the orange continuous curve represents the data up to ultimate load, as previously described. Figure 5.8 illustrates the model under pure tension at the collapse load. The displacements recorded at transducers 13 and 14 are nearly identical, justifying the use of their mean value in the analysis.

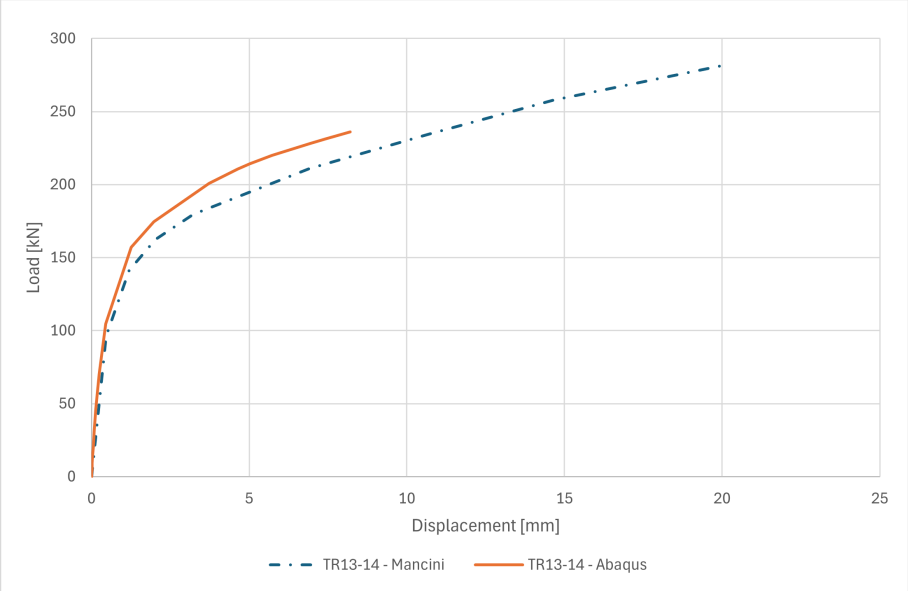

Figure 5.7: Load-displacement curve for $\varphi = 90°$

Note: The orange curve corresponds to a simulation using the "*MPC surface*" constraint, which will be described in detail in the following subsection.

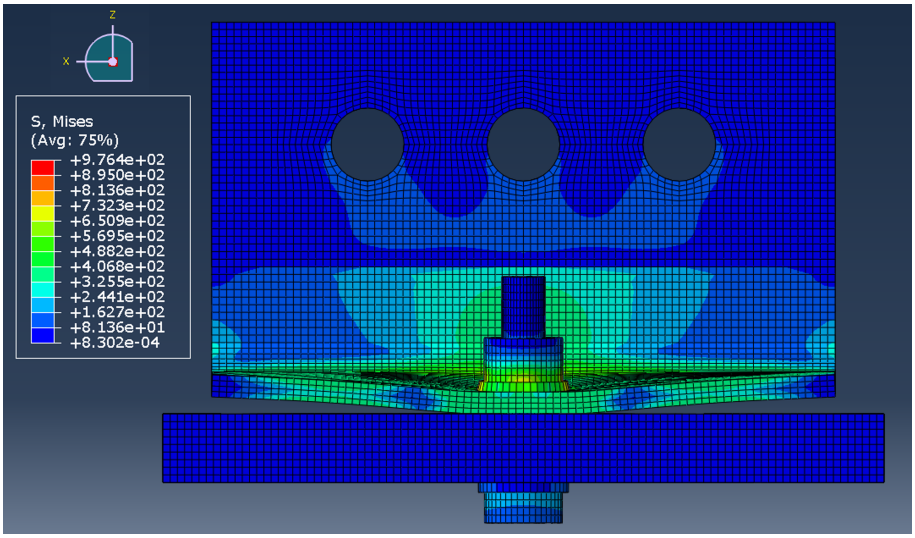

Figure 5.8: von Mises stress for model under pure tension at ultimate load

One discrepancy arises from the bolt thread, which was not modelled. In physical tests, the thread can deform and interact with adjacent surfaces, allowing for increased ductility and displacement. The interaction between the bolt and nut threads is significant and contributes to notable differences in observed behaviour.This omission results in a stiffer numerical response.

Despite this, the model provides a reliable prediction of resistance and reproduces failure Mode 1 accurately. The side view of the flange at ultimate loading, as illustrated in Figure 5.9, clearly shows the formation of two plastic hinges.

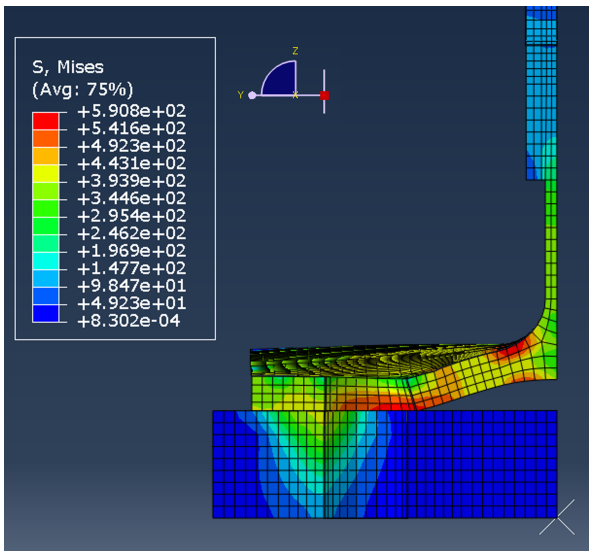

Figure 5.9: Side view of the flange at plasticity

The non-uniform stress distribution in the bolt will be analysed in more detail in the next Section, which considers the influence of inclined loading on stress distribution along the bolt shank.

5.2 Model under inclined force

The behaviour of the T-stub under combined shear and axial forces leads to a critical discussion of the constraints applied on the three pins. Specifically, different assumptions regarding these constraints influence the rotational behaviour, resulting in distinct mechanical responses in the numerical model.

5.2.1 Rotational constraint

As previously discussed in Section 4, the MPC Tie constraint was applied to simulate the load transfer from the experimental apparatus to the T-stub web. This load is introduced through the inner surfaces of three holes, each with a diameter of 30 mm.

The simulations were conducted by applying a force decomposed into two orthogonal components: one perpendicular to the foundation (axial) and one parallel (shear), to replicate the experimental loading. Different tests used varying inclinations of the resultant force vector. Table 5.1 presents the corresponding axial and shear components for an applied force of 350 000 N on a half T-stub model. This force magnitude was arbitrarily chosen; however, since the applied load increases linearly throughout the simulation, selecting a sufficiently high value ensures that the ultimate capacity of the system is reached for every considered inclination angle.

φ [°]	Axial force N [N]	Shear force V [N]
0	0	350 000
15	90 586.6	338 074
30	175 000	303 108.9
45	247 487	247 487
60	303 108.9	175 000
75	338 074	90 586.6
90	350 000	0

Table 5.1: Axial and shear force distribution corresponding to inclination angle φ

To simulate the physical interaction between the pins and the web holes, an MPC Tie constraint was employed, as described in Section 4.1.5. Two distinct modelling assumptions were investigated for the application of this constraint.

The first approach involved applying the MPC Tie only on three discrete circular regions along the edges of the holes, as illustrated in Figure 5.10a. The second approach extended the MPC constraint over the entire inner surfaces of the holes, as shown in Figure 5.10b.

Although neither approach explicitly restricts rotational motion, the extent of the constrained surface significantly influences the rotational freedom of the web. As a result, these two assumptions produce different deformation patterns, which will be analysed in the following sections. A critical discussion of the physical relevance of each modelling strategy is also provided.

Notation: The term *MPC circle* refers to the model where the constraint is applied only on circular edges of the holes. The term *MPC surface* refers to the model where the MPC constraint is applied to the entire inner surface of the pin holes. These two configurations are illustrated in Figure 5.10.

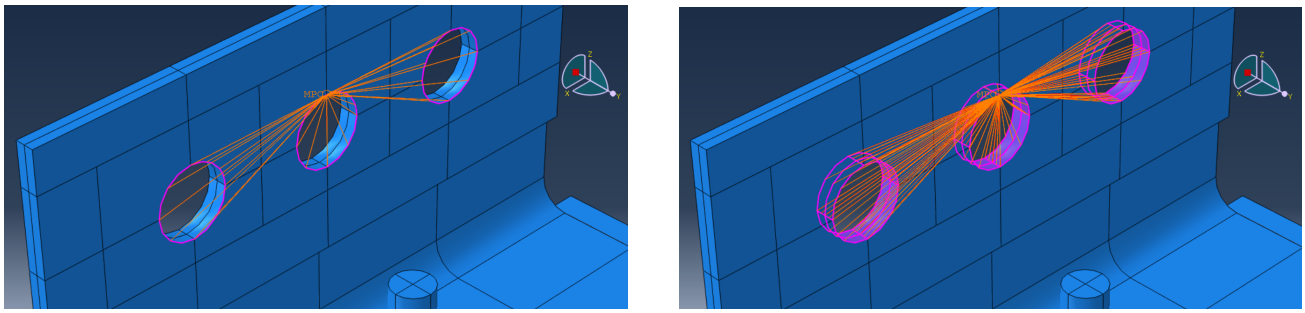

(a) *MPC circle* (b) *MPC surface*

Figure 5.10: Illustration of the different MPC constraint applications

Note: In all further analysis, transducers 13 and 14 are referred to as TR13-14, and transducers 01 and 02 as TR01-02.

5.2.2 Results of TR13-14 for different force inclinations

The variation in constraint application produces markedly different results for inclination angles $\varphi = 0°$, 15°, 45° and 90°, as shown in Figures 5.11 – 5.14. The curves are illustrated for the transducers 13 and 14, measuring displacements perpendicular to the flange. The purple and orange curves correspond to simulations using the *MPC circle* and *MPC surface* constraints, respectively. The dotted blue curves correspond to numerical results from Mancini. These values were extracted from his graphs, which illustrate load-displacement curves for both experimental and numerical results related to transducers 13 and 14. These graphs are provided in Appendix A2.1.

First, the observed difference in displacement between TR13 and TR14 arises from their positions on opposite sides of the T-stub and the orientation of the shear force component. This difference diminishes as the shear component decreases, eventually disappearing under pure axial loading ($\varphi = 90°$). In this case, both transducers record identical displacements, allowing the calculation of a mean displacement value, as discussed in Section 5.1.

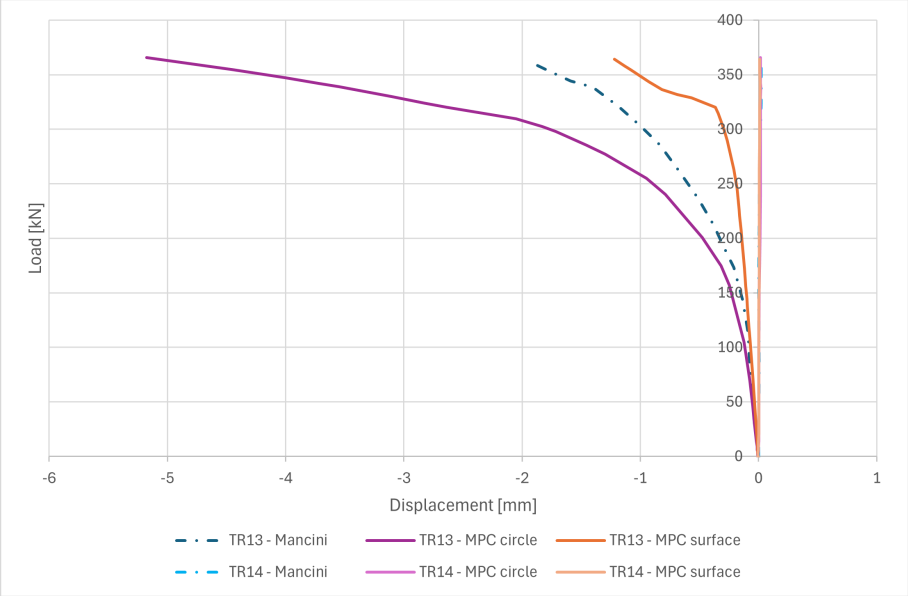

Figure 5.11: Load-displacement curve for $\varphi = 0°$

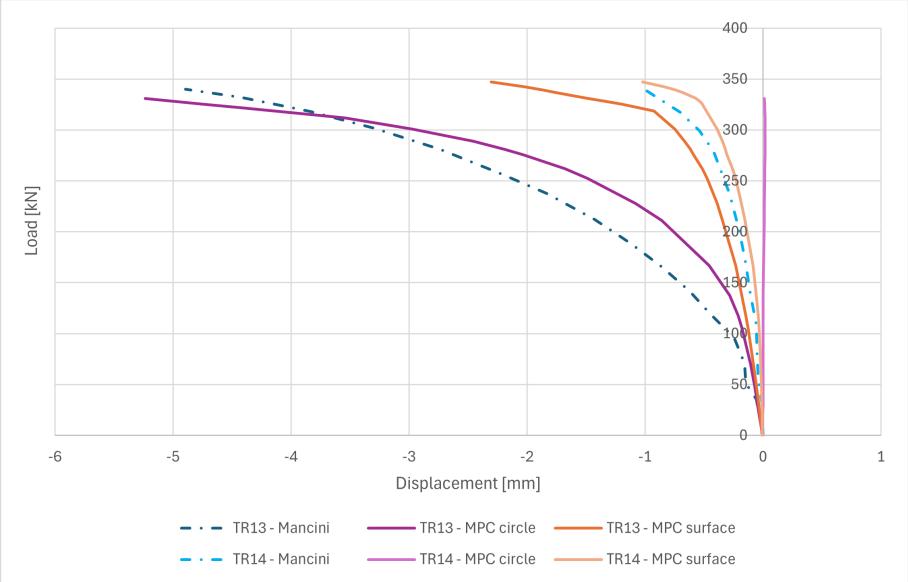

Figure 5.12: Load-displacement curve for $\varphi = 15°$

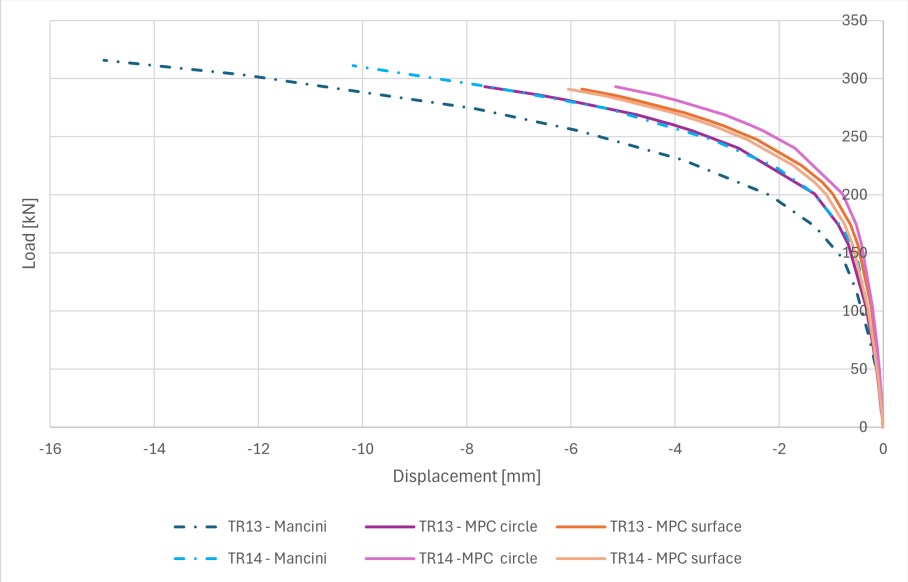

Figure 5.13: Load-displacement curve for $\varphi = 45°$

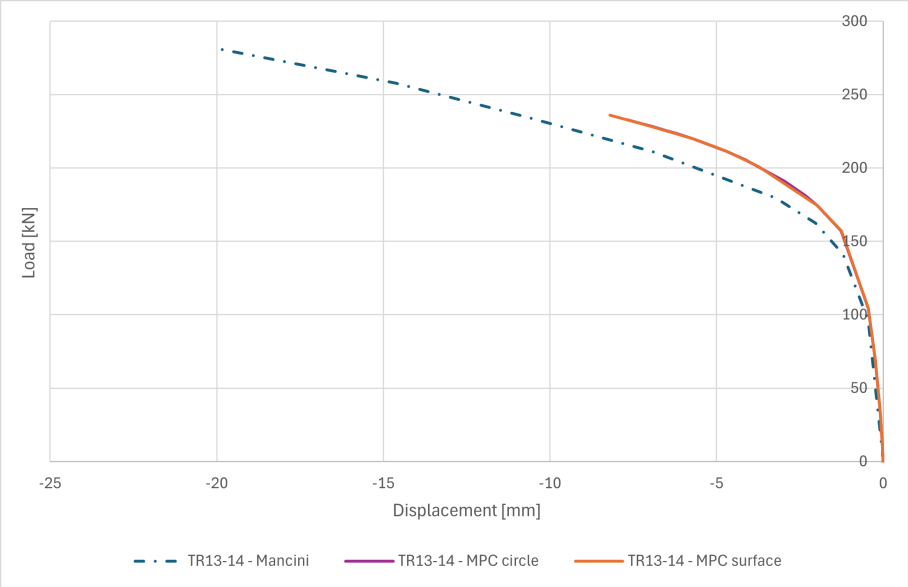

Figure 5.14: Load-displacement curve for $\varphi = 90°$

Note: The load-displacement curves for inclination angles $\varphi = 30°$, $60°$ and $75°$ are provided in Appendix A2.2.

Analysis by angle

- **Angle $\varphi = 0°$: pure shear**
  The two MPC constraint types lead to distinctly different behaviours. The *MPC surface* configuration imposes excessive rotational restraint, resulting in a stiffer response for small displacements. A transition from elastic to plastic behaviour is observed at approximately 320 kN and a negative displacement of 0.36 mm. The change in the slope of the curve indicates the onset of yielding, associated with the bolt reaching its ultimate strength.

In contrast, the *MPC circle* model allows excessive displacement, indicating a more flexible rotational behaviour due to a less constrained interface, as discussed further in Section 5.3.

- **Angle $\varphi = 15°$**
  When moving from the pure shear case ($\varphi = 0°$) to the inclined loading case ($\varphi = 15°$), similar distinctions between the two constraint configurations are observed. When the *MPC surface* constraint is applied, the displacement values are significantly lower for TR13 and slightly lower for TR14, indicating that the rotation of the T-stub is more effectively restrained. The closeness of the TR13 and TR14 curves under this configuration suggests that the T-stub rotates very little, and both sides of the flange remain relatively symmetric in their response.

  In contrast, when the *MPC circle* constraint is used, the rotation is insufficiently restrained. This results in a noticeable increase in displacement, particularly for TR13, while TR14 does not exhibit any significant displacement. This asymmetry indicates that one side of the T-stub loses contact with the foundation, leading to localized uplift, while the other side remains in contact. However, the displacements obtained with the *MPC circle* model for TR13 still remain below those observed in Mancini's experimental campaign, except at load levels exceeding 315 kN, where the values begin to converge.

- **Angle $\varphi = 30°$**
  This inclination angle exhibits a transitional behaviour between the cases of $\varphi = 15°$ and $\varphi = 45°$. The same trends discussed previously for $\varphi = 15°$ are generally observed here as well. However, unlike the 15° case, the TR13 displacement curve under the *MPC circle* constraint does not converge with the experimental results, even at higher load levels, and remains consistently lower throughout. Furthermore, in this configuration, the *MPC circle* model shows a detachment at transducer 14 under higher applied loads, which contrasts with the $\varphi = 15°$ case where continuous contact is maintained throughout the loading.

- **Angle $\varphi = 45°$**
  The influence of the constraint becomes less pronounced as the axial component of the force increases. Both constraint types result in comparable behaviours. However, *MPC circle* results match better the experimental asymmetry. In the *MPC surface* model, rotation appears to be blocked, as identical displacements are observed on both sides of the T-stub.

- **Angles $\varphi = 60°$ and $\varphi = 75°$**
  As the force approaches pure axial inclination, the behaviour is increasingly well predicted. Graphs for these inclination angles are included in the Appendix A2.2.

- **Angle $\varphi = 90°$: pure tension**
  At this angle, the model undergoes no rotation, making the rotational constraint irrelevant. Accordingly, the two MPC configurations show nearly identical results, as illustrated in Figure 5.14.

5.2.3 Summary of TR13-14 displacement responses at varying inclination angles

Summary plots comparing all inclination angles for the *MPC circle* and *MPC surface* constraint are presented in Figure 5.15 and Figure 5.16 respectively. The dotted curves represent the results at transducer 13, while the continuous curves correspond to transducer 14. This figure displays the numerical results from simulations using the two different constraint and should be compared to Figure 2.9, which shows the experimental load-displacement curves obtained by Mancini [3].

MPC circle constraint

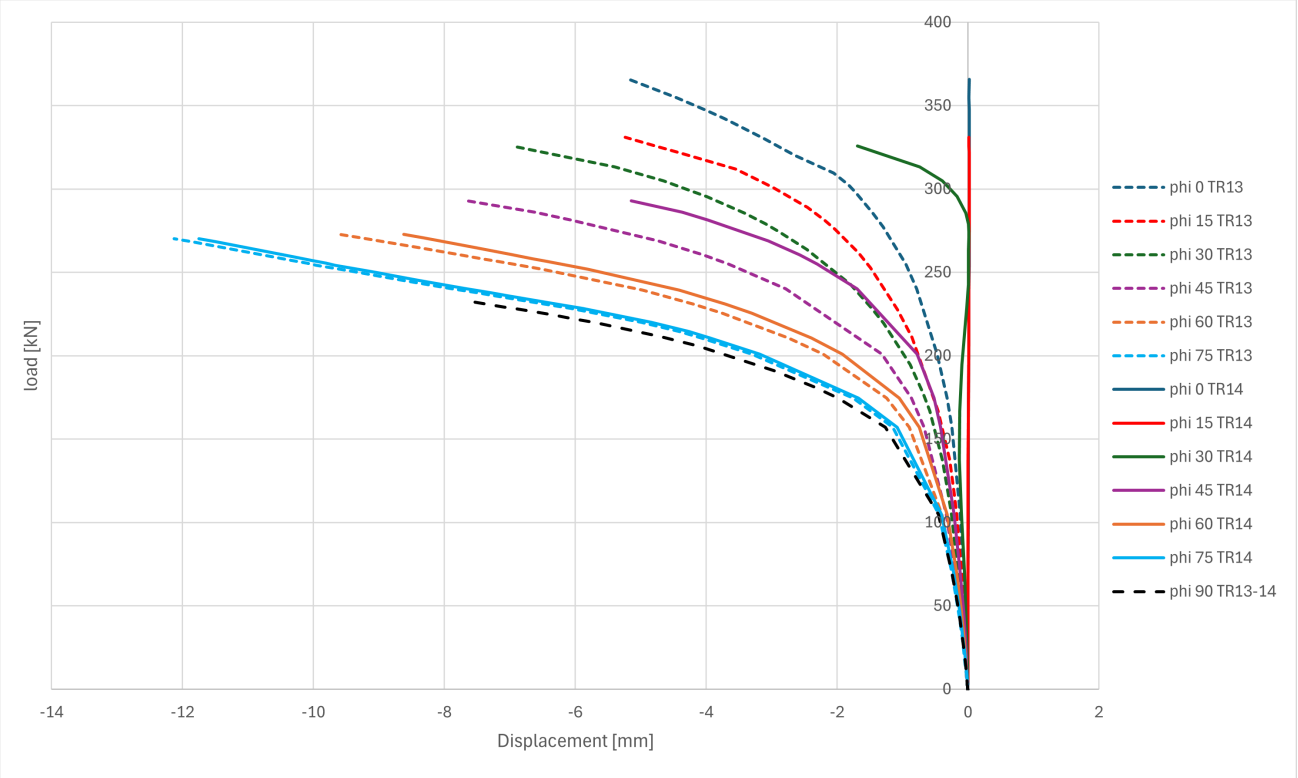

Figure 5.15: TR13 and TR14 load-displacement curves for different values of φ - *MPC circle* constraint

Note: The unique curve for $\varphi = 90°$ illustrates the mean value of TR13 and TR14.

Although the numerical results are not fully consistent with the experimental data, this discrepancy is partly attributed to limited knowledge of the physical properties of certain materials, which could not be accurately implemented in Abaqus. Additionally, material damage was not considered in the definition of the constitutive laws, contributing further to the observed deviations.

The absence of the threaded portion of the bolt on its surface affects the response of the specimen. This impact will be discussed at the end of the next Section (5.2.4), in the subsection "Analysis of TR01-02 displacements".

Nevertheless, the simulations generally exhibit similar trends to those reported by Mancini [3], particularly for higher inclination angles. For angles ranging from 45° to 90°, the numerical results align well with the experimental observations. In contrast, for lower inclination angles (i.e., 0° to 30°), where shear effects dominate, the agreement is less satisfactory.

MPC surface constraint

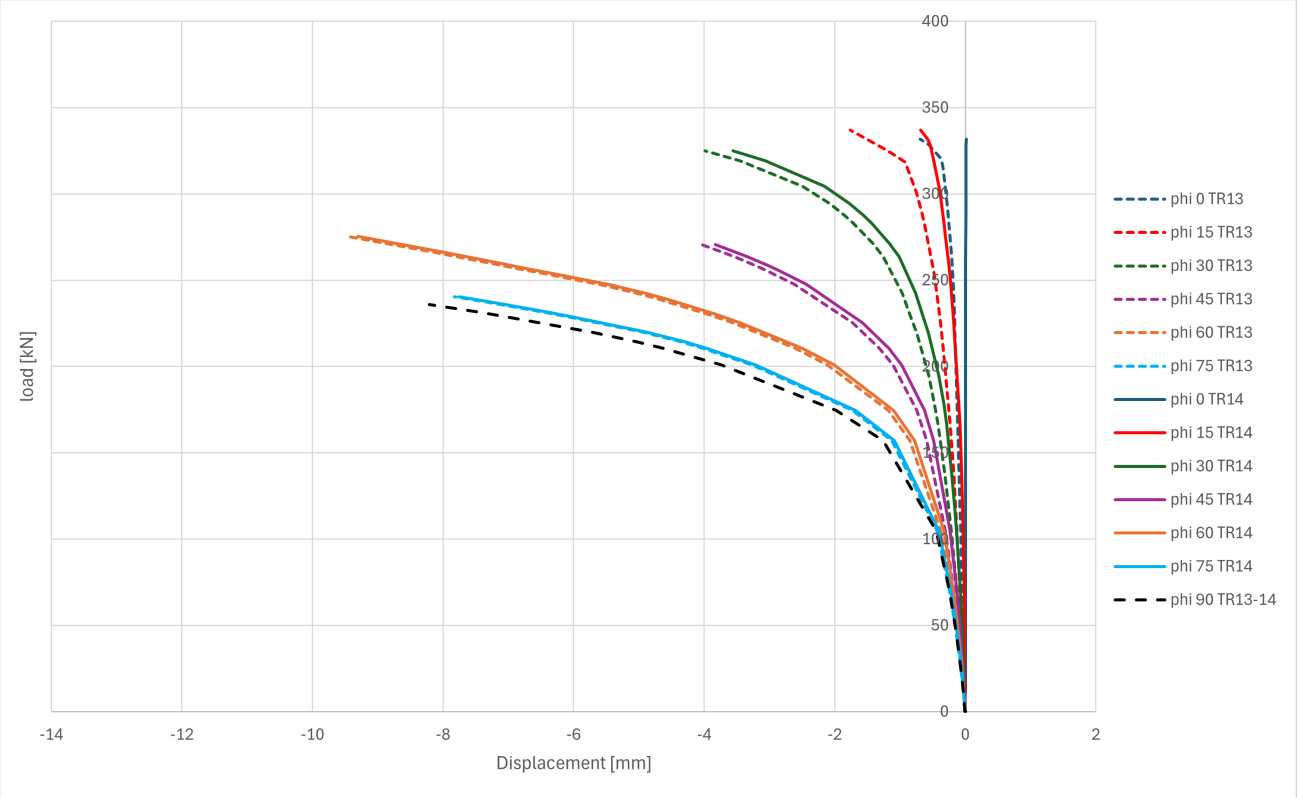

Figure 5.16: TR13 and TR14 load-displacement curves for different values of φ - *MPC surface* constraint

Note: The unique curve for $\varphi = 90°$ illustrates the mean value of TR13 and TR14.

The application of the *MPC surface* constraint also leads to results that deviate from the experimental data. A notable observation is the significantly smaller displacement difference between TR13 and TR14, along with an overall lower displacement magnitude compared to the experimental curves. These results highlight the strong influence of the constraint type on the behaviour of the model, particularly in limiting the relative displacement for the two sides of the T-stub. The implications of this constraint will be further examined in Section 5.3.

5.2.4 Results of TR01-02 for different force inclinations

Transducers TR01 and TR02, illustrated in Figure 5.5, are used to measure the displacement parallel to the T-stub flange, which is primarily associated with the shear force. In the experimental setup, a screw was inserted between the transducers and the specimen in order to be able to measure the displacements. This solution was adopted to protect the instrumentation from damage in the event of sudden bolt failure.

However, the presence of the screw affects the accuracy of the measurement of displacement because the screw undergoes deformation following that of the T-stub flange. As a result, the measured displacement includes not only a longitudinal component but also a transverse one, caused by flange detachment from the foundation. A post-processing correction was therefore necessary to account for screw rotation and to accurately reconstruct the actual displacement.

The corrected displacement is denoted as d, while the raw displacement recorded by transducers TR01 and TR02 is referred to as TR01-02, as illustrated in Figure 5.17. The screw used in the experimental setup had a length of 30 mm, denoted as L_{tr}, as described by Mancini [3]. By using the displacement recorded by transducers TR09 and TR10 (denoted as TR09-10), it is possible to compute the measured TR01-02 values from the real displacement d, and vice versa.

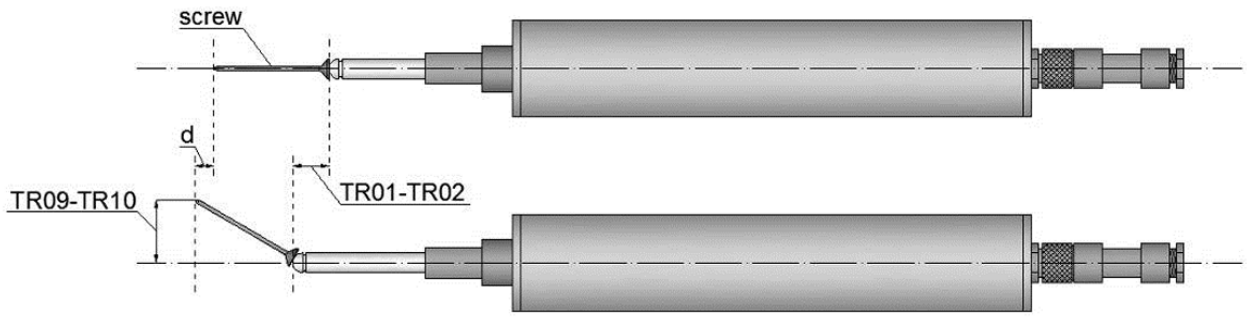

Figure 5.17: TR01 and TR02: measured vs. real displacement [3]

In Mancini's work, graphs are presented with two curves:

- The experimental displacement recorded by transducers TR01 and TR02.
- The corrected Abaqus-simulated displacement in order to mathematically simulate the presence of the screw in the numerical model.

An example of such a comparison is shown in Figure 5.18 for an inclination angle $\varphi = 0°$.

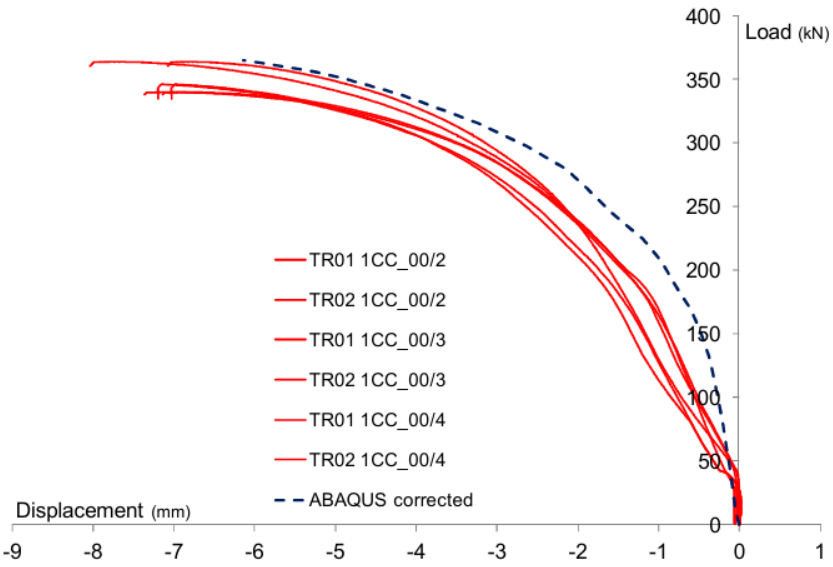

Figure 5.18: TR01-02: load-displacement curve from Mancini [3] for $\varphi = 0°$

Note: Graphs for other inclination angles are available in Appendix A2.3.

The post-processing to obtain the Abaqus-corrected values involves the following steps:

1. To extract the value of TR09-10 from the simulation (only one value is used due to model symmetry).
2. To extract the value of d from the simulation at the TR01-02 location.
3. To calculate the equivalent TR01-02 value using the equations below (5.2 and 5.3) and the geometry illustrated in Figure 5.19.

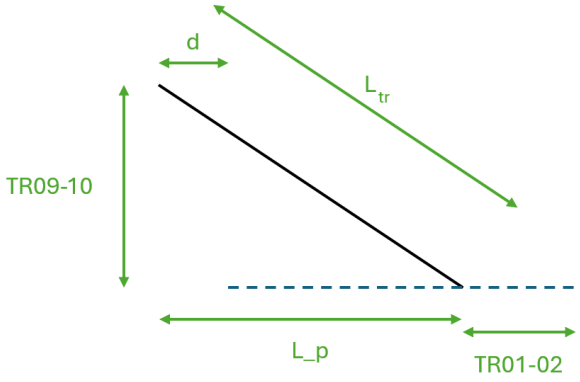

Figure 5.19: Illustration of the post-processing calculation

Note: The dotted blue line represents the initial (non-rotated) position of the screw, while the continuous black line indicates its rotated configuration during testing. The parameter L_p corresponds to the horizontal projection of the screw length in its rotated position, accounting for the transverse displacement component.

$$L_p = \sqrt{L_{tr}^2 - \text{TR09-10}^2} \tag{5.2}$$

$$\text{TR01-02} = d + L_{tr} - L_p \tag{5.3}$$

Figures 5.20 to 5.23 present the load-displacement curves obtained from transducers TR01 and TR02 for inclination angles $\varphi = 0°$, 15°, 45° and 75°. As in previous Section 5.2.2, the purple and orange curves correspond to the numerical simulations using the *MPC circle* and *MPC surface* constraints, respectively.

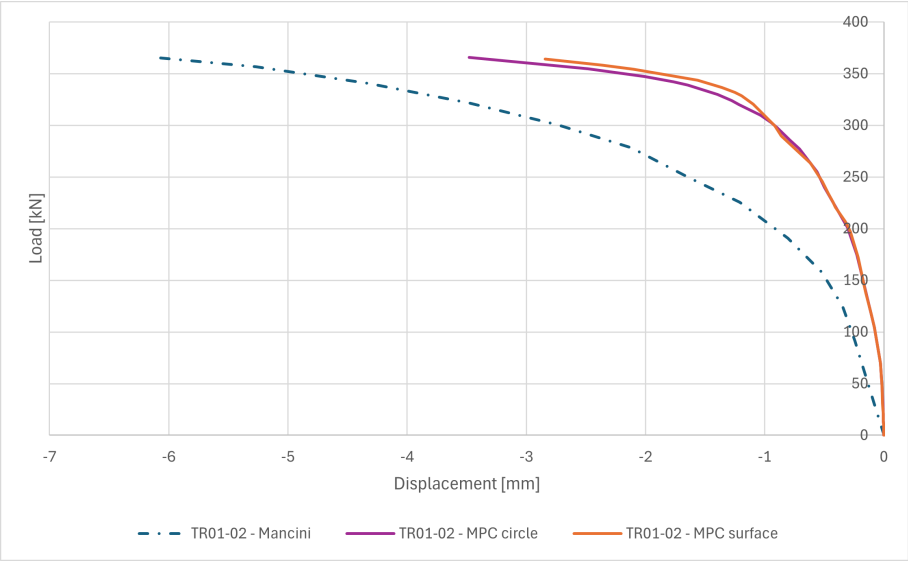

Figure 5.20: TR01-02: load-displacement curve for $\varphi = 0°$

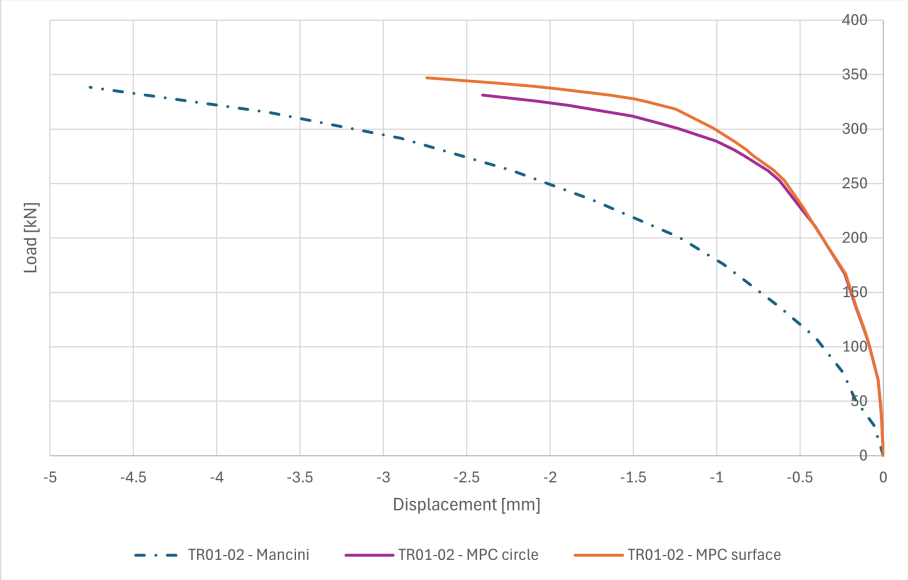

Figure 5.21: TR01-02: load-displacement curve for $\varphi = 15°$

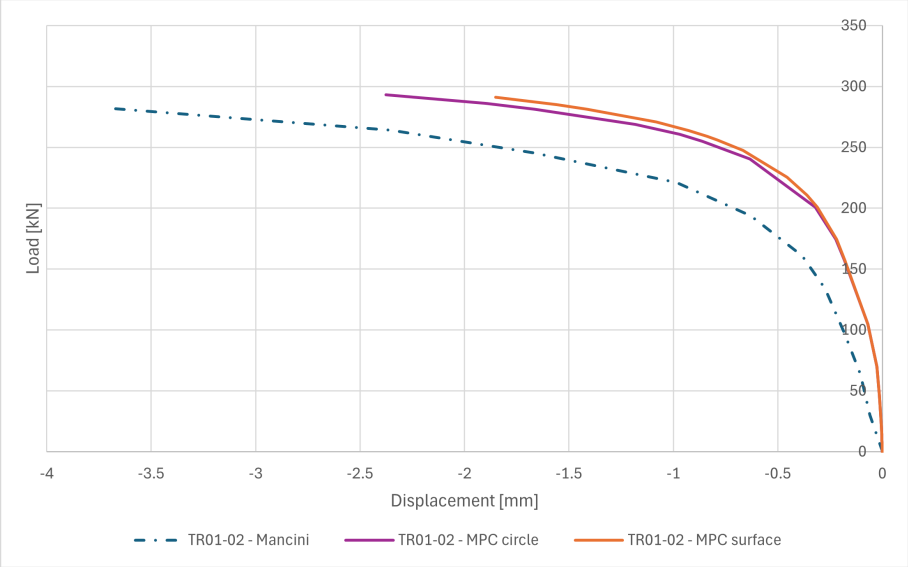

Figure 5.22: TR01-02: load-displacement curve for $\varphi = 45°$

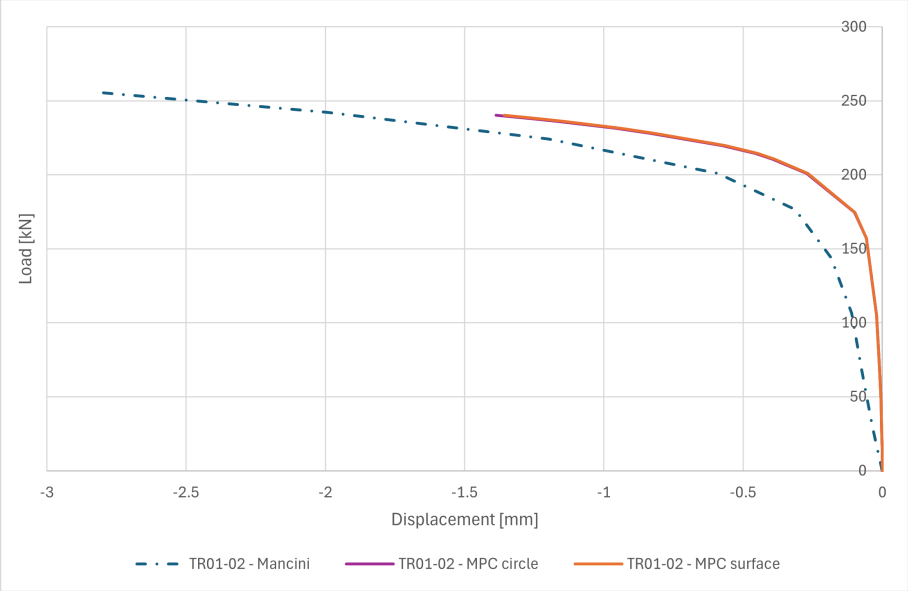

Figure 5.23: TR01-02: Load-displacement curve for $\varphi = 75°$

Note: TR01-02 load-displacement curves for $\varphi = 30°$ and $60°$ are available in Appendix A2.4.

Analysis of TR01-02 displacements

As observed with transducers TR13 and TR14 in the previous Section, variations in the applied constraint (*MPC surface* vs. *MPC circle*) affect the measured response. However, the difference between constraint types is less pronounced for TR01-02 results.

For small inclination angles, the *MPC circle* constraint allows for larger displacements beyond a certain load threshold compared to the *MPC surface* constraint. This difference between the results obtained with each constraint diminishes for inclination angles above 45° and becomes negligible at 75°, as lateral displacement decreases with the reduction of the shear force component.

In general, the results show a stiffer response across all angles. The greater the applied shear force, the larger the discrepancy between the current simulations and Mancini's experimental data. As discussed previously for pure tension simulations, the presence of bolt threading significantly influences the results. Specifically, two interactions are relevant:

- The interaction between the threads of the bolt and nut, which affects the force transfer mechanism.
- The contact between the bolt threads and the internal surfaces of the flange and foundation holes, particularly under shear loading.

These factors may partially explain the differences observed between Mancini's experimental and numerical results. As illustrated in Figure 5.18, the experimental results exhibit higher displacements than those obtained in Mancini's numerical simulations, indicating that the omission of bolt threads in the numerical model affects the accuracy of the response.

In addition, the differences between Mancini's results and the present study may also come from uncertainties in material and contact interaction parameters. Unlike the present work, Mancini had access to detailed experimental data regarding aspects such as penetration tolerances and the varying hardness of contact surfaces, which were incorporated into the model and could have influenced the results.

5.3 Analysis of the impact of the rotational constraint

In the previous Section, the results for two different constraint applications on the assembly were presented: the *MPC circle* and *MPC surface* constraints. The simulation results for various force inclination angles highlighted the influence of rotational restraint on the behaviour of the T-stub. These observations were consistently made using transducers 13 and 14, which measure displacement perpendicular to the foundation. While the global response of the assembly was captured, localised behaviours around the constraint regions were not explicitly represented. In fact, when forces are applied, the manner in which constraints are implemented at the pins leads to different load distributions, thereby inducing distinct local behaviours in the pins.

At the global scale, the difference in the response of the assembly is mainly attributed to how the rotational restraint either permits or restricts rotation. This constraint, applied locally at the pin holes, affects the surrounding material behaviour in different ways.

This constraint produces different levels of rotational freedom, observable in the deformed configurations of the T-stub. Specifically, when the *MPC circle* constraint is used, the regions defined by the circular MPC deform significantly more than the other parts of the pin holes. Moreover, the relative deformation of each circle compared to its corresponding hole varies across the three holes, indicating that they do not behave uniformly and are subjected to different force distributions. This variation depends on the force inclination angle and the overall assembly behaviour, which involves the interaction of multiple connected components.

In contrast, when the *MPC surface* constraint is applied, the entire hole surface is uniformly constrained, leading to more consistent local behaviour across the pin holes.

The deformations around the holes, represented at ultimate load, for force inclinations of $\varphi = 0°$, $\varphi = 45°$ and $\varphi = 90°$, are shown in Figures 5.24, 5.25, and 5.26 respectively.

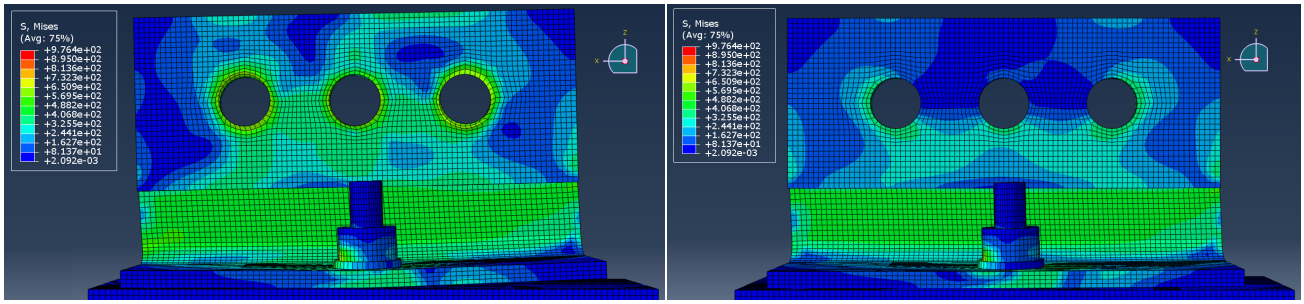

(a) *MPC circle* (b) *MPC surface*

Figure 5.24: Stress distribution in the model at ultimate load for different MPC constraints, with $\varphi = 0°$ (pure shear)

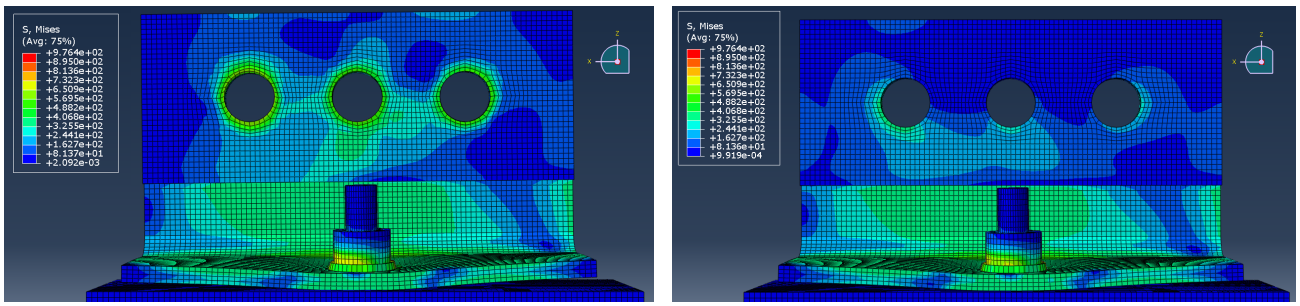

(a) *MPC circle* (b) *MPC surface*

Figure 5.25: Stress distribution in the model at ultimate load for different MPC constraints, with $\varphi = 45°$

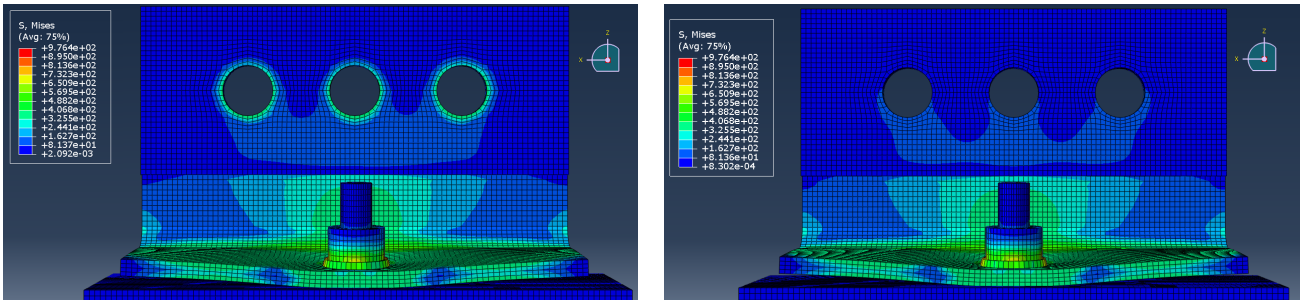

(a) *MPC circle* (b) *MPC surface*

Figure 5.26: Stress distribution in the model at ultimate load for different MPC constraints, with $\varphi = 90°$ (pure tension)

Depending on the inclination angle, the shear component plays a significant role in the behaviour of the system. For simulations with $\varphi = 0°$ and $\varphi = 45°$, different lever arms associated with each hole lead to unequal force distributions. Additionally, due to the interaction between the T-stub and the foundation, contact on one side and detachment on the other create further asymmetries. These effects are visible in the displacement patterns: for instance, the left hole may restrain downward movement (towards the foundation), whereas the right hole may restrain upward detachment. These behaviours are especially evident at lower inclination angles.

Another important observation is the behaviour of the web. Even though the stress distributions near the holes differ significantly between the *MPC circle* and *MPC surface* simulations, the stress pattern in the lower portion of the web – unreinforced by the welded plate – is largely unaffected. A back view of the model further supports this observation for an inclination of $\varphi = 45°$, as shown in Figure 5.27.

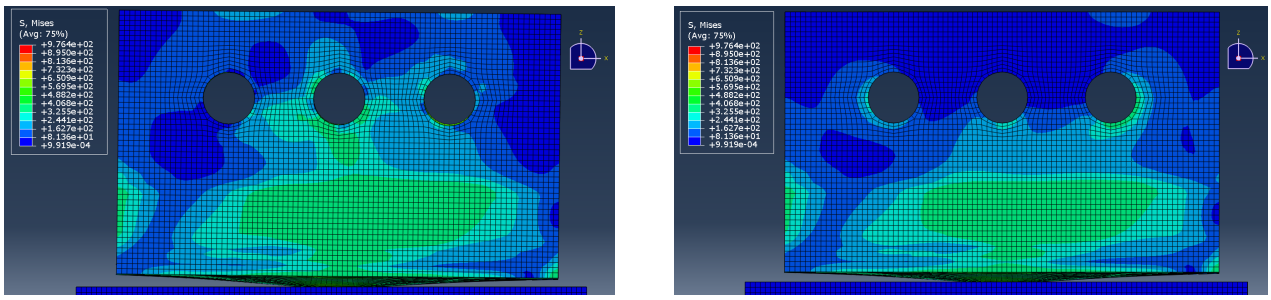

(a) *MPC circle* - back view (b) *MPC surface* - back view

Figure 5.27: Stress distribution in the model at ultimate load for different MPC constraints, with $\varphi = 45°$ (back view)

The vertical displacements measured in the Z direction at the flange extremities along the web axis indicate that the model with the *MPC circle* constraint allows a greater rotation of the web compared to the *MPC surface* case. This difference in vertical displacement is illustrated in Figure 5.28 for a representative force inclination angle of $\varphi = 45°$, comparing the deformation patterns for the two constraint types applied at the bolt holes. Additional examples for inclination angles $\varphi = 0°$, $\varphi = 15°$, $30°$, and $75°$ are provided in Appendix A3. These results support the earlier discussion regarding rotational constraint effects and are consistent with the load-displacement trends presented in Section 5.2.2.

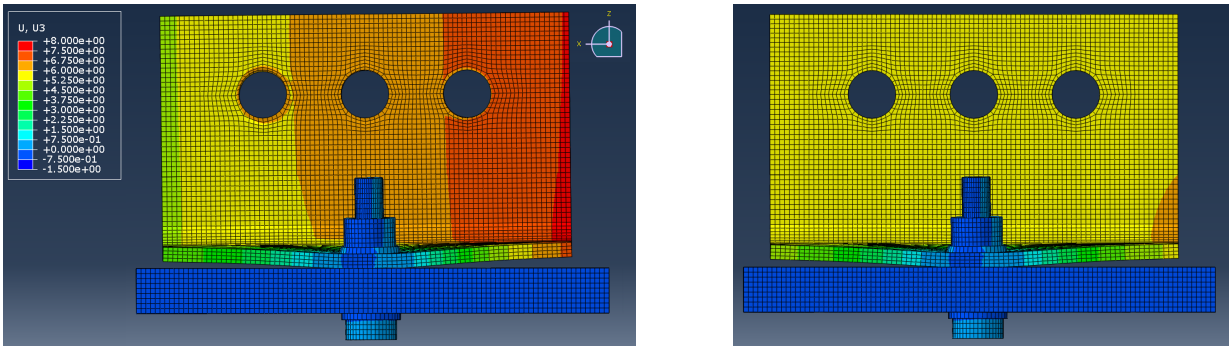

(a) *MPC circle* (b) *MPC surface*

Figure 5.28: Vertical displacement (Z) distribution of the assembly for $\varphi = 45°$ at ultimate load, comparing the effects of the *MPC circle* and *MPC surface* constraints.

Note: The legend is illustrated in Figure 5.28a and is consistent for the other Figure 5.28b represented

A further analysis examines the PEMAG intensity distribution around the holes, used to compare plastic strain magnitudes between the two constraint applications. Simulations with pure shear loading ($\varphi = 0°$) are presented in Figure 5.29, since they show the most pronounced deformations at the circles.

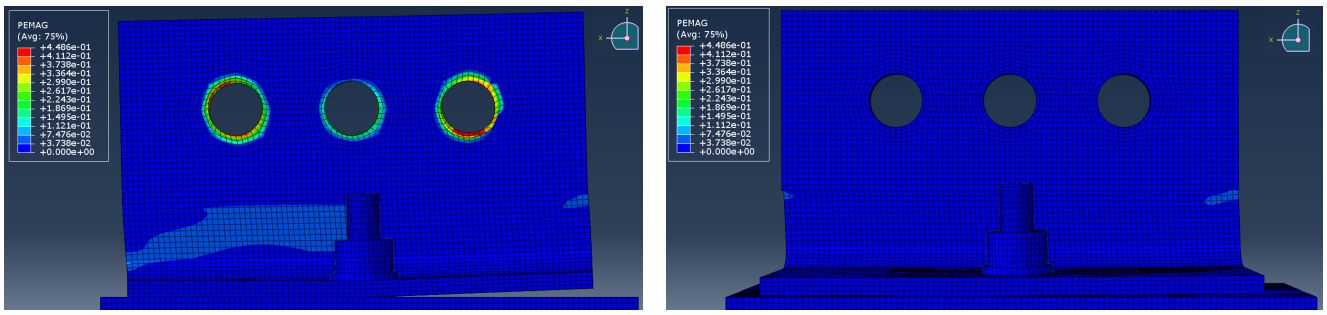

(a) *MPC circle* - PEMAG (b) *MPC surface* - PEMAG

Figure 5.29: PEMAG distribution for different MPC constraints at ultimate load for $\varphi = 0°$

Although the figures illustrate the deformed configurations at the ultimate load, the onset of plasticity is observed much earlier in the simulations using the *MPC circle* constraint. In contrast, the model employing the *MPC surface* constraint does not exhibit any plastic response in the web, as the force required to induce plastic strains uniformly across the entire hole surface is significantly higher.

It is important to note that neither of these constraint configurations accurately reflects the physical conditions of the experimental setup. The *MPC circle* constraint does not realistically represent the contact between the pins and the inner surfaces of the holes, as it enforces displacement over idealised circular boundaries rather than true contact interfaces. Similarly, the *MPC surface* constraint imposes force transmission over the full internal surface of the holes, which is also not physically representative. In practice, the pins are not in continuous contact with the entire hole surface; instead, contact occurs only over limited regions.

These actual contact areas are determined by the initial load inclination at the beginning of the test and evolve with the deformation of the hole, leading to localised stress concentrations. Consequently, modelling the applied forces as uniformly distributed across either circles or surfaces fails to capture the real mechanical interaction between the pins and the T-stub holes. A more accurate representation would require explicitly modelling the pins as solid components in the assembly, thereby allowing the contact interactions and potential detachment zones to develop naturally as a function of load orientation and local deformation.

5.4 Model with three pins

In the actual experimental setup, the pins do not remain in full contact with the inner surfaces of the holes. Depending on the orientation of the applied forces, detachment may occur in specific regions while contact is maintained elsewhere. This behaviour is not adequately captured by either of the current constraint configurations, as both *MPC circle* and *MPC surface* enforce a fully bonded interaction over idealised areas. Consequently, these simplified assumptions can lead to unrealistic distributions of stress and plasticity, particularly in regions where physical contact would not occur.

To more accurately replicate the mechanical behaviour observed in experiments, the most reliable approach is to explicitly model the three pins as separate components within the simulation. This enables the use of contact interactions capable of capturing both the localisation of force transmission and the potential for detachment between the pins and the hole surfaces. Such a setup would allow the contact zones to evolve naturally with the deformation of the assembly, in response to varying load inclinations and boundary conditions.

The modelling details are provided in Appendix A4.1. The key modification in this version is the explicit representation of the three pins, each with a diameter of 30 mm. The holes into which the pins are inserted are also defined with a 30 mm diameter. This choice reflects the lack of more specific information in the work of Mancini [3] and avoids introducing additional geometric variables that might obscure the influence of the contact modelling itself.

A critical aspect of this model is the implementation of constraints that link the pins to the rest of the assembly. An *MPC Tie* constraint is applied to connect the entire external surface of each pin to a reference point where the force is applied. This configuration makes the results of the three-pin model directly comparable to those obtained using the *MPC surface* approach, the main improvement being the possible local separation between the pins and the holes. For the purposes of analysis, this updated configuration is referred to as the "3-pin model".

Figure 5.30 shows the updated assembly in which the three pins are inserted into the holes of the web. The pin length exceeds the combined thickness of the web and the reinforcing welded plate to prevent edge effects or boundary-related artefacts during the simulation.

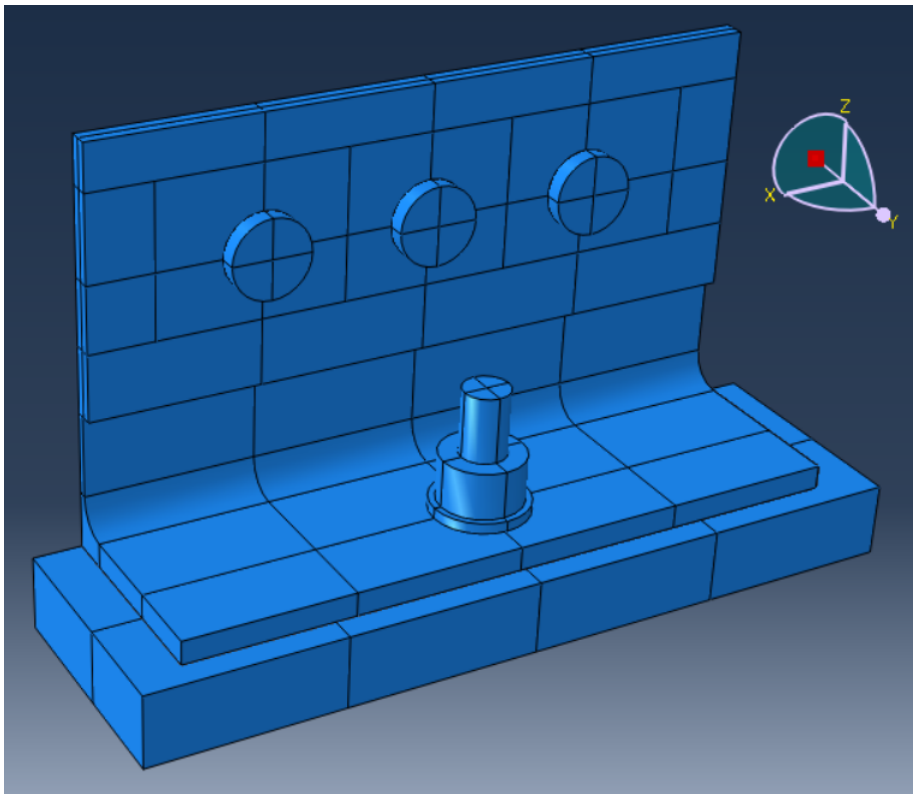

Figure 5.30: 3-pin model assembly

5.4.1 Results of the simulations

The results of the simulation for displacements recorded by transducers 13 and 14 at inclination angles $\varphi = 0°$, 15° and 30° are presented in Figures 5.31 to 5.33. Additional results for inclination angles of 45° and 90° are included in Appendix A4.2, as the observed differences with respect to the *MPC surface* model are less pronounced at these higher angles.

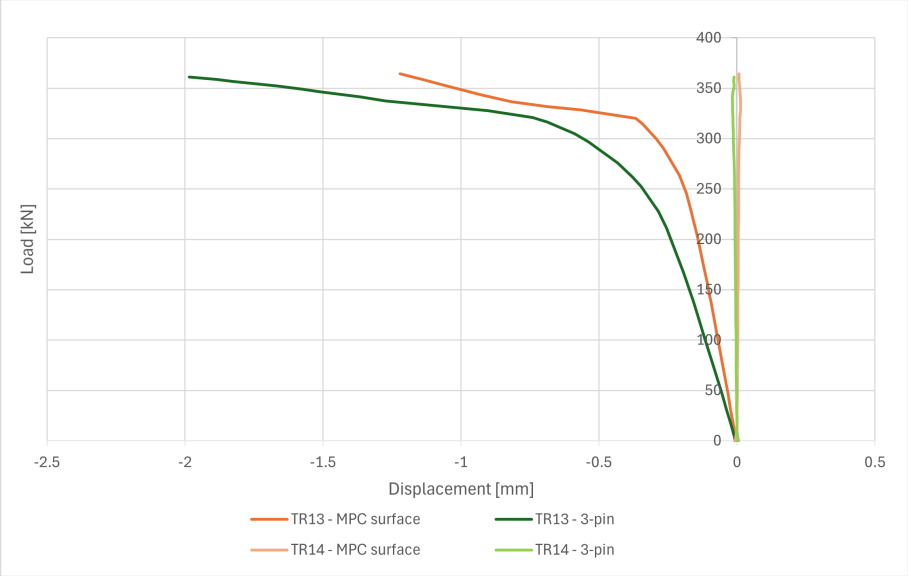

Figure 5.31: TR13-14 load-displacement curve for inclination $\varphi = 0°$ (3-pin)

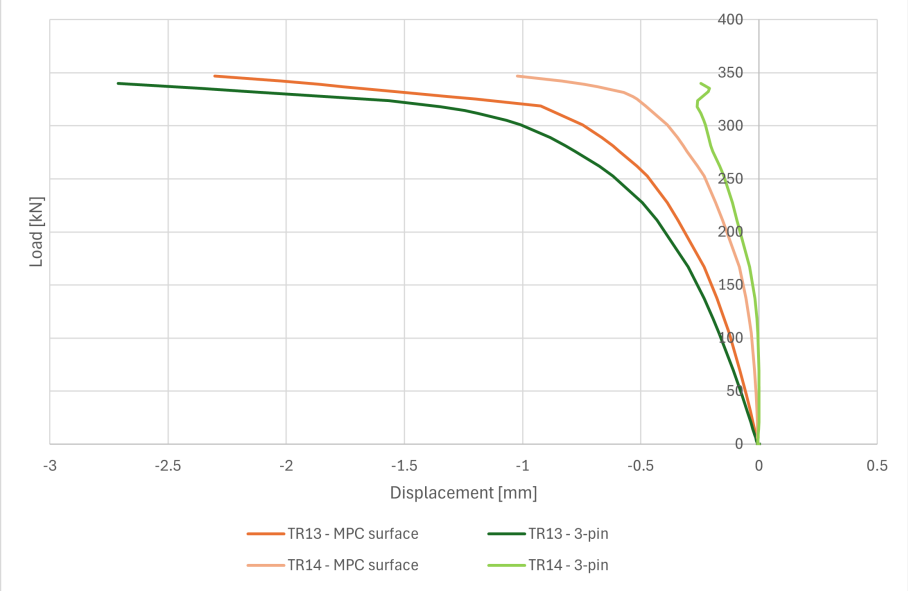

Figure 5.32: TR13-14 load displacement curve for inclination $\varphi = 15°$ (3-pin)

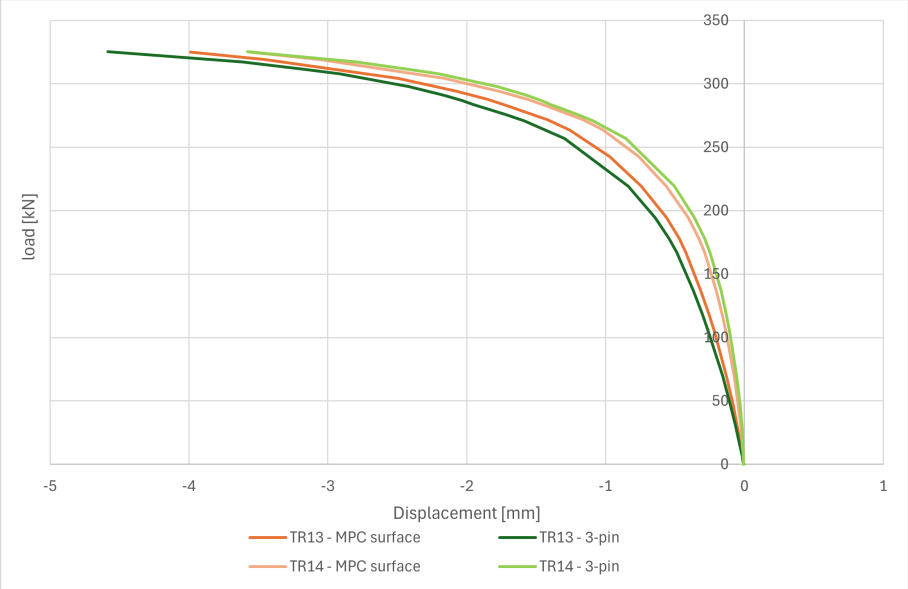

Figure 5.33: TR13-14 load displacement curve for inclination $\varphi = 30°$ (3-pin)

5.4.2 Discussion of the results

The inclusion of the three pins in the model slightly alters the displacements recorded by transducers 13 and 14:

- **Angle $\varphi = 0°$**
  For transducer 13, the measured displacement is significantly higher than in the *MPC surface* model. This indicates a reduction in rotational restraint, leading to a delayed onset of the plastic deformation and a larger displacement, suggesting increased deformations due to rotation of the assembly. The transducer 14 is not impacted and stays is contact with the foundation.

- **Angle $\varphi = 15°$**
  Transducer 14 records a lower displacement, while transducer 13 records a higher one, again pointing to greater rotational deformation. As illustrated in Figure 5.34, which compares all three configurations (*MPC circle*, *MPC surface*, and the 3-pin model), the behaviour of the 3-pin model lies between that of the two simplified constraint models.

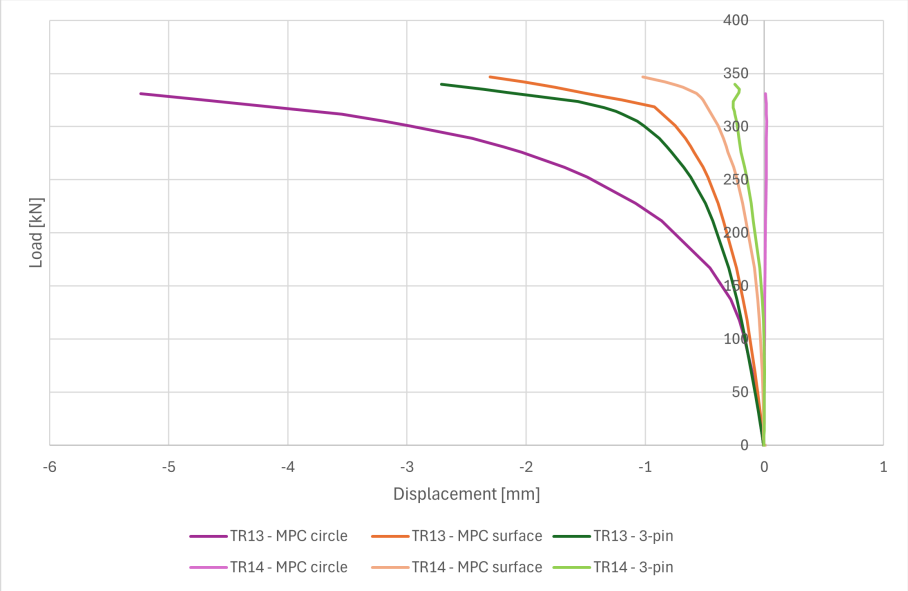

Figure 5.34: TR13-14 load-displacement curve for inclination $\varphi = 15°$ (*MPC surface*, *MPC circle* and 3-pin)

- **Angle $\varphi \geq 30°$**
  From an inclination of 30° upwards, the differences between the models become less significant.

5.4.3 Deformations of the holes

At the ultimate load, localized detachments between the pins and the internal surfaces of the holes are observed, indicating partial contact conditions and resulting in stress concentrations. Specifically:

- In the left hole (Figure 5.35a), a detachment is visible along the lower surface.
- In the right hole (Figure 5.35b), a detachment occurs along the upper internal surface.

These separation zones – highlighted by red crescent markers in Figures 5.35 and 5.36 – tend to decrease in size as the inclination angle of the applied force on the model increases. The middle hole exhibits smaller detachment areas compared to the outer holes, as illustrated in Figure 5.36.

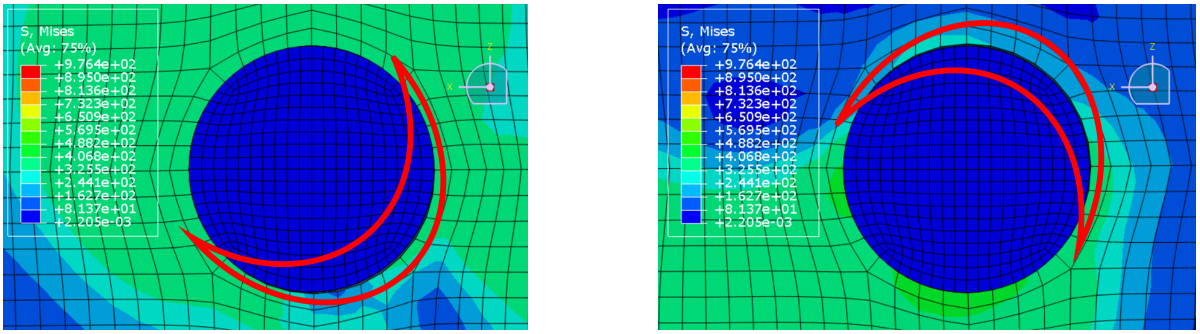

(a) left hole (b) right hole

Figure 5.35: Stress detail around left and right holes for 3-pin model under $\varphi = 0°$ at ultimate load

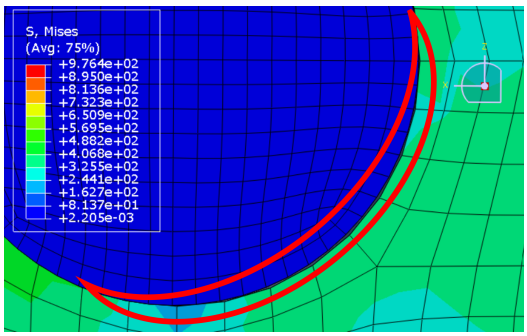

Figure 5.36: Stress detail around middle hole for 3-pin model under $\varphi = 0°$ at ultimate load

Furthermore, the CPRESS output – representing the contact stress perpendicular to the interface – is shown in Figures 5.37 and 5.38. These results confirm the presence of localized contact stress concentrations on specific sides of the pins, aligned with the previously noted detachment areas. The absence of significant CPRESS values over large surface regions indicates that no effective contact is maintained in those zones, further supporting the observed detachment between the pin and hole surfaces.

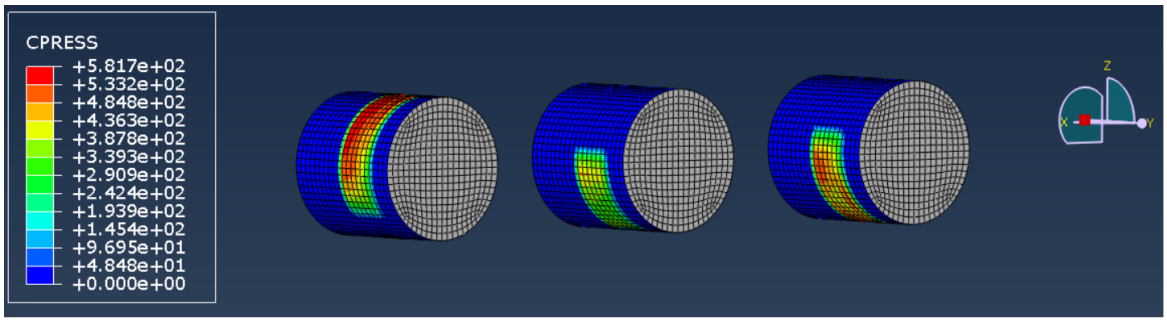

Figure 5.37: CPRESS stress on the pins - left view

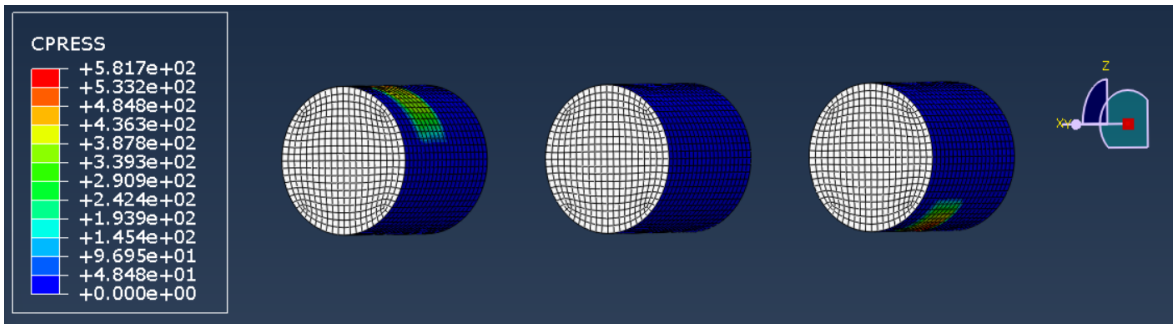

Figure 5.38: CPRESS stress on the pins - right view

5.4.4 Results of the 3-pin model

The results obtained using the 3-pin model highlight the complexity of accurately reproducing physical interactions through numerical modelling. Each assumption made in the digital representation of the experimental setup has a significant impact on the simulation outcomes. The interaction between multiple components, each with distinct properties, introduces numerous interdependent parameters, making the simulation results highly sensitive to modelling choices.

5.5 Bolt stress analysis

The inclination of the force applied to the T-stub significantly influences the behaviour of the assembly, as shown in Figure 2.9 in Mancini's results and in Figures 5.15 and 5.16. The displacement of the flange edge points along the web axis is affected, but the critical aspect to investigate is whether the bolt – the most influential component in the assembly – is subjected to different stress states. In Section 5.1, a non-uniform stress distribution was highlighted under pure tensile loading. Additionally, the method for imposing rotational constraints was discussed in Section 5.2 and a more complex model with three pins was discussed in Section 5.4. The present analysis focused on bolt stresses for combined axial and shear loading of varying magnitudes applied on the T-stub, the **MPC surface** constraint is applied.
As will be further demonstrated in this section, simulations using the *MPC circle* constraint yield results nearly identical to those obtained with the *MPC surface* constraint. For this reason, only the *MPC surface* configuration is discussed in detail, while results for the *MPC circle* configuration are provided in Appendix A5 as supporting evidence. Similarly, the 3-pin model exhibits an intermediate displacement behaviour compared to the two constraint approaches and is therefore expected to lead to the same conclusions. Consequently, it is not further analysed in the following sections.

For reference, the orientation of the inclined resultant force applied in the model is illustrated in Figure 3.9. In the numerical simulation, this force is decomposed into two components: an axial component (oriented along the positive Z-axis) and a shear component (oriented along the positive X-axis), as previously depicted in Figure 4.20a.

5.5.1 Stress distribution in the bolt cross-section

Varying the inclination angle of the applied force induces a transitional behaviour in the structural response of the assembly. This effect is especially pronounced in the bolt, which experiences complex loading conditions. Even when a purely tensile force is applied to the T-stub, the bolt is not subjected to pure axial tension but instead undergoes a combination of stresses due to local deformations and interaction effects within the connection.

Initially, the bolt is analysed at the simulation step corresponding to the **onset of plastic deformation** in the bolt itself. According to the simulation results, this threshold consistently occurs around 933 MPa.

Figure 5.39 illustrates the global view of the assembly used to analyse the subsequent stress plots shown in Figure 5.40.

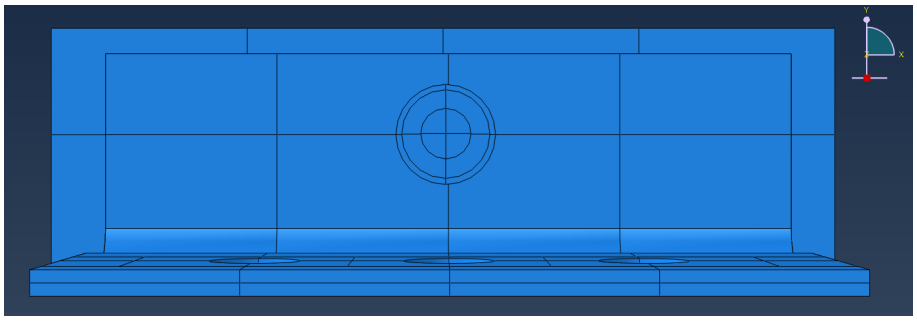

Figure 5.39: General view of the T-stub for bolt analysis

The analysis is conducted at a specific height in the bolt shank to examine the stress distribution across a cross-section. The chosen section – cutting layer 3 – is illustrated in Figure 5.41. This section corresponds to the region exhibiting the highest stress values in the bolt shank. It is also located within the middle of the threaded portion of the bolt, which is 6 mm high and partially embedded within the washer thickness.

In Figure 5.40, the von Mises stress distributions are presented for this cutting layer, for different inclination angles of the applied force. A legend is included for each case, as the stress ranges exhibit slight variations. The analysed angles range from predominantly shear to predominantly axial loading: 0°, 15°, 30°, 45°, 60°, 75° and 90°. The axis orientation is shown in Figure 5.40a and remains consistent across all Figures.

It is evident that the inclination angle of the applied force strongly affects the stress distribution within the bolt cross-section at the onset of plastic deformation.

For predominantly axial loads ($\varphi = 75°$ and 90°), the stress distributions in the bolt show similar profiles, primarily characterized by axial tension (from both preloading and T-stub traction) combined with bending. The stress magnitudes remain consistent across the inclination force angle cases, as the analysis is conducted near the onset of plastic deformation. As the shear component increases (i.e. for lower inclination angles), the orientation of the stress field gradually rotates with respect to the pure tension case. This rotation becomes increasingly pronounced, ultimately reaching nearly 90° between the two extreme loading configurations. Specifically, for $\varphi = 90°$, where a purely tensile force is applied to the T-stub, the bolt undergoes tension and bending. In contrast, for $\varphi = 0°$, corresponding to pure shear loading, the bolt is subjected to shear and bending.

In conclusion, the inclination of the applied force significantly influences the orientation of the von Mises stress distribution in the threaded portion of the bolt. While the stress magnitudes and overall profile shapes are comparable, their orientation varies with the force inclination angle.

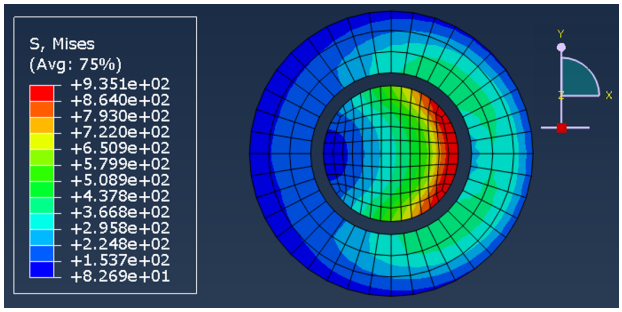

(a) $\varphi = 0°$

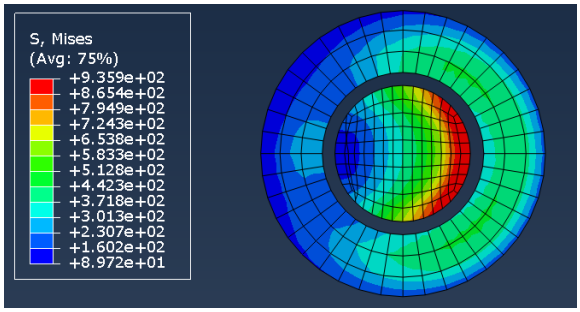

(b) $\varphi = 15°$

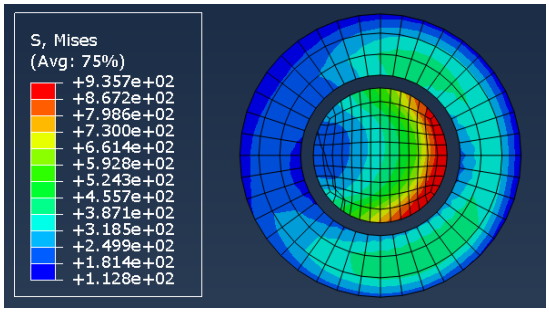

(c) $\varphi = 30°$

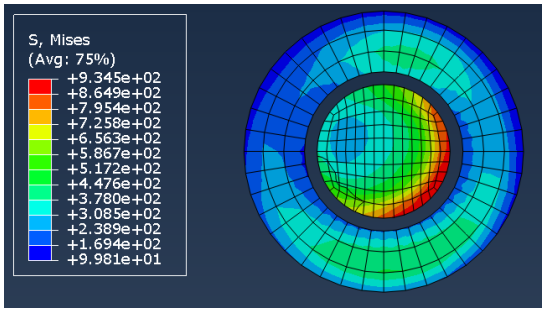

(d) $\varphi = 45°$

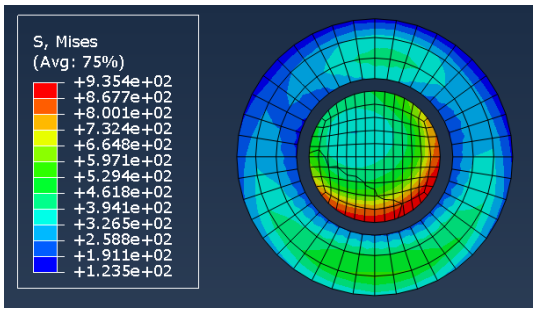

(e) $\varphi = 60°$

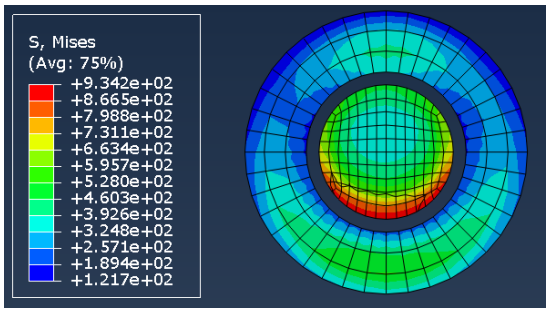

(f) $\varphi = 75°$

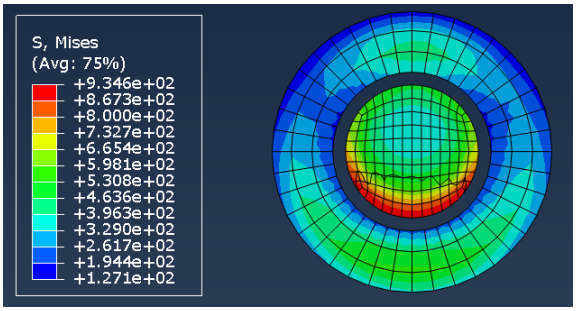

(g) $\varphi = 90°$

Figure 5.40: Cutting layer 3 of bolt for different force inclinations, at bolt yielding

5.5.2 Stress distribution along the bolt shank

At the **ultimate load**, the stress distribution along the bolt shank exhibits significant variations depending on the inclination angle of the applied force. Regions experiencing maximum stress (up to 976.4 MPa) shift along the bolt axis as the load angle changes.

This analysis focuses on simulations performed with the **MPC surface** constraint at ultimate load. The stress distribution is evaluated at three distinct cross-sections along the bolt height, as illustrated in Figure 5.41:

- Cutting layer 1: located in the unthreaded shank region,
- Cutting layer 2: situated at the upper boundary of the foundation, a region potentially affected by lateral compressive forces due to contact,
- Cutting layer 3: positioned in the middle of the threaded portion, coinciding with the section used previously to assess plasticity onset.

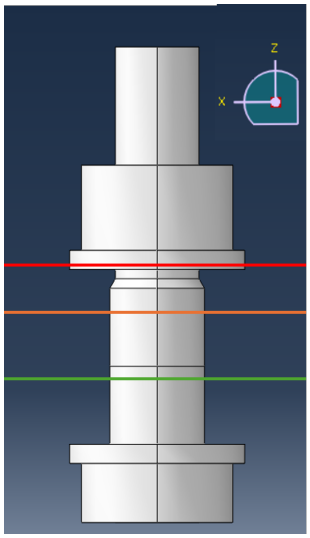

Figure 5.41: Cutting planes along the bolt height

A global view of the assembly used to orient this analysis is presented in Figure 5.39. As previously stated the applied force lies in the XZ plane, with the shear component acting in the positive X-direction and the axial component in the positive Z-direction.

Stress distributions at cutting layers

Figures 5.42 to 5.44 present the stress distributions at the three cutting layers for inclination angles of 0°, 45° and 90° respectively.

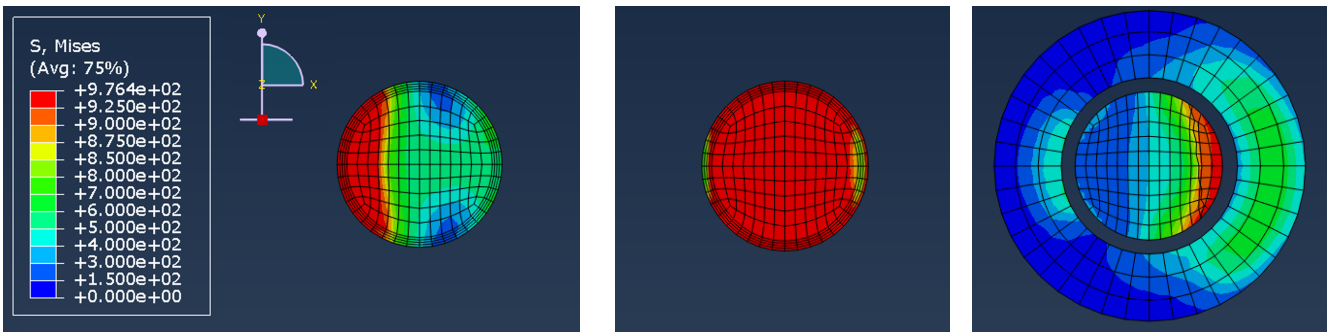

(a) Cutting layer 1 (b) Cutting layer 2 (c) Cutting layer 3

Figure 5.42: Stress distribution at $\varphi = 0°$ and ultimate load

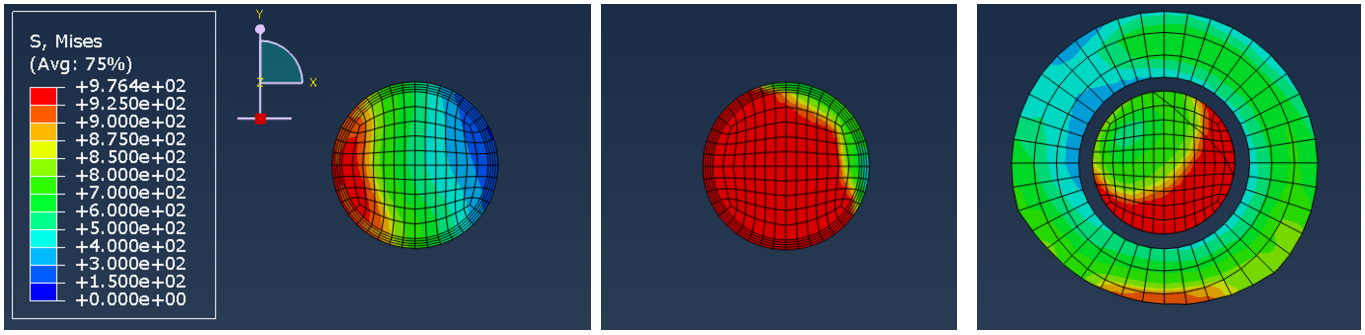

(a) Cutting layer 1 (b) Cutting layer 2 (c) Cutting layer 3

Figure 5.43: Stress distribution at $\varphi = 45°$ and ultimate load

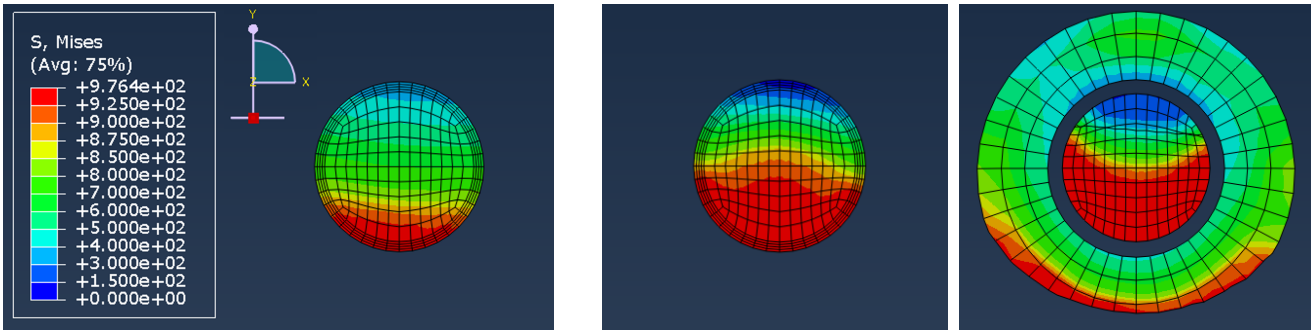

(a) Cutting layer 1 (b) Cutting layer 2 (c) Cutting layer 3

Figure 5.44: Stress distribution at $\varphi = 90°$ and ultimate load

Several observations can be drawn from these Figures.

- Under a force inclination of $\varphi = 90°$, as shown in Figure 5.44, the bolt is primarily subjected to axial tension and bending. The stress distribution exhibits a consistent orientation across the three cutting planes, indicating uniform loading along the bolt axis.
- In contrast, under a force inclination of $\varphi = 0°$, illustrated in Figure 5.42, the bolt is subjected to a combination of tension, shear, and also compressive stresses arising from contact interactions. In cutting layer 3, maximum stresses are observed on the right side of the bolt, corresponding to contact with the T-stub flange. In cutting layer 1, the maximum occurs on the left side, due to contact with the foundation. This stress distribution is further confirmed by the side view shown in Figure 5.46b.

The rotation of the web, governed by the constraints applied to the pin holes, could potentially influence the stress distribution along the bolt axis. To assess this, the same analysis was repeated using the *MPC circle* constraint. The corresponding results, presented in Appendix A5, show no significant deviations compared to those obtained with the *MPC surface* constraint.

If the rotational boundary condition had a strong influence, substantial differences would be expected between the two sets of results. However, the stress distributions remain nearly identical across all examined cutting planes. Only minor variations in magnitude – particularly in cutting layer 1 and cutting layer 3 – are observed, while the overall shape of the profiles remains consistent.

This comparison confirms that the choice of rotational constraint (whether *MPC surface* or *MPC circle*) has a negligible effect on the stress distribution along the bolt axis.

Side and back views of the bolt

Note: The applied force lies in the XZ plane, with the shear component acting in the positive X-direction and the axial component in the positive Z-direction.

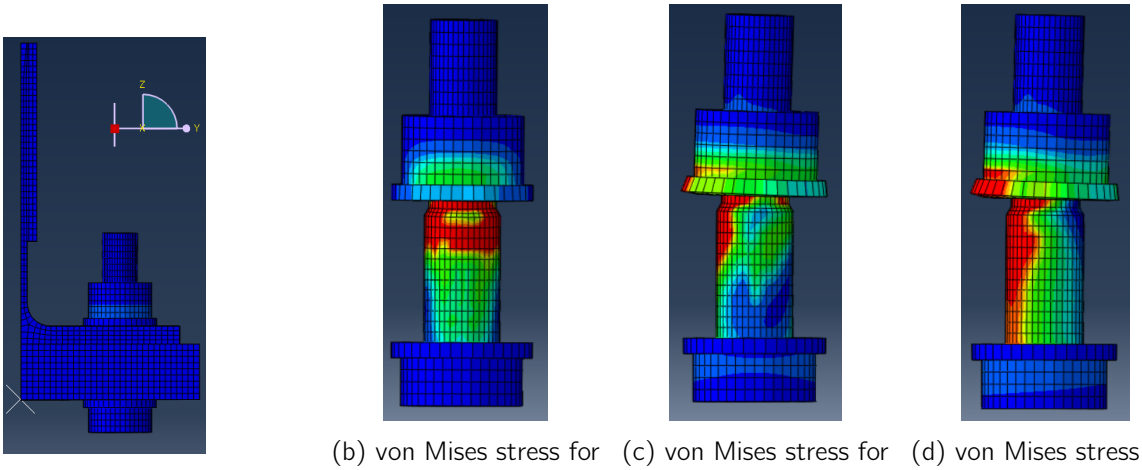

(a) Reference side view (b) von Mises stress for $\varphi = 0°$ (c) von Mises stress for $\varphi = 45°$ (d) von Mises stress for $\varphi = 90°$

Figure 5.45: von Mises stress for side view of the bolt at ultimate load for different inclination angles

Note: The legend is consistent with Figures 5.44.

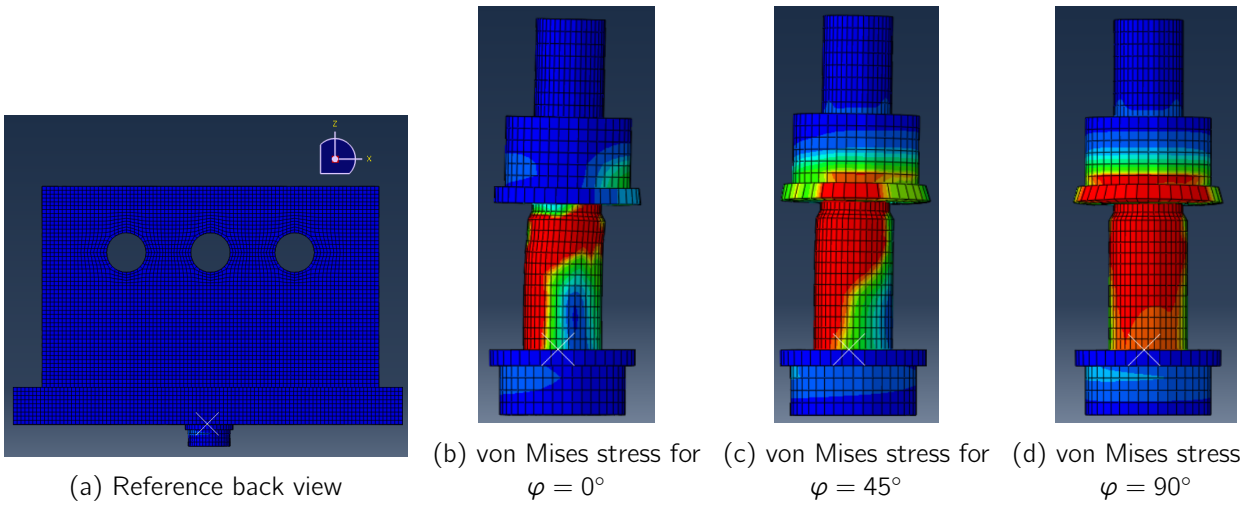

(a) Reference back view (b) von Mises stress for $\varphi = 0°$ (c) von Mises stress for $\varphi = 45°$ (d) von Mises stress for $\varphi = 90°$

Figure 5.46: von Mises stress for back view of the bolt at ultimate load for different inclination angles

Note: The legend is consistent with Figures 5.44.

5.5.3 Discussion of the results

The results reveal a significant influence of the force inclination angle on the internal stress distribution within the bolt. Stress fields differ markedly between pure axial and pure shear T-stub loading conditions, reflecting distinct load transfer mechanisms. At $\varphi = 45°$, the stress profiles are not a simple combination of pure shear and axial cases. Instead, they reflect complex interactions due to the orientation and magnitude of the combined loading. The observed deformed shapes of the bolt further confirm the presence of bending moments. Side views, illustrated in Figure 5.45, indicate bending about the X-axis (M_x), attributed to the lever arm between the axial load path in the web and the bolt axis – quantified as the m parameter in analytical models – and also depending on the stiffness of the T-stub flange. Back views also suggest that interaction between the flange and bolt surfaces in the deformed configuration could contribute to the development of bending around the Y-axis (M_y). Specifically, differential deformation of the flange on either side of the bolt may induce asymmetrical contact forces, particularly at the interface between the bolt washer and the flange surface.

These findings align with the discussion in Section 5.6, regarding the role of moment effects in T-stub models subjected to combined axial and shear loads.

5.6 Influence of Moments

As presented in the previous Section, the analysis of bolt stress under various load inclinations at the ultimate load reveals deformed configurations that suggest the presence of bending moments acting on the bolt. Specifically, the lever arm between the axial load path in the web and the bolt axis may generate a bending moment around the X-axis (M_x), while the shear load could introduce a bending moment around the Y-axis (M_y).

Different force inclinations on the assembly result in varying proportions of axial and shear forces, which may produce a complex interaction between the two bending moments. To support these observations, the contact stresses between the model components are examined.

5.6.1 Contact stress in foundation hole and top surfaces

The von Mises stress distributions, shown in the left column of Figure 5.48, highlight localized stress zones whose orientation varies with the force inclination. These stress zones are typically concentrated on one side of the foundation hole, but von Mises stresses by themselves cannot distinguish whether their origin is due to axial or shear effects.

To clarify this, we consider the CPRESS stress output from Abaqus, which represents the magnitude of the contact stress perpendicular to the contact surface. These CPRESS distributions are displayed in the right column of Figure 5.48. For reference, the overall view of the assembly used to generate these results is shown in Figure 5.47a, and the zoomed region used in Figures 5.48 is illustrated in Figure 5.47b.

For consistency and clarity across all inclination angles, the CPRESS visualization range in the software was fixed arbitrarily at a maximum value of 750 MPa. This value was chosen to maintain a uniform color scale across all figures.

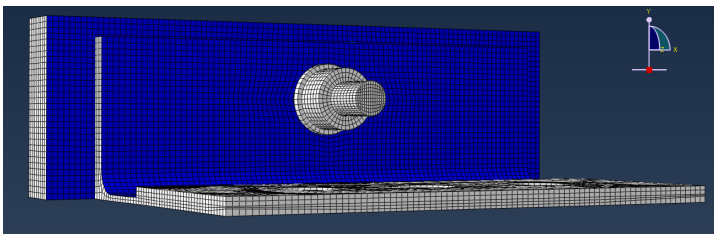

(a) General view on assembly

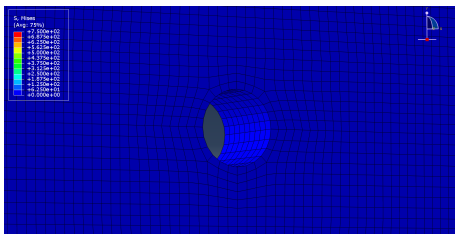

(b) Zoomed general view on assembly

Figure 5.47: General view on assembly

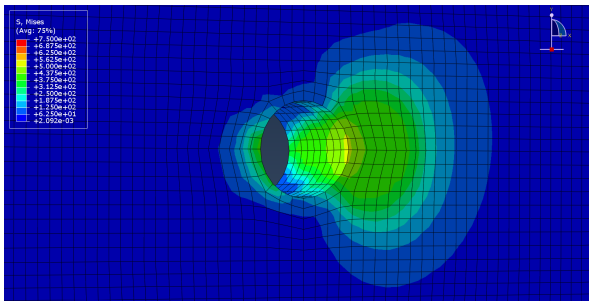

(a) von Mises stresses - $\varphi = 0°$

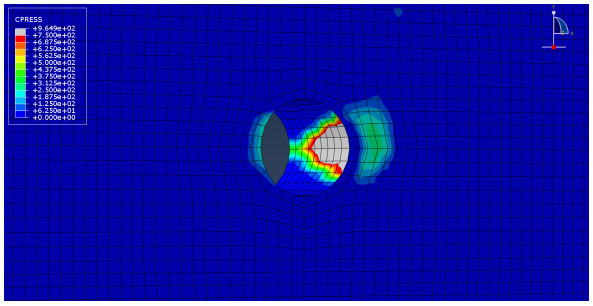

(b) CPRESS stresses - $\varphi = 0°$

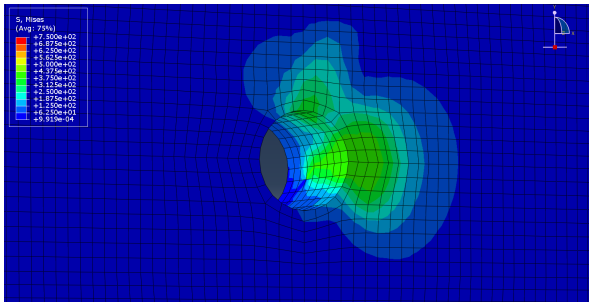

(c) von Mises stresses - $\varphi = 45°$

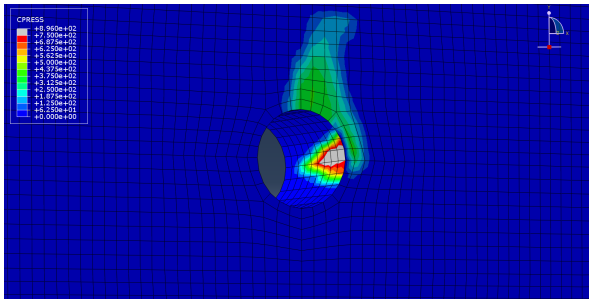

(d) CPRESS stresses - $\varphi = 45°$

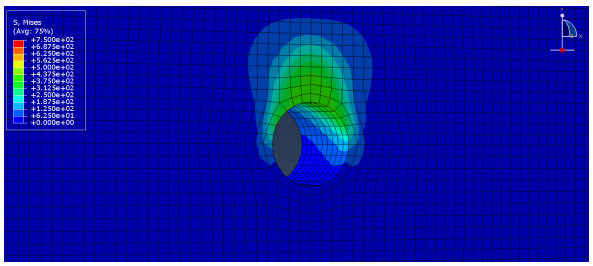

(e) von Mises stresses - $\varphi = 90°$

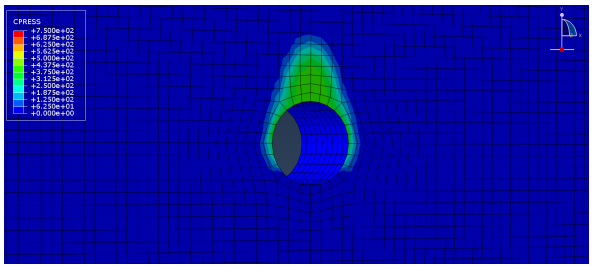

(f) CPRESS stresses - $\varphi = 90°$

Figure 5.48: von Mises and CPRESS stress distributions on the foundation (oriented view)

The influence of force inclination on CPRESS stress distribution can be summarized as follows:

- **Pure shear case ($\varphi = 0°$):**
  Almost no perpendicular contact stresses are observed on the top surface of the foundation, indicating limited axial contact between the flange and foundation. The von Mises stress in this zone is primarily due to shear. However, a localized contact point appears at the extreme corner of the foundation, as illustrated in Figure 5.49, where the end of the flange web (at the position of TR14) is in contact with the foundation. The foundation hole surface exhibits significant contact stress due to shear-induced bearing.

- **Pure axial case ($\varphi = 90°$):**
  The contact stress distribution is symmetric with respect to the Y-axis, representing prying force effects between the flange and the foundation. No contact is observed on the inner surface of the foundation hole, as shear is absent.

- **Intermediate case ($\varphi = 45°$):**
  The CPRESS distribution reveals a transitional state between the two extremes. A noticeable contact zone is observed on the top surface of the foundation with an intermediate orientation. Contact stress in the hole surface is reduced compared to the pure shear case. As the inclination angle decreases from 45° to 0°, the contact on the top surface reduces, while the contact on the hole surface becomes more dominant.

These variations in CPRESS contact orientation and magnitude illustrate the interaction between axial and shear forces applied to the T-stub assembly. To determine whether the bolt is subject to bending, it is necessary to examine the asymmetry in the contact stresses between the washer and the top surface of the plate.

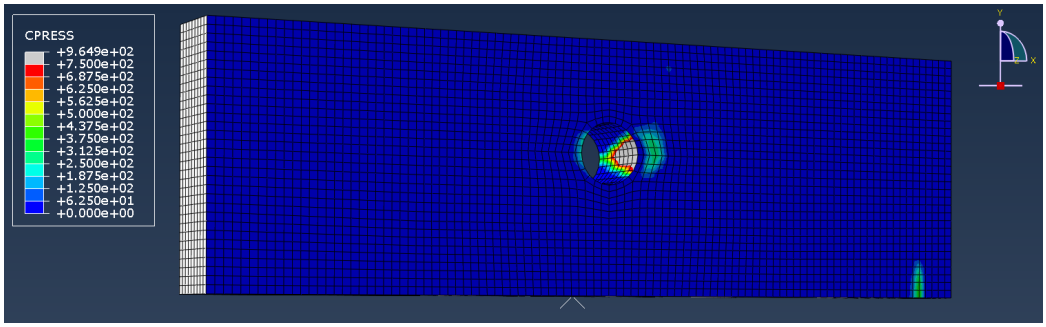

Figure 5.49: CPRESS stresses for $\varphi = 0°$ inclination angle

5.6.2 Contact stress on flange surface and bolt washer interface

The following illustrations present CPRESS values on the top surface of the flange, representing the perpendicular contact stress between the bottom surface of the bolt washer and the top surface of the flange. Figure 5.50 provides a global view of the isolated flange used for analyzing the subsequent figures.

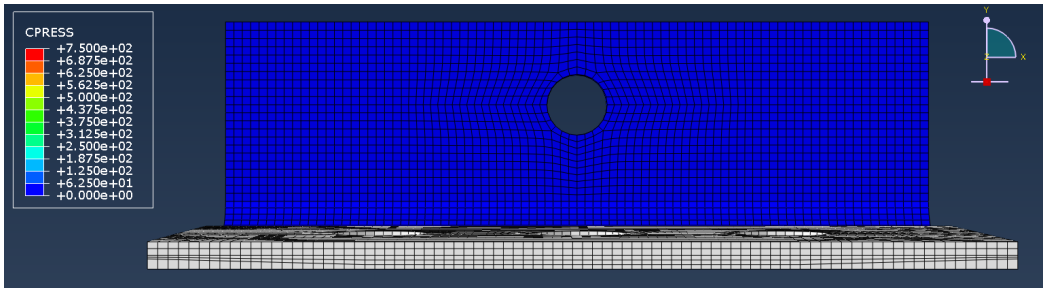

Figure 5.50: General view on flange

The CPRESS output is used to analyze the surface contact between the flange and the bolt washer. Only selected inclination angles are illustrated: 0°, 15°, 30°, 45°, and 90°. The focus is on the flange rather than on the bolt due to simpler visualization options in Abaqus.

Figure 5.51a shows the CPRESS stress distribution at the end of the bolt preloading step. This configuration is identical for all simulations, except for the pure tensile test, which exhibits a symmetric configuration due to a different experimental setup, as discussed in Section 2.1.1. The observed stress non-uniformity in Figure 5.51a results from the non-concentricity between the axes of the foundation, bolt and flange holes, as explained in Section 4.1.1. Initial surface contact was enforced in the simulation to prevent slippage at the beginning of loading.

Figure 5.51 displays the CPRESS distribution for different inclination angles, showing significant variation in the stress patterns on the flange surface.

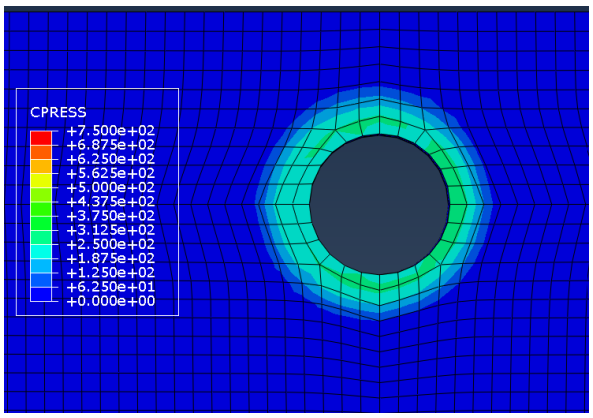

(a) CPRESS stresses - end of preloading step

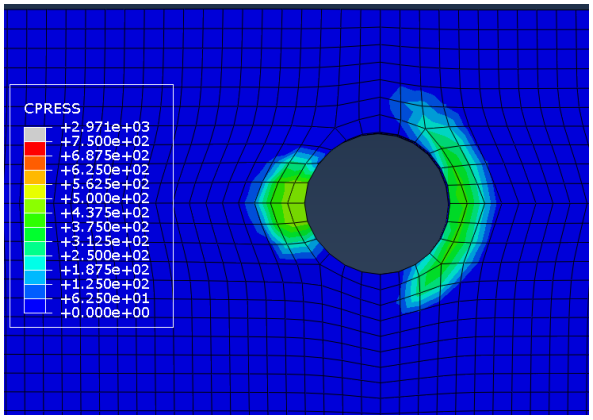

(b) Flange - $\varphi = 0°$

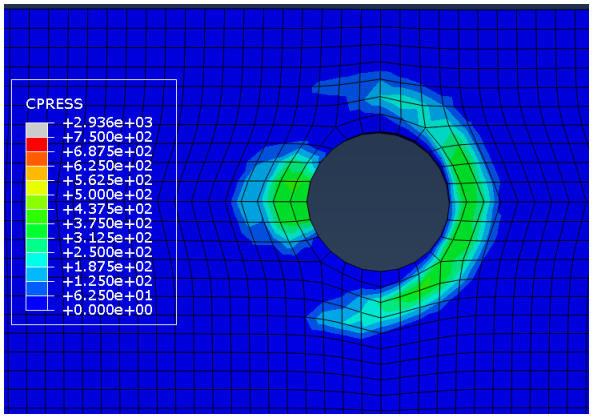

(c) Flange - $\varphi = 15°$

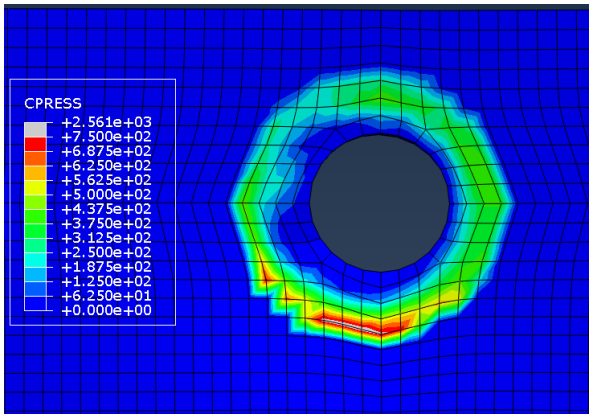

(d) Flange - $\varphi = 30°$

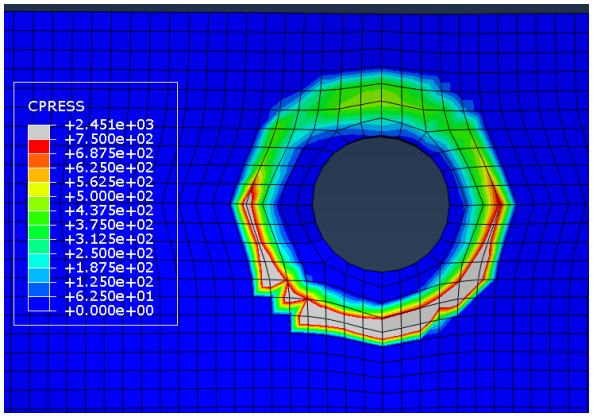

(e) Flange - $\varphi = 45°$

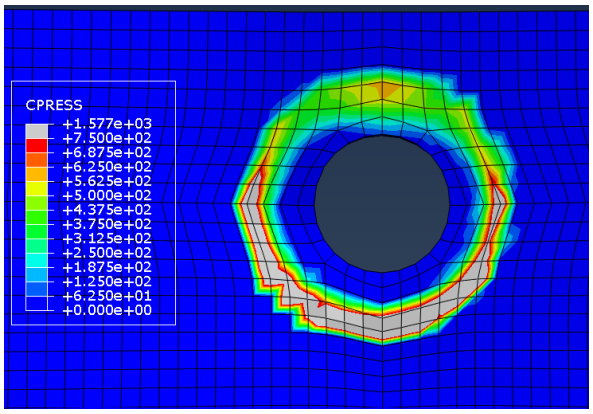

(f) Flange - $\varphi = 90°$

Figure 5.51: CPRESS stresses distribution on flange for different loading inclinations

Observations:

- **Effect of preloading:**
  The shear force is applied along the positive X-axis (as defined in Figure 4.18b, Section 4.1.5). However, in small inclination angles, contact stress remains visible on the negative X-side due to the initial bolt preloading. Without preloading, the contact area on the negative X-side would be significantly reduced.

- **Pure shear case ($\varphi = 0°$):**
  The primary load transfer occurs at the flange hole due to contact with the bolt shank. Nevertheless, a stress zone also develops at the interface between the washer and flange. This contact is asymmetric with respect to the Y-axis. The resulting non-uniform pressure distribution on the washer surface leads to an uneven lever arm with respect to the bolt axis, inducing a bending moment in the bolt.

- **$\varphi = 15°$ case:**
  The CPRESS distribution remains asymmetric along the X-axis and also shows some asymmetry along the Y-axis. This is attributed to the additional tensile component introduced by the inclined force.

- **$\varphi = 30°$ case:**
  The contact stress distribution becomes more uniform, suggesting reduced bending effects as compared to lower inclination angles.

- **Higher inclination angles ($45° \leq \varphi \leq 90°$):**
  For these cases, the CPRESS distribution becomes increasingly symmetric with respect to the Y-axis. However, a degree of asymmetry persists with respect to the X-axis, primarily caused by localized deformation near the weld toe. As the inclination angle increases, the shear force component is progressively reduced, leading to decreased contact between the bolt shank and the flange hole. This contact is most pronounced at $\varphi = 0°$ and nearly vanishes at $\varphi = 90°$.

The asymmetry in contact stress between the washer and flange confirms that the bolt is subjected to bending. This bending moment can be decomposed into two components: M_x and M_y, both of which are highly sensitive to the force inclination angle.

Additionally, it is observed that the lever arm associated with the shear load component increases as the model deforms, due to the load application point moving further away from the flange contact with the flange-bolt contact region. In deformed configuration, the axial load also contributes to a bending moment, which acts in opposition to the moment generated by the shear component. As deformation progresses, the axial force shifts slightly along the X-axis, introducing a small lever arm that results in a minor bending moment about the Y-axis (M_y). However, this contribution is very limited and has a negligible effect on the overall behaviour of the system.

5.6.3 Discussion of the results

These observations underscore the presence of significant bending moments in the bolt during the simulations – an effect not accounted for in standard analytical design methods. Current design standards typically assume that the bolt resists only axial tension, neglecting the additional stresses induced by bending, which can influence the actual load-bearing capacity of the assembly. This suggests that a more accurate assessment of the behaviour of the bolt should consider not only axial force (N) and shear force (V), but also bending moments about both the X and Y axes (M_x and M_y).

Chapter 6

Conclusions and perspectives

In traditional construction practices, structural robustness was not explicitly addressed. However, past events have underscored the vulnerability of structures to progressive collapse resulting from localized damage. Recent design guidelines now emphasize the importance of catenary effects, which activate under large deformations and necessitate significant rotational capacity at the joints. Among the joint components, T-stubs are selected for their significant ductility reserve, which is crucial for ensuring structural robustness. This thesis focuses on investigating the behaviour of T-stubs subjected to combined axial and shear loading conditions.

In the literature, the most relevant study on this topic is the work carried out at the University of Trento, particularly the research of Valerio Mancini, who experimentally investigates a T-stub specimen under various loading angles. These inclined forces result in different combinations of axial and shear forces applied to the T-stub. The experimental setup was carefully analyzed to fully understand the boundary conditions and measurement configurations until experimental collapse.

To evaluate how existing design codes well capture this complex behaviour, analytical calculations based on Eurocode and other standards (American, Australian, and Song's proposal) were performed. These standards define resistance for both the T-stubs and the individual bolts under combined actions. However, significant discrepancies were observed when comparing calculated resistances to experimental results. The limitations in accurately capturing the resistance of the T-stub under combined axial and shear loading highlight a shortcoming in the current predictive models.

To address this, a finite element model was developed using Abaqus to numerically simulate the T-stub specimen. Loads, boundary conditions and interactions were carefully implemented. However, since the constitutive laws did not include damage effects, the study was limited to the pre-damage behaviour of the T-stub.

A validation phase compared numerical outputs with Mancini's results. The model showed good qualitative outcomes but differed quantitatively in stiffness, likely due to simplifications and unavailable parameters in Mancini's study (e.g. bolt thread geometry, penetration tolerance). The bolt threads were not explicitly modelled, which limited the ability to replicate local stress concentrations at the contact interfaces with the flange and foundation hole surfaces. Nonetheless, the overall force-displacement responses were consistent enough to support further analysis.

The load application method – through three holes in the web – was analyzed through different rotational boundary conditions. It was observed that while these constraints influenced the displacement measurements on the flange, they had minimal impact on bolt behaviour. An extended model, including the three loading pins as in the experimental setup, revealed local detachment zones and stress concen-

trations, confirming that simplified models may overlook critical local effects.

A detailed stress analysis of the bolts under different load inclinations revealed non-uniform stress distributions and stress field rotations across bolt sections. The stress profiles along the bolt shank varied considerably depending on the force inclination, suggesting complex interactions between axial and shear forces. Intermediate inclination angles did not result in a simple superposition of pure axial and pure shear behaviour, but rather induced unique and nonlinear responses.

The final part of the analysis focused on identifying moment effects on the bolts. Asymmetric contact stress distributions on the washer surfaces confirmed the presence of bending moments, which varied with the loading angle. These moments include components around both the X- and Y-axes and are not considered in the analytical formulations provided by current standards.

In conclusion, this thesis demonstrates the high sensitivity of T-stub behaviour to loading configuration and boundary assumptions. It reveals the complex interplay of contact, deformation and force redistribution mechanisms in bolted joints under combined axial and shear loading. Current design standards do not sufficiently capture these phenomena.

Future research should focus on refining bolt modelling – particularly under moment-induced effects – and incorporating realistic thread geometry to improve predictive accuracy. Another valuable direction for future research is to evaluate the magnitude of the influence that bending moments have on bolt behaviour.

Appendix A

Appendices

A1 Mancini's yield graph

Mancini's graph presenting analytical versus experimental yield load component.

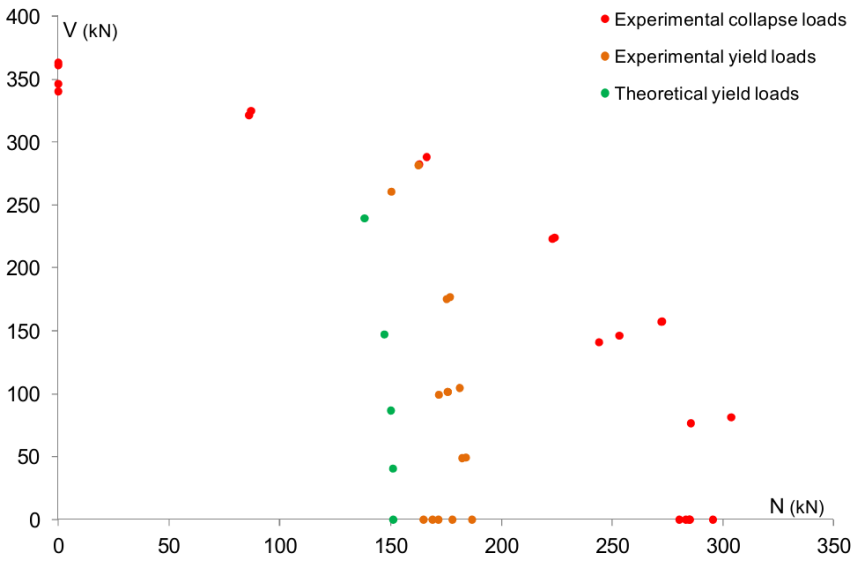

Figure A.1: Analytical vs. experimental yield load components [3]

A2 Load-displacement curves

A2.1 TR13-14 - load-displacement curves from Mancini

Load-displacement curves from Mancini corresponding to transducers 13 and 14, for inclination angles ranging from $\varphi = 0°$ to $\varphi = 75°$.

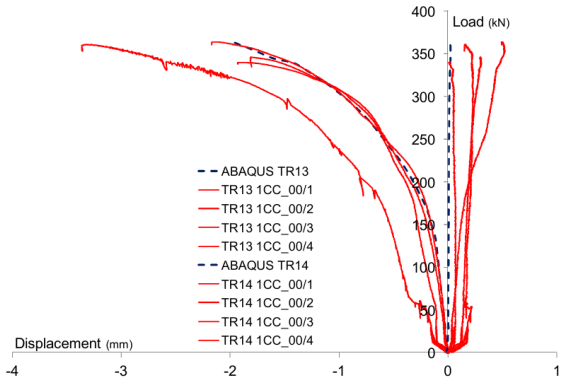

(a) $\varphi = 0°$

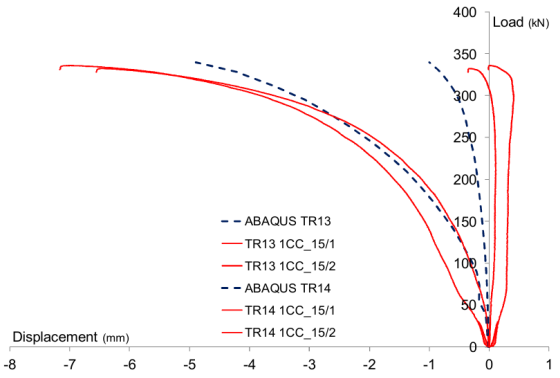

(b) $\varphi = 15°$

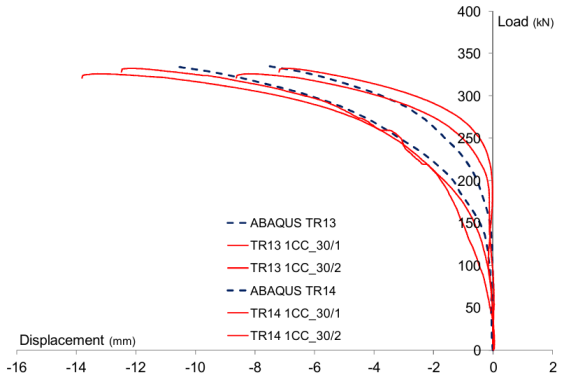

(c) $\varphi = 30°$

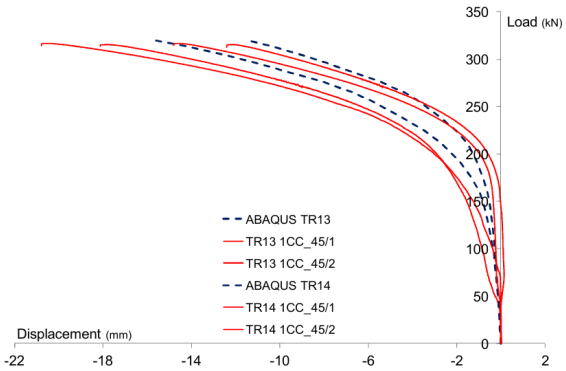

(d) $\varphi = 45°$

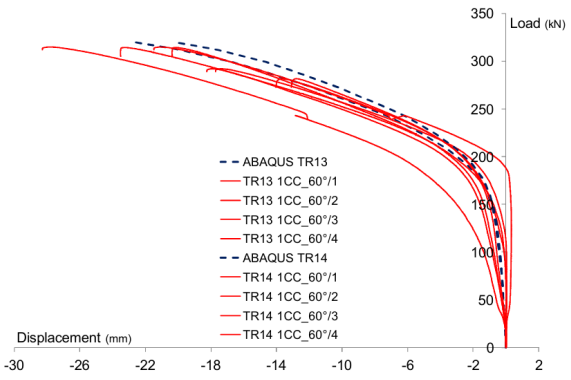

(e) $\varphi = 60°$

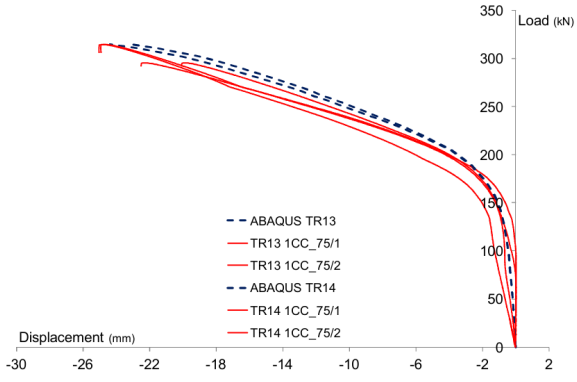

(f) $\varphi = 75°$

Figure A.2: TR13-14 - load-displacement curves from Mancini [3]

A2.2 TR13-14 - load-displacement curves

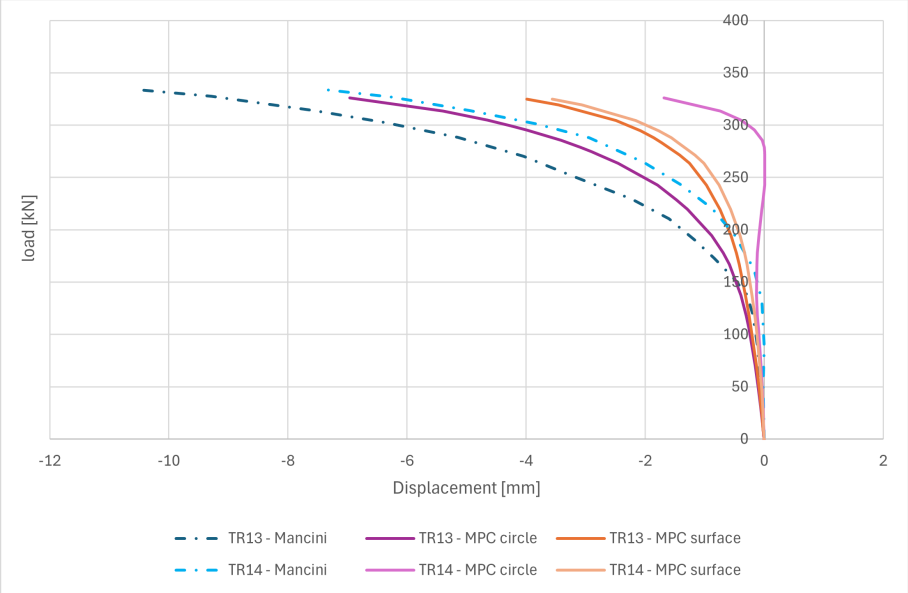

Figure A.3: Load-displacement curve for $\varphi = 30°$

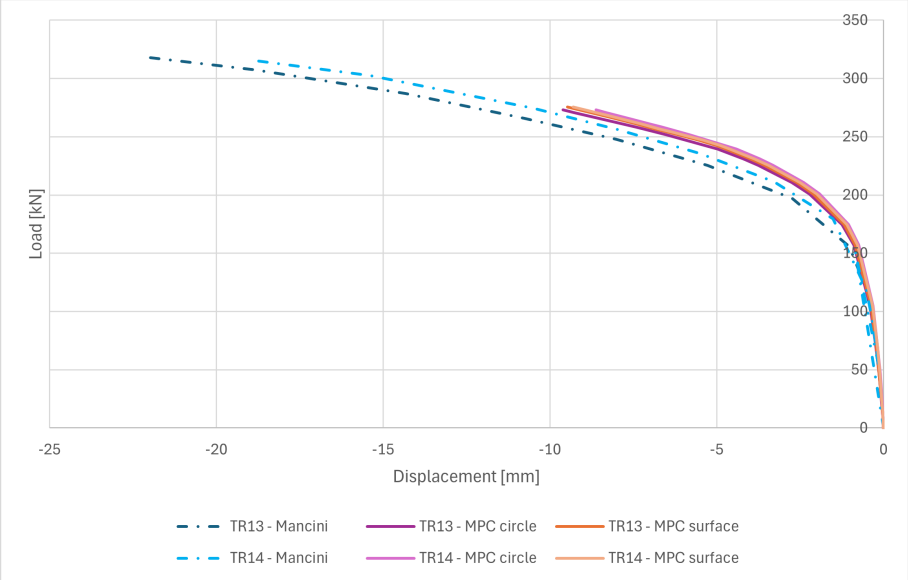

Figure A.4: Load-displacement curve for $\varphi = 60°$

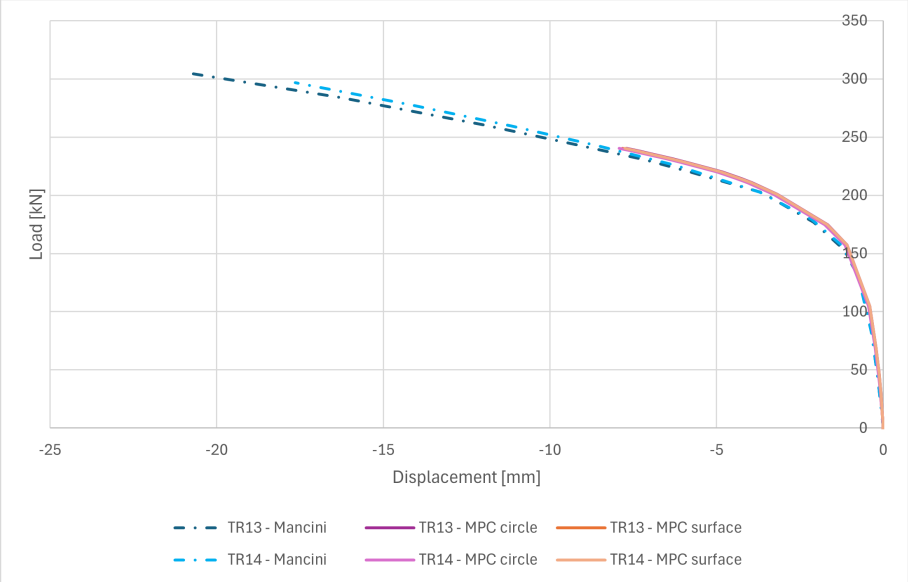

Figure A.5: Load-displacement curve for $\varphi = 75°$

A2.3 TR01-02 - load-displacement curves from Mancini

Load-displacement curves from Mancini corresponding to transducers 01 and 02, for inclination angles ranging from $\varphi = 0°$ to $\varphi = 75°$.

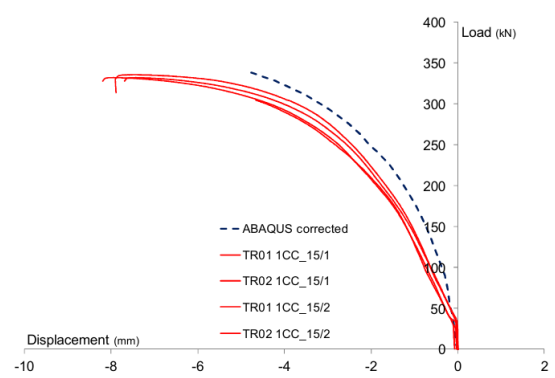

(a) $\varphi = 15°$

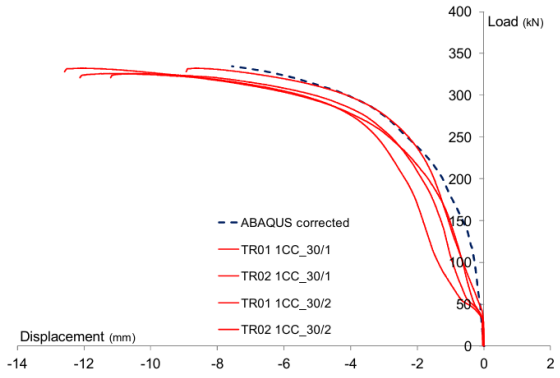

(b) $\varphi = 30°$

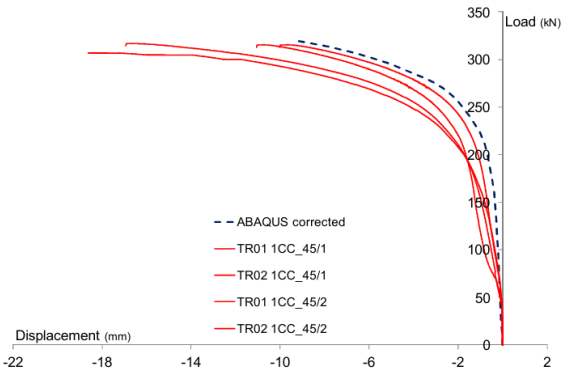

(c) $\varphi = 45°$

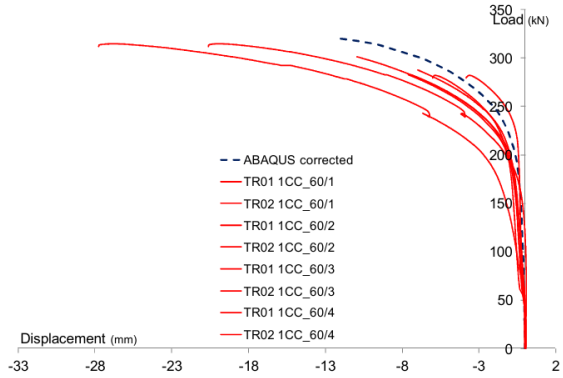

(d) $\varphi = 60°$

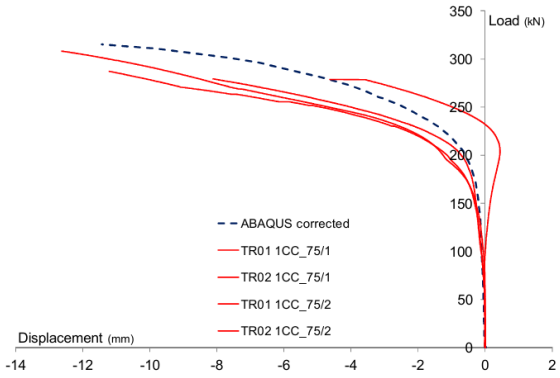

(e) $\varphi = 75°$

Figure A.6: TR01-02 - load-displacement curves from Mancini [3]

A2.4 TR01-02 - load-displacement curves

.

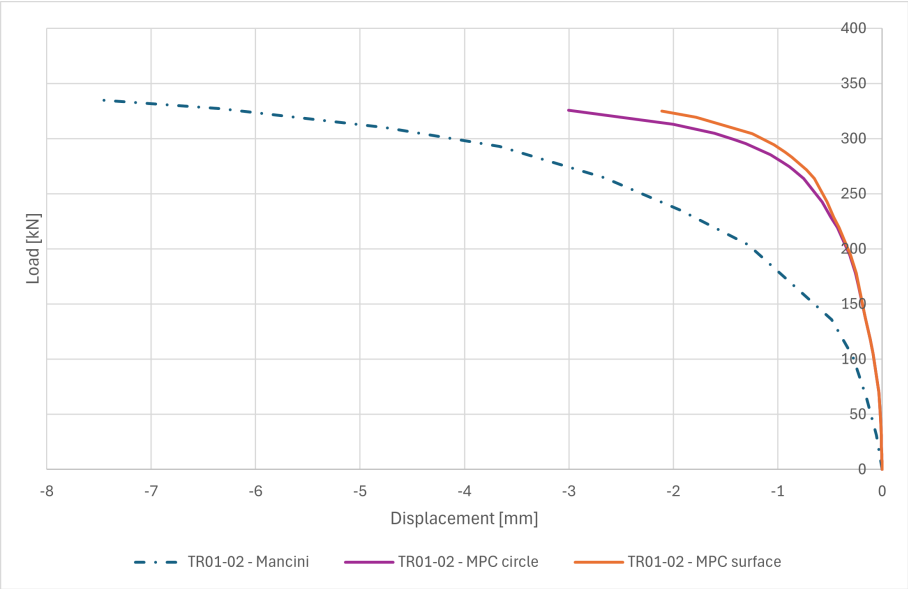

Figure A.7: TR01-02: Load-displacement curve for $\varphi = 30°$

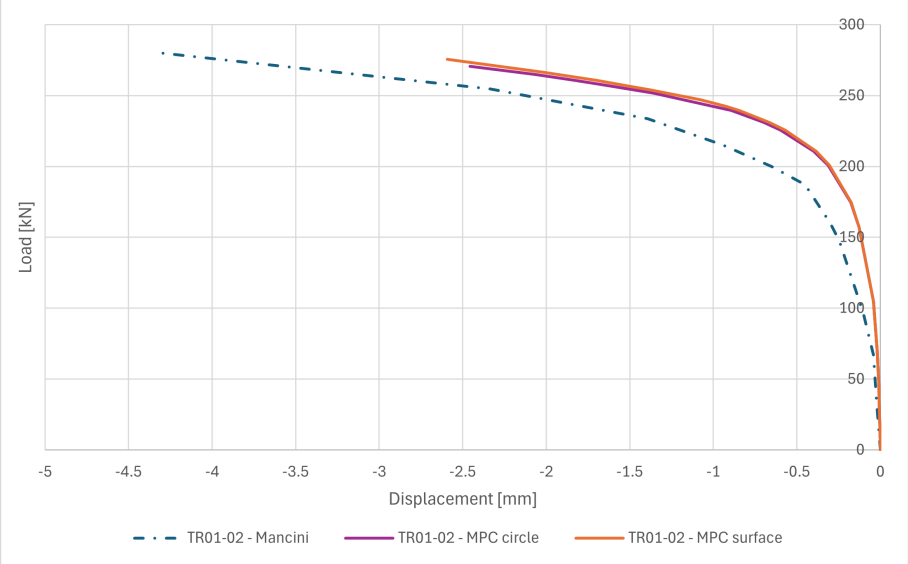

Figure A.8: TR01-02: Load-displacement curve for $\varphi = 60°$

A3 Vertical displacement of the assembly

The legend and axis orientation are illustrated in Figure A.9a and remain consistent across all Figures in this Section (Figures A.9, A.10, A.11, A.11, A.12).

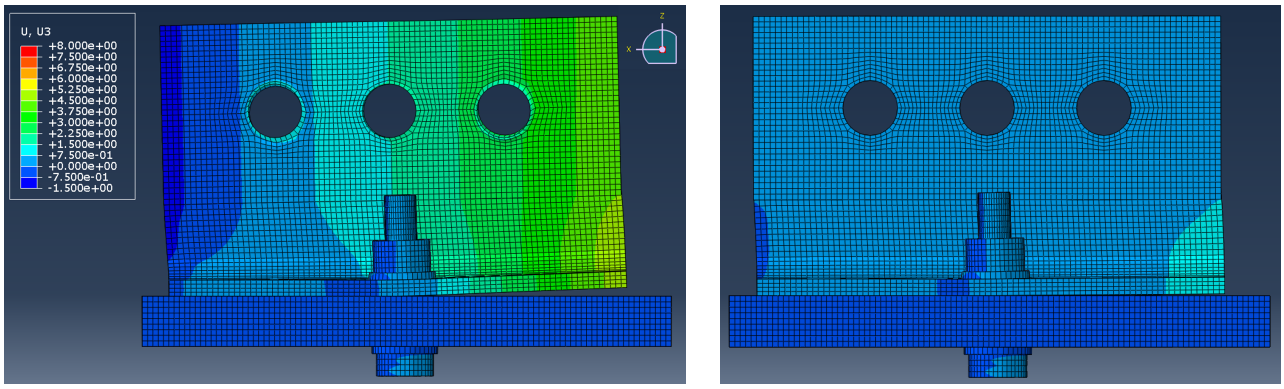

(a) *MPC circle* (b) *MPC surface*

Figure A.9: vertical (=Z) displacement of the assembly for $\varphi = 0°$

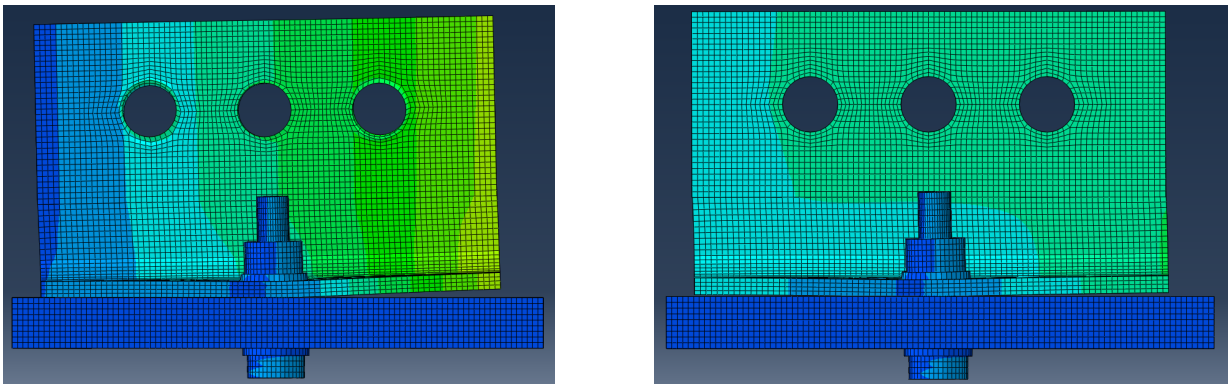

(a) *MPC circle* (b) *MPC surface*

Figure A.10: vertical (=Z) displacement of the assembly for $\varphi = 15°$

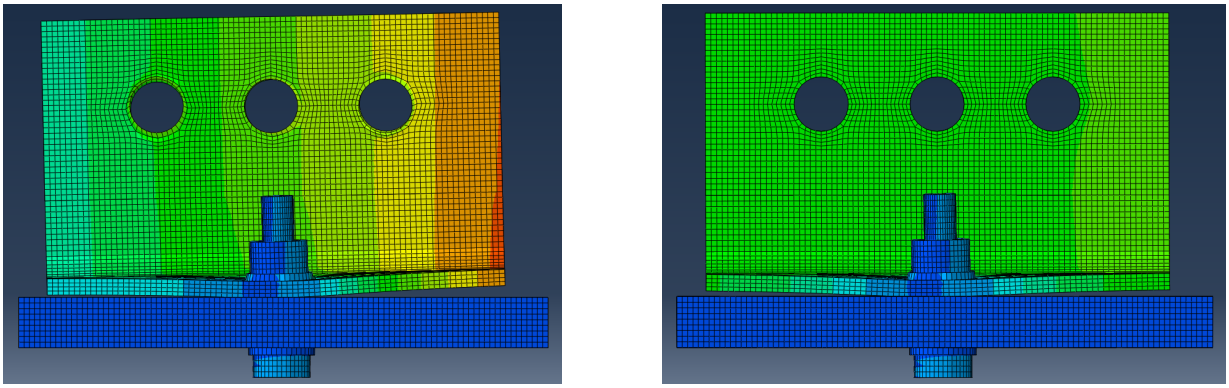

(a) *MPC circle* (b) *MPC surface*

Figure A.11: vertical (=Z) displacement of the assembly for $\varphi = 30°$

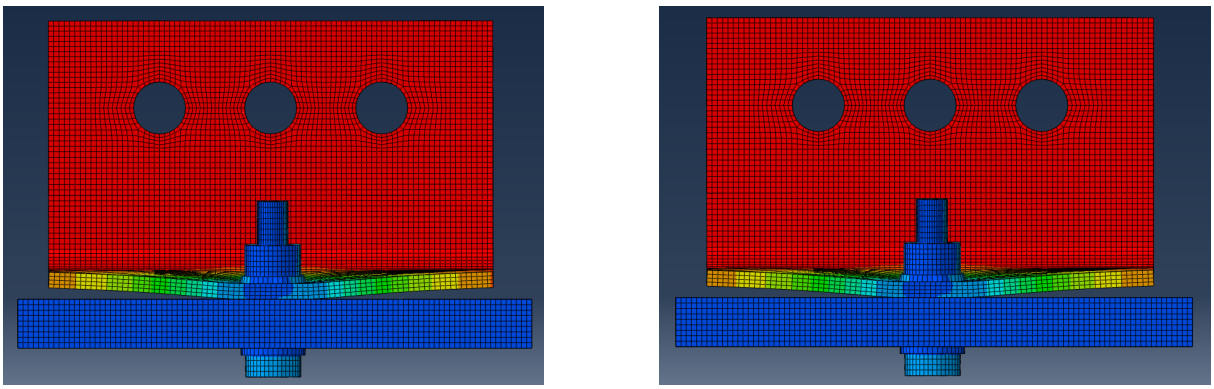

(a) *MPC circle* (b) *MPC surface*

Figure A.12: vertical (=Z) displacement of the assembly for $\varphi = 75°$

A4 3-pin model

A4.1 Modelling details of 3-pin models

All modeling steps follow the same approach as described in Section 4. The model components and their assembly remain unchanged. The material constitutive laws are preserved, and the mesh definition does not differ. The only additional meshing is applied to the pins, as illustrated in Figure A.13. The pins are discretized with a sufficiently refined mesh to ensure accurate stress and strain predictions.

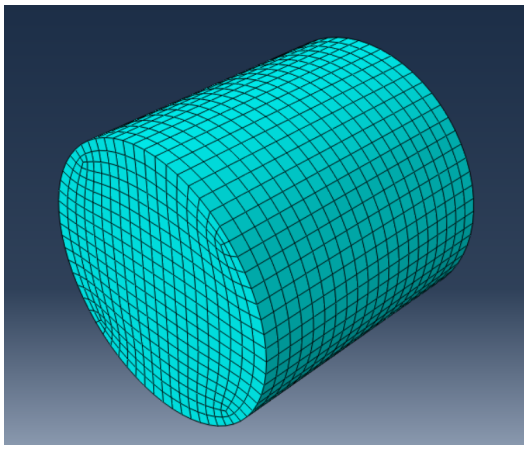

Figure A.13: Meshing of the pins

The interactions between the bolt, the plate and the foundation are unchanged. And additional interactions are created for the pins interaction with the holes of the web. These interactions are illustrated in Figures A.14a – A.14c.

The interactions between the bolt, the plate and the foundation remain unchanged. Additionally, new interactions are introduced for the contact of the pins with the holes in the web. These interactions are illustrated in Figures A.14a – A.14c.

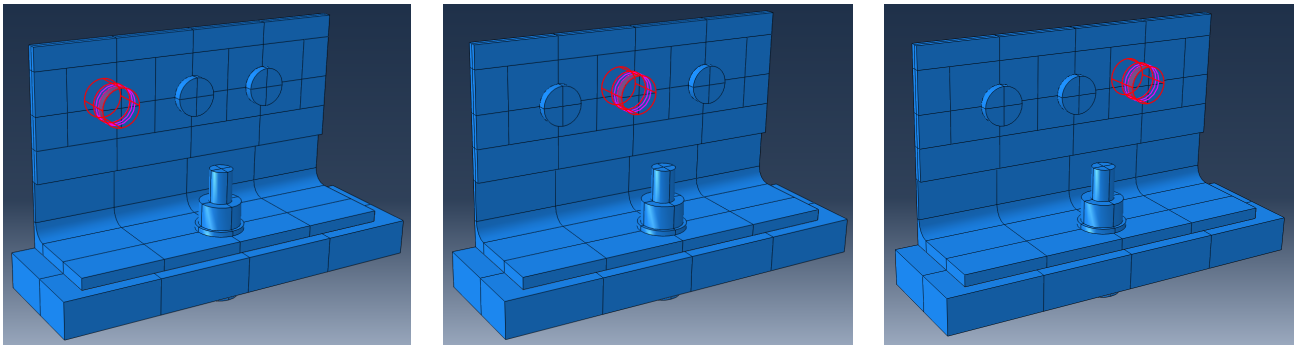

(a) left pin (b) central pin (c) right pin

Figure A.14: Interactions between the pins and the holes of the web

Boundary conditions, illustrated in Figure A.15, are applied to the flat surfaces of the pins to prevent any displacement along the Y-axis.

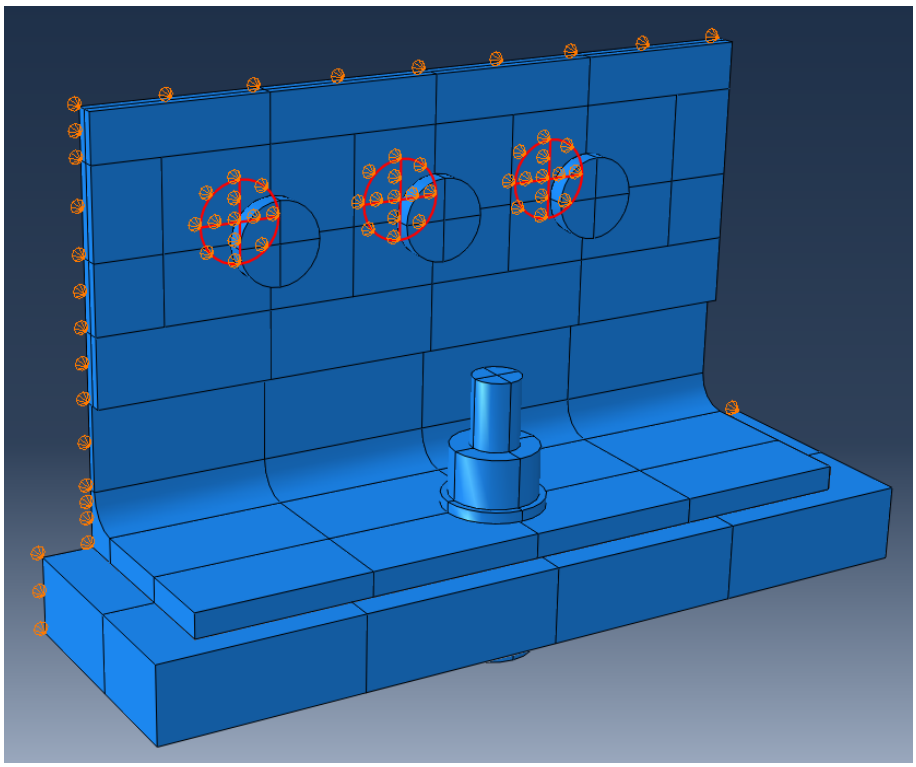

Figure A.15: Boundary condition of pins

An MPC Tie constraint is applied to the surfaces of the pins, as explained in the Section. The applied forces are localized at the center of the central pin.

A4.2 Graphs of model with 3 pins

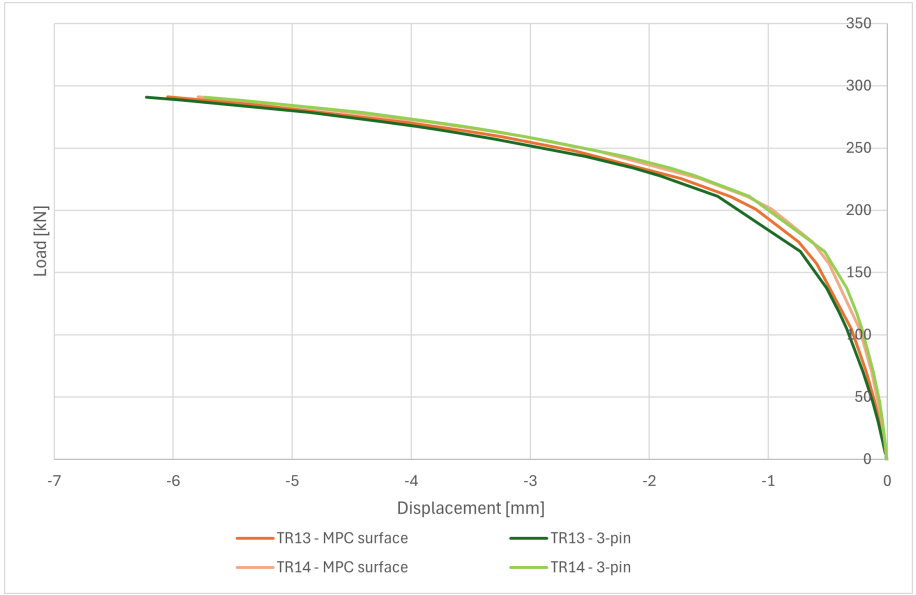

Figure A.16: Load displacement curve for inclination $\varphi = 45°$

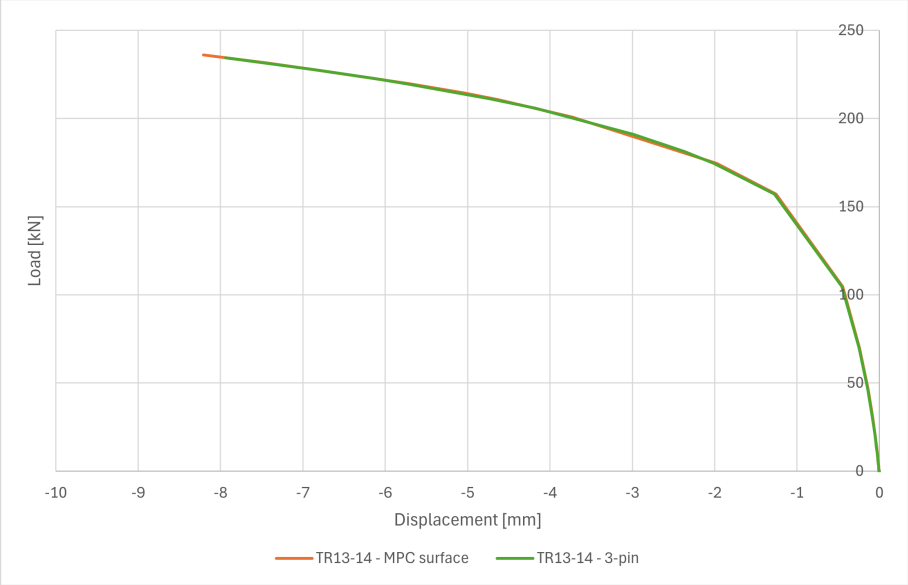

Figure A.17: Load displacement curve for inclination $\varphi = 90°$

A5 Stress distributions at cutting layers - MPC circle

The constraint applied to the holes of the T-stub may influence the stress distribution along the bolt axis. This analysis aims to further highlight the role of rotational constraints at the pin holes. If significant differences are observed in bolt stresses, it would underscore the impact of these constraints. Conversely, if the results are similar, it would suggest that the type of constraint has limited influence on the distribution of stress on the bolt.

Using the *MPC circle* constraint, the stress distribution along the bolt axis exhibits a profile very similar to that observed under the *MPC surface* constraint. Only minor differences are observed in the cutting layer 1 and cutting layer 3, and these differences involve more to stress magnitude than to distribution shape.

This consistency is illustrated in Figures 5.42 to 5.44 for the *MPC surface*, and in Figures A.18 to A.20 for the *MPC circle*. These observations confirm that the method of applying rotational constraints at the bolt holes does not significantly affect the stress distribution along the bolt shank.

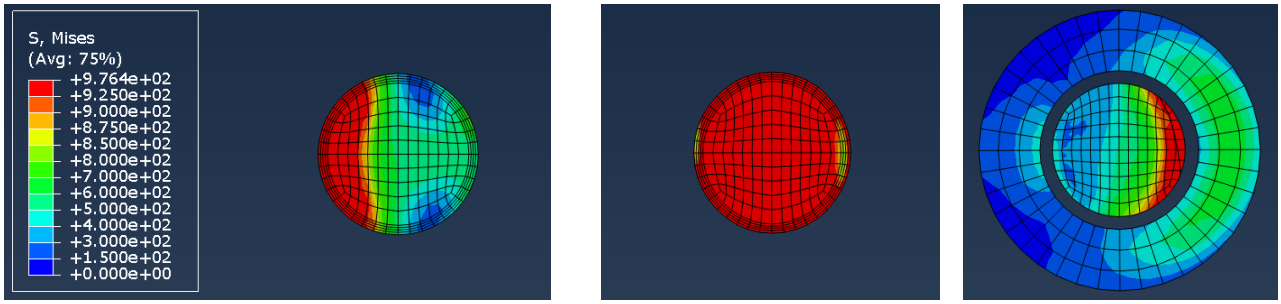

(a) Cutting layer 1 (b) Cutting layer 2 (c) Cutting layer 3

Figure A.18: $\varphi = 0°$ - ultimate load - *MPC circle*

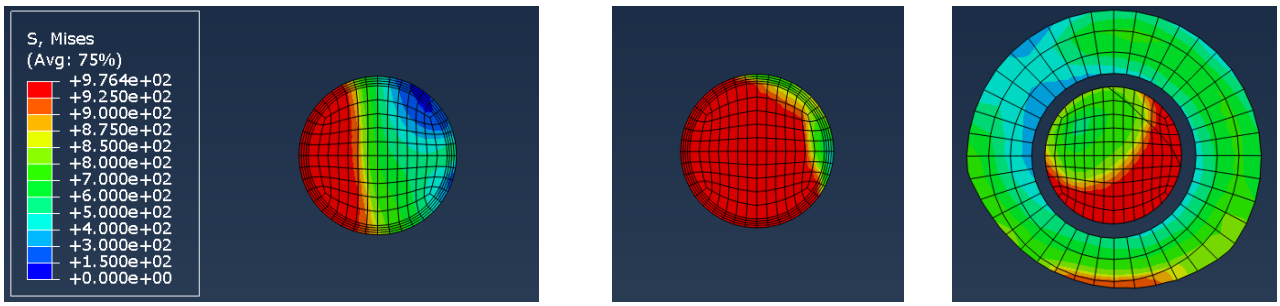

(a) Cutting layer 1 (b) Cutting layer 2 (c) Cutting layer 3

Figure A.19: $\varphi = 45°$ - ultimate load - *MPC circle*

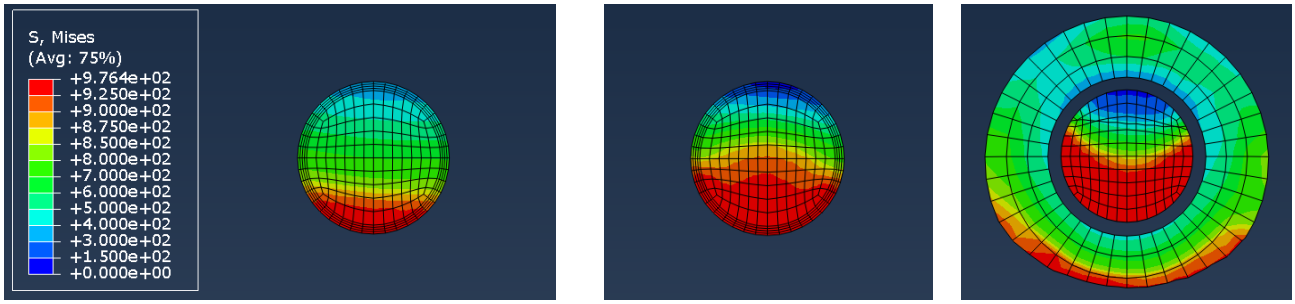

(a) Cutting layer 1 (b) Cutting layer 2 (c) Cutting layer 3

Figure A.20: $\varphi = 90°$ - ultimate load - *MPC circle*

Bibliography

[1] CEN, EN. *Eurocode 1: Actions on structures - Part 1-7: General actions - Accidental actions*. Brussels: European Committee for Standardization, 2006.

[2] Jean-Pierre Jaspart. "Contributions to recent advances in the field of steel joints, column bases and further configurations for beam-to-column joints and column bases". English. Faculté des Sciences Appliquées, Département M. S. M. MA thesis. ULiège - Université de Liège, February 1997.

[3] V. Mancini. *Response of flush endplate joints under combined actions*. University of Trento, Trento, Italy. 2012.

[4] A. Neutelers. *Improvement of the mechanical model for mode 1 T-stub plastic strength*. Université de Liège, Liège, Belgique. 2023.

[5] CEN, EN. *1-8 Eurocode 3: Design of Steel Structures-Part 1-8: Design of Joints*. Brussels: European Committee for Standardization, 2005.

[6] A. Warnant. *Contribution à l'étude des assemblages de construction métallique sous charges exceptionnelles*. Université de Liège, Liège, Belgique. 2010.

[7] B. Leruth. *Résistance ultime et capacité de déformation d'assemblages boulonnés*. Université de Liège, Liège, Belgique. 2017.

[8] Jean-Pierre Jaspart. "Etude de la semi-rigidité des noeuds poutre-colonne et son influence sur la résistance et la stabilité des ossatures en acier". French. Faculté des Sciences Appliquées, Département M. S. M. PhD thesis. ULiège - Université de Liège, January 1991.

[9] CEN, EN. *Eurocode 3 Design of steel structures Part 1-8: Joints*. Brussels: European Committee for Standardization, 2023.

[10] Jean-François Demonceau. *Cours de constructions métalliques, en béton, en bois et mixte: Concepts généraux relatifs à l'analyse et au dimensionnement des structures de bâtiments*. Support de cours, Université de Liège. 2024.

[11] P. Zoetemeijer. "A design method for the tension side of statically loaded, bolted beam-to-column connections". In: *HERON* 20.1 (1974).

[12] U. Kuhlmann, J.-P. Jaspart, R. Zandonini, et al. *Robust Structures by Joint Ductility*. Tech. rep. European research report. Luxembourg: Research Fund for Coal and Steel, 2009.

[13] ArcelorMittal. *Profilés et Aciers Marchands*. Technical catalogue. ArcelorMittal Commercial sections, 2014.

[14] Baldassino N. and al. *Experimental test on steel and concrete beam-to-column joint components*. University of Trento, Trento, Italy. 2007.

[15] FATOR. *General Catalogue*. Technical catalogue. Belgium: FATOR S.A., 2023.

[16] R. T. Douty and W. McGuire. "High Strength Bolted Moment Connections". In: *Journal of the Structural Division, ASCE* 91.2 (1965), pp. 101–128.

[17] Yuchen Song et al. "Behaviour and design of stainless steel-concrete composite beam-to-column joints". In: *Journal of Constructional Steel Research* 184 (2021), p. 106800. issn: 0143-974X.

[18] AISC. *Design Guide 27: Structural Stainless Steel, American Institute of Steel Construction*. AMERICAN INSTITUTE OF STEEL CONSTRUCTION, 2013.

[19] *AS 4100–1998 (R2016): Steel Structures*. Australian Standard. Standards Australia. Sydney, Australia, 2016.

[20] Yuchen Song et al. "Stainless steel bolts subjected to combined tension and shear: Behaviour and design". In: *Journal of Constructional Steel Research* 170 (2020), p. 106122. issn: 0143-974X.

[21] Dassault Systèmes. *ABAQUS Theory Guide Version 6.10*. `http://130.149.89.49:2080/v2016/books/usi/default.htm`. Dassault Systèmes Inc. 2010.

[22] CEN, EN. *Eurocode 3 Design of steel structures Part 1-14: Design assisted by finite element analysis*. Brussels: European Committee for Standardization, 2025.

[23] Vincenzo Piluso, Ciro Faella, and Gianvittorio Rizzano. "Ultimate Behavior of Bolted T-Stubs. I: Theoretical Model". In: *Journal of Structural Engineering* 127.6 (2001), pp. 686–693.

[24] Vincenzo Piluso, Ciro Faella, and Gianvittorio Rizzano. "Ultimate Behavior of Bolted T-Stubs. II: Model Validation". In: *Journal of Structural Engineering* 127.6 (2001), pp. 694–704.

[25] Mario D'Aniello, Raffaele Landolfo, and Federico Portioli. "Simplified criteria for finite element modelling of European preloadable bolts". In: *Steel and Composite Structures* 24.5 (2017), pp. 643–658. doi: `10.12989/scs.2017.24.5.643`.